

1 8 JUN 1998

**STRUCTURAL INTEGRITY OF INTELLIGENT  
MATERIALS AND STRUCTURES**

**FINAL TECHNICAL REPORT**

**March 1998**

**Prepared by:**

**Dr. M. Panahandeh, Principal Investigator**

**Berkeley Applied Science and Engineering, Inc. (BASE)**

**5 Third Street, Suite 530**

**San Francisco, CA 94103-3206**

**Phone: (415) 543-1600 FAX: (415) 543-1601**

**email: base@baseco.com**

**Contract No.: F49620-94-C0084**

**B A S E**

18 JUN 1998

C504

**STRUCTURAL INTEGRITY OF INTELLIGENT  
MATERIALS AND STRUCTURES**

**FINAL TECHNICAL REPORT**

**March 1998**

**Prepared by:**

**Dr. M. Panahandeh, Principal Investigator**

**Berkeley Applied Science and Engineering, Inc. (BASE)  
5 Third Street, Suite 530  
San Francisco, CA 94103-3206  
Phone: (415) 543-1600 FAX: (415) 543-1601  
email: base@baseco.com**

**Contract No.: F49620-94-C0084**

**B A S E**

# REPORT DOCUMENTATION PAGE

Form Approved

OMB No. 0704-0188

Public reporting burden for this collection of information is estimated to average 1 hour per response, including the time for reviewing instructions, searching existing data sources, gathering and maintaining the data needed, and completing and reviewing the collection of information. Send comments regarding this burden estimate or any other aspect of this collection of information, including suggestions for reducing this burden, to Washington Headquarters Services, Directorate for Information Operations and Reports, 1215 Jefferson Davis Highway, Suite 1204, Arlington, VA 22202-4302, and to the Office of Management and Budget, Paperwork Reduction Project (0704-0188), Washington, DC 20503

1. AGENCY USE ONLY (Leave blank)	2. REPORT DATE March 1998	3. REPORT TYPE AND DATES COVERED Final Technical-94Sep30 thru 97Dec30
----------------------------------	------------------------------	---

4. TITLE AND SUBTITLE Structural Integrity of Intelligent Materials & Structures	5. FUNDING NUMBERS F49620-94-C-0084
---	--

6. AUTHOR(S) M. Panahandeh A. Masud E. Kasper
--

7. PERFORMING ORGANIZATION NAME(S) AND ADDRESS(ES) Berkeley Applied Science & Engineering, Inc. 5 Third Street, Suite 530 San Francisco, CA 94103-3206 (415) 543-1600	8. PERFORMING ORGANIZATION REPORT NUMBER 93-161 Final Report
---	--

9. SPONSORING/MONITORING AGENCY NAME(S) AND ADDRESS(ES) Air Force Office of Scientific Research 110 Duncan Ave., Suite B115 Bolling AFB, DC 20332-0001	10. SPONSORING/MONITORING AGENCY REPORT NUMBER
---	--

11. SUPPLEMENTARY NOTES	19980630 040
-------------------------	--------------

12a. DISTRIBUTION AVAILABILITY STATEMENT  Approved for public release; distribution unlimited.	12b. DISTRIBUTION CODE
---	------------------------

13. ABSTRACT (Maximum 200 words)

A wide variety of applications for intelligent structure technologies exist in defense, aerospace, auto, civil and biomedical industries. Shape Memory Alloys (SMA) and laminated composite materials have unique properties suitable for these technologies. Extensive utilization of these materials requires accurate theories for the mechanics of these materials be developed. The present research is an effort in this direction. In this work;

- A thermomechanical constitutive model for phase transformation in SMA was proposed;
- Numerical schemes for solving the highly nonlinear finite element equations were developed;
- Geometrically nonlinear elements for SMA were introduced;
- The mechanics of composite laminates was formulated through a multi-director shell theory and was extended to finite kinematics in a corotational framework;
- Geometrically nonlinear plates and shell elements with multi-directors through the thickness were developed for composite laminates; and
- An extensive set of test problems was simulated to show the accuracy of the developed theories.

14. SUBJECT TERMS Nitinol, Shape Memory Alloys, Constitutive Modeling, Composite Laminates, Large Deformation Shells and Plates	15. NUMBER OF PAGES
	16. PRICE CODE

17. SECURITY CLASSIFICATION OF REPORT UNCLASSIFIED	18. SECURITY CLASSIFICATION OF THIS PAGE UNCLASSIFIED	19. SECURITY CLASSIFICATION OF ABSTRACT UNCLASSIFIED	20. LIMITATION OF ABSTRACT UL (UNLIMITED)
---	--	---	--

## **ACKNOWLEDGEMENT**

The present research was sponsored by the Air Force Office of Scientific Research (AFOSR) under contract No. F49620-94-C-0084. The financial support of AFOSR is gratefully acknowledged. The authors are indebted to Dr. C.I. Jim Chang, Director, Dr. Walter F. Jones, Program Manager, and Professor Ozden Ochoa in AFOSR for their encouragement and interest in the work.

## **DISCLAIMER**

The views and conclusions contained herein are those of the authors and should not be interpreted as necessarily representing the official policies or endorsements, either expressed or implied, of the Air Force Office of Scientific Research or the US Government.

# Table of Contents

<b>Part I</b>	<b>Introduction</b>	<b>1-1</b>
1.0	General .....	1-1
2.0	Shape Memory Alloys .....	1-3
3.0	Multilayer Shell Theory of Laminated Composites.....	1-4
4.0	Summary .....	1-7
	References.....	1-9
<b>Part II</b>	<b>Shape Memory Alloys Theory and Numerical Implementation</b>	<b>2-1</b>
1	Introduction	
1.1	Motivation .....	2-2
1.2	Background .....	2-4
1.3	Applications.....	2-6
1.3.1	Commercial Devices .....	2-6
1.3.2	Medical Devices .....	2-7
1.4	Overview .....	2-8
2	Martensite Phase Transformation	
2.1	General Characteristics.....	2-10
2.2	Classification of Transformations .....	2-11
2.3	Activation of Transformations .....	2-12
2.4	Shape Memory Effect.....	2-14
2.5	Pseudoelastic Effect.....	2-15
3	One Dimensional Shape Memory Alloy Model	
3.1	Continuum Mechanics.....	2-17
3.1.1	Kinematics.....	2-18
3.1.2	Balance Laws.....	2-22
3.2	Linearized Thermoelasticity .....	2-27
3.3	Constitutive Equation .....	2-30
3.4	Evolution Equations .....	2-32
3.4.1	Production of Austenite.....	2-32
3.4.2	Production of Positive Single Variant Martensite.....	2-35
3.4.3	Production of Negative Single Variant Martensite .....	2-38
3.4.4	Production of Multiple Variant Martensite .....	2-41
4	Finite Element Developments	
4.1	State Determination.....	2-44
4.1.1	Production of Austenite.....	2-45
4.1.2	Production of Positive Single Variant Martensite.....	2-48
4.1.3	Production of Negative Single Variant Martensite .....	2-50

4.1.4	Production of Multiple Variant Martensite .....	2-52
4.1.5	Outline of Algorithm .....	2-54
4.2	Multi-Dimensional Truss-Bar Element .....	2-56
4.2.1	Notation .....	2-57
4.2.2	Strain Measure.....	2-58
4.2.3	Variational Formulation .....	2-59
4.2.4	Finite Element Interpolations .....	2-60
4.2.5	Linear Kinematic Element.....	2-61
4.2.6	Non-Linear Kinematic Element .....	2-64
4.2.7	Solution Procedure .....	2-67
4.2.8	Numerical Simulations .....	2-68
4.3	Two-Dimensional Beam Element .....	2-84
4.3.1	Notation .....	2-84
4.3.2	Deformation Measure.....	2-85
4.3.3	Variational Formulation .....	2-87
4.3.4	Finite Element Interpolations .....	2-89
4.3.5	Linear Kinematic Element.....	2-89
4.3.6	Non-Linear Kinematic Element .....	2-91
4.3.7	Solution Procedure .....	2-93
4.3.8	Numerical Simulations .....	2-95
4.3.9	Summary of Numerical Simulations .....	2-102
4.4	Summary .....	2-102
	Bibliography .....	2-103

<b>Part III</b>	<b>A Nonlinear Composite Shell Theory</b>	<b>3-1</b>
1	Geometrically Nonlinear Finite Element Approaches .....	3-1
1.1	Introduction .....	3-1
1.2	Background on total and updated Lagrangian formulations .....	3-2
1.3	Basic philosophy of the co-rotational problems.....	3-2
1.4	Solution techniques for nonlinear finite element equations .....	3-3
2	Element Corotational Formulation for Geometrically Nonlinear Analysis of Multilayered Shells .....	3-5
2.1	Total Lagrangian Formulation.....	3-13
2.2	Updated Lagrangian Formulation.....	3-13
2.3	Element Corotational Procedure.....	3-13
3	Stabilization Techniques for Underintegrated Nonlinear Shell Elements .....	3-5
3.1	Introduction .....	3-5
3.2	Four-node quadrilateral elements.....	3-7
3.3	Eight-node hexahedral elements.....	3-13
4	Numerical Examples .....	3-22

References ..... 3-22

**Part IV Simulation of Coupled Systems** ..... 4-1

- 1 Coupled Elastic/SMA Simulations ..... 4-1
  - 1.1 Two-Dimensional Cantilever Beam ..... 4-2
  - 1.2 Two-Dimensional Simply Supported Beam..... 4-5

# Part I

## Introduction

# **PART I - INTRODUCTION**

## **1.0 General**

Intelligent material systems and structures have been investigated by various government agencies and private corporations in the past decade. Intelligent material systems and structures are engineered systems with a significant degree of autonomy that enables them to maximize performance, provide adaptive functionality, and minimize life-cycle cost. These engineered systems are formed by incorporating highly integrated actuators and sensors into the structure. These components may have structural functionality, as well as control logic, signal conditioning and power amplification electronics. Such actuating, sensing, and signal processing elements are incorporated into a structure for the purpose of influencing its mechanical and thermal characteristics to achieve desired structural performance

A wide variety of applications for intelligent structure technologies exist in aerospace, defense, auto, civil, and medical devices industries. These include aeroelastic, control and maneuver enhancement, reduction of vibrations and structure borne noise, jitter reduction in precision pointing systems, shape control of plates, trusses and lifting surfaces, isolation of offending machinery and sensitive instruments, flexible robotic arms damage detection, reduction of life-cycle-cost of buildings, bridges and lifelines, and sensitive biocompatible medical instrumentation.

The rebuilding and enhancement of our Nation's infrastructure can greatly profit from the research, development, and implementation of intelligent material systems. Intelligent material systems can allow us to design buildings, bridges, lifelines, etc. to not only have a greater envelope of utility but also do so while reducing the overall life-cycle cost—it is precisely this objective which defines intelligent systems. Intelligent structures incorporate innovative material compositions and sophistication in the design and architecture in order to simplify construction, reduce maintenance, and decrease cost of the entire system. The synergy of actuators, sensors, and controls, will not only allow structures of the future to have increased performance and functionality, but will facilitate the solution of many socio-economic issues concerning the repair, enhancement and construction of our Nation's infrastructure.

Several technical developments have been combined to establish the potential feasibility of intelligent structures. The first is a transition to laminated materials. In the past, structures were built from large pieces of monolithic materials which were machined, forged, or formed to a final structural shape, making it difficult to incorporate any active element inside the structure. However, in the past thirty years a transition to laminated material technology has occurred. Laminated materials allow for the easy incorporation of active elements within the build up of structural forms.

Exploitation of the off-diagonal terms in the material constitutive relations is a second trend makes the development of intelligent structures promising. The full constitutive relations of a material include characterizations of its mechanical, optical, electromagnetic, chemical, physical, and thermal properties. Researchers have focused on only block diagonal terms for quite sometime. For example, those interested in exploiting a material for its structural benefits have focused only on the mechanical characterization, and those interested in exploiting its electrical properties have focused on the electrical characterization. However, much gain can be obtained by exploiting the off-block diagonal terms in the constitutive relations, which for example, couple the mechanical and electrical properties or couple the mechanical and thermal properties. The characterization and exploitation of these off-diagonal material relations had led to many of the progress in the intelligent structure technology.

Central to the emergence of intelligent structures is the development of information processing, artificial intelligence, and control disciplines. These developing technologies have created the enabling infrastructure based on which intelligent structures can develop. Control architectures and algorithms are the brains of intelligent systems. These are where the very intelligence comes from. The design of these architectures and algorithms is of utmost importance for the effective utilization of smart functions of intelligent structures.

In an intelligent structure, the presence of active elements such as actuators, sensors and processors impact the host structure by increasing the mass and stiffness of the system and interfering with the load path and potentially introducing new structural discontinuities which must be accommodated. This introduces great challenges for accurate modeling of these systems. On the other hand, the complex interactions among sensors, actuators, the host materials, and the processors must be fully characterized before the technology can reach its full potential. Experimental models are powerful tools for characterizing these complicated interactions and showing the dynamic behavior of laboratory scale active systems. However, experimental models are limited by size, cost, time, noise, and many laboratory unknowns. It is virtually impossible to generate large quantities of data for full size structures. Therefore, development of a simulation package for design and analysis of smart structural systems would greatly enhance this technology.

The present research is directed toward modeling and simulation of some of the elements of smart structures such as sensors, actuators and host structures. Shape Memory Alloys (SMA) are among candidate materials suitable for wide applications as sensors and actuators in smart structures. They have the unusual material property of being able to sustain and recover large strains (of the order of 10%) without inducing irreversible plastic deformation and to "remember" a previous configuration and return to it with a

temperature change. Their ability to achieve large strains instantaneously enables the design of structures capable of extremely large, recoverable deflections. In addition, shape memory alloys are relatively lightweight, biocompatible, easy to manufacture and have a high force to weight ratio [Wayman, 1980]. These characteristics of SMA make it an ideal candidate for shape control and frequency tuning of composite laminates. On the other hand, laminated composites are best suitable as host material, for smart structural systems. Their laminated structures provide the capability of embedding sensors, actuators, and the electronic circuitry in the load-bearing structure. Following is a summary of activities related to the technology of smart structures that was pursued during the course of this research.

## **2.0 Shape Memory Alloys (SMA)**

Given the variety of potential uses for SMA and the high interest in developing new applications, the ability to accurately model and analyze structures containing SMA components via a finite element procedure is extremely attractive. The incorporation of the SMA finite element procedure into the design stages of new products could reduce development times and costs dramatically. Since the properties of a particular alloy can be easily and drastically altered in the manufacturing process, the properties of a SMA component for a given design can be varied systematically in the finite element analysis before production. This optimization procedure will enable use of shape memory alloy components with specifically tailored properties that will realize their full potential in each individual application.

The following research work related to modeling of Shape Memory Alloys (SMA) were conducted during this project.

- Development of thermomechanical constitutive relations for SMA based on the kinetics of solid-solid phase transformation for arbitrary paths in stress-temperature space.
- Development of criteria for complete cyclic loading-unloading and partial loading-unloading conditions.
- Development of numerical schemes in a finite element framework for state determination during phase transformation and solution of highly nonlinear field equations for SMA.
- Implementation of nonlinear truss and beam elements for SMA.
- Introduction of a 3D model based on the extension of the proposed 1D thermomechanical model.
- Formulation of large kinematics for pseudoelastic behavior of SMA and its finite element implementation.

- Extension of the thermomechanical model to tension-compression through introduction of new internal variables.
- Numerical and algorithmic developments with respect to the finite element method for a multi-dimensional truss and a two-dimensional beam elements.
- Extension of above formulation to finite kinematics elements.

Computational aspects of solid-solid phase transformation modeling were a challenge during the course of this research. State determination with all possibilities in a stress-temperature space required design of specific numerical schemes for convergence. The hysteresis of phase transformation in cyclic loadings, its expansion and contraction during phase transformation, and the nonlinear material response within the hysteresis loop made the modeling phase transformation in Shape Memory Alloys much more complicated as compared to the modeling of other material nonlinearities such as plasticity.

The details of these developments are discussed in Part II of the present report and in the progress reports during the course of this research.

### **3.0 Multilayer Shell Theory of Laminated Composites**

In the last two decades, composites have found increasing application in many engineering structures. Recent advances in the technologies of manufacturing and materials have enhanced the current application of composite materials from being used as secondary structural elements to becoming primary load-carrying structural components. Due to the inherent inhomogeneity and anisotropy of these materials, analysis of composite structures imposes new challenges on engineers.

Plate and shell structures made of laminated composite materials have often been modeled as an equivalent single layer using classical laminate theory (C.L.T.) [Christensen, 1979; Jones, 1975; Pagano, 1989 & 1973; Pipes & Pagano, 1970] in which thickness stress components are ignored. C.L.T. is a direct extension of classical plate theory in which the well-known Kirchhoff-Love kinematic hypothesis is assumed enforced. This theory is adequate when the thickness (to side or radius ratio) is small. However, laminated plates and shells made of advanced filamentary composite materials are susceptible to thickness effects, because their effective transverse moduli are significantly small compared to the effective elastic modulus along the fiber direction. Furthermore, the classical theory of plates, which assumes that the normals to the mid-plane before deformation remain straight and normal to the plane after deformation, under predicts deflections and over predicts natural frequencies and buckling loads. These discrepancies arise due to the neglect of transverse shear strains. The range of applicability of the C.L.T. solution has been well established for laminated flat plates

[Noor & Burton, 1989; Pagano, 1989; Reddy, 1993]. In order to overcome the deficiencies in C.L.T., refined laminate theories have been proposed [Byun & Kapania, 1992; Noor & Burton, 1990 & 1989; Reddy, 1993, Oct and Dec 1984; Robbins, Reddy & Murty, 1991; Whitney & Pagano, 1970]. These are single layer theories in which the transverse shear stresses are taken into account. They provide improved global response estimates for deflections, vibration frequencies and buckling loads of moderately thick composites when compared to the classical laminate theory. A Mindlin type first-order transverse shear deformation theory (S.D.T.) was first developed by Whitney and Pagano [1970] for multi-layered anisotropic plates, and by Dong and Tso [1972] for multi-layered anisotropic shells. Both approaches (C.L.T. and S.D.T.) consider all layers as one equivalent single anisotropic layer, thus they can not model the warping of cross-sections, that is, the in-plane distortion of the deformed normal due to transverse shear stresses. Furthermore, the assumption of a non-deformable normal results in incompatible shearing stresses between adjacent layers. The later approach also requires the introduction of an arbitrary shear correction factor, which depends on the lamination parameters for obtaining accurate results. It is well established that such a theory is adequate to predict only the gross behavior of laminates.

The exact analyses performed by Pagano [1989; 1973; Pipes & Pagano, 1970] on the composite flat plates have indicated that the in-plate distortion of the deformed normal depends not only on the laminate thickness, but also on the orientation and the degree of orthotropy of the individual layers. Therefore the hypothesis of non-deformable normals, while acceptable for isotropic plates and shells, is often quite unacceptable for multi-layered anisotropic plates and shells that have a large ratio of Young's modulus to shear modulus, even if they are relatively thin [F. Chang, Perez, & K.Y. Chang, 1990; Reddy, 1993, Oct & Dec 1984]. Thus a *transverse shear deformation theory which also accounts for the warping of the deformed normal* is required for accurate prediction of the elastic behavior (deflections, thickness distribution of the in-plane displacements, natural frequencies, etc.) of multi-layered anisotropic plates and shells.

In view of these issues we have developed a multi-director shell theory for composite laminates with the following attributes:

1. The displacement field is continuous through the thickness of the multi-layer structure while the rotation field is layer-wise continuous (in 2-D) and can be discontinuous across the finite element layers through the thickness direction. This displacement field fulfills *a priori* the geometric continuity conditions between contiguous layers.
2. The assumed displacement field is capable of modeling the distortion of the deformed normal, without increasing the order of the partial differential equations with respect to the first-order transverse shear deformation theory.
3. The assumed displacement field has a 3-D feature, thereby modeling accurately the interlaminar conditions and predicting the 3-D edge effects, in orthotropic layers.

4. Like the shear deformable theory, the proposed composite shell theory provides flexibility in the specification of the boundary conditions.
5. In this theory, at most, only first derivatives of displacement and rotation fields appear in the variational equations. The practical consequence of this fact is that only  $C^0$  continuity of finite element functions is required, which is readily satisfied by the family of LaGrange elements.
6. Development of electromechanical and thermomechanical models for simulation of active surfaces with sensors and actuators elements (either embedded or mounted) is straight forward and it is a natural extension of the theory for coupled systems.

Considerable attention has been devoted, during the past few years to the developments of active structural systems with shape control capabilities [Pfaeffle, 1993], [Beauchamp, 1992], [McLean, 1993]. These structures range from simple beams that are controlled with a single actuator to the more imaginative compliant fins that are controlled with a distributed network of actuators. In these structures, the emphasis has been placed on utilizing Nitinol fibers which are embedded either directly or indirectly inside the fabric of these multilayer structures. Generally Nitinol fibers are thermally trained to shrink and remain straight upon heating above their austenite phase transformation temperature. Restraining the fibers from shrinking, by the composite when the fibers are directly embedded or by end restraints when embedded indirectly results in the generation of large forces. By virtue of the spatial spacing between the direction of the developed phase recovery forces and the neutral planes, control moments are generated which are then used to control the shape of the structures. In this manner, the shape memory effect is not fully utilized to its complete potential particularly because the deflection of the Nitinol fibers is limited to motions along the fibers' longitudinal axes. Furthermore, the use of directly embedded fibers results in thermal buckling of the composites due to the thermal stresses induced by the activation of the Nitinol fibers. In the case of the indirectly embedded fibers, mechanical as well as thermal buckling are developed due to the generated in-plane recovery forces. In either case and before the occurrence of buckling, the stiffness as well as the natural frequencies of the Nitinol-reinforced composites is reduced considerably.

An alternative way of controlling the shape of Nitinol-reinforced composites relies on the operation of Nitinol strips which are indirectly embedded inside the composites [Baz, 1994], where a full utilization of the shape memory effect to control the shape of beams without compromising their structural stiffnesses or frequencies is demonstrated.

Several biomedical applications have also resulted in innovative designs where active structure has experienced deformations that are an order of magnitude larger than the actuator material [Barrett, 1995].

To develop modeling capabilities suitable for these applications, a comprehensive literature review was conducted on geometrically nonlinear finite element approaches and nonlinear solution techniques proposed in the last two decades. Shape control applications are mostly associated with geometrically nonlinear kinematics but small strain values. As a result, an element co-rotational procedure was selected along with a nonlinear solution technique for handling the geometric nonlinearities.

The theoretical issues related to the implementation of the co-rotational procedure and the close relationship between the Updated Lagrangian formulation and the co-rotational procedure are discussed in Part III of this report. All the approximations made in the co-rotational procedure as well as the restrictions and limitations caused by them are also identified.

## 4.0 Summary

Part II of this report presents the constitutive modeling of shape memory alloys and its numerical implementation. Martensitic phase transformations are discussed. Evolution equations for production of austenite, and single variant/multiple variant martensite are presented. State determination for finite element modeling of the theory is discussed. Truss and beam elements of SMA for both linear and nonlinear kinematics are developed and a series of numerical simulations are performed.

Part III presents the finite element formulation of geometrically nonlinear multi-layered shells in a co-rotational framework. Total and Updated Lagrangian formulations for the element co-rotation procedure are discussed. Stabilization techniques for under-integrated nonlinear shell elements are investigated, four-node quadrilateral and eight-node hexahedral elements are developed. Several simulations of flat and curved structures under various loadings are performed and the results are compared with benchmark problems to show the accuracy of the proposed theory.

Publications and presentations associated with this work are listed below.

1. "Finite Strain Formulation of Pseudoelastic Materials," *Computer Methods in Applied Mechanics and Engineering*, 148 (1997) 23-37.
2. "Multi-layered Shell Formulation of Composite Laminates," *International Journal for Numerical Methods and Engineering* (in press).
3. "Coupled Thermomechanical Simulation of Shape Memory Alloys," *Smart Structures and Materials Conference*, San Diego, March 1997.
4. "Finite Element Implementation of Large Deformation Coupled Thermomechanical Response of Shape Memory Alloys." *Fourth US National Congress on Computational Mechanics*, San Francisco, August 1997.

5. "Thermomechanical Simulation of Expansion and Contraction of Shape Memory Alloy Stent," 1<sup>st</sup> International conference on Advanced Biomaterials, October 1997, Canada.

## References

1. Barrett, R., and Gross, S., "Super active shape-memory alloys composite," SPIE Conference, San Diego, Feb. 1995.
2. Baz, A., Chen, T., and Ro, J., "Shape control of Nitinol-reinforced composite beams," SPIE 2190, 436-453, 1994.
3. Beauchamp, C.H., Nadolink, R.H., and Dean L.M., "Shape memory alloy articulated (SMAART) control surfaces," *Proc. of Active Materials and Adaptive Structures*, ed. G. Knowles, IOP Publishing Ltd., Philadelphia, PA, pp. 455-460, 1992.
4. Byun, C. and Kapania, R.K., "Prediction of interlaminar stresses in laminated plates using global orthogonal interpolation polynomials," *AIAA Journal.*, **30**, No 11, Nov. 1992.
5. Chang, Fu-Kuo, Perez, J.L., and Chang, K.Y., "Analysis of thick laminated composites," *Journals of Composite Materials*, **24**, 801-822, August 1990.
6. Christensen, R.M., *Mechanics of Composite Materials*, John Wiley & Sons, NY 1979.
7. Dong, S.B. and Tso, F.K.W., "On a laminate orthotropic shell theory including transverse shear deformation," *Journal of Applied Mechanics*, **39**, 1972.
8. Jones, R.M., *Mechanics of Composite Materials*, McGraw-Hill Book Co., New York, 1975.
9. McLean, B.J., Carpenter, B.B., Draper, J.L., and Misra, M.S., "A shape memory compliant control surface," *Proc. of SPIE Conference on Smart Structures and Intelligent Systes*, vol. 1917, pp. 809-818, 1993.
10. Noor, A.K. and Burton, W.S., "Assessment of computational models for multi-layered composite shells," *Applied Mechanics Review*, **43**, No. 4, 67-97, 1990.
11. Noor, A.K. and Burton, W.S., "Assessment of shear deformation theories for multi-layered composite plates," *Applied Mechanics Review*, **42**, No.1, 1-13, 1989.
12. Pagano, N.J., *Interlaminar response of composite materials*, Composite Materials Series, Vol. 5., Elsevier, New York, NY, 1989.
13. Pagano, N.J. and Pipes, R. B., "Some observations on the interlaminar strength of composite laminates," *Int. J. Mech. Sci.*, **15**, 679, 1973.
14. Pfaeffle, H.J., Lagoudas, D.C., Tadjbakhsh, I.G., and Craig, K.C., "Design of flexible rods with embedded SMA actuators," *Proc of SPIE Conference on Smart Structures and Intelligent Systems*, vol. 1917, pp.762-773, 1993.
15. Pipes, R.B. and Pagano, N.J., "Interlaminar stresses in composite laminates under uniform axial extension," *J. Comp. Materials*, **4**, 538-548, 1970.

16. Reddy, J.N., "An evaluation of equivalent-single-layer and layer-wise theories of composite laminates," *Composite Structures*, **25**, 21-35, 1993.
17. Reddy, J. N., "A simple higher-order theory for laminated composite plates," *Journal of Applied Mechanics*, **51**, 745-752, December 1984.
18. Reddy, J. N., "A refined non-linear theory of plates with transverse shear deformation," *Int. J. Solids Struct.*, **20**, 881-896, October 1984.
19. Robbins, D.H., Reddy, J.N. and Murty, A.V.K., "On the modeling of delamination in thick composites," in *Enhanced Analysis Techniques for Composite Materials*, ed. L. Schwer, J. N. Reddy and A. Mal, *The Winter Annual Meeting of the American Society of Mechanical Engineers*, Atlanta, Georgia, December 1-6, 1991.
20. Wayman, C.M., "Some applications of shape-memory alloys," *J. Metals*, **32**, 129-137, 1980.
21. Whitney, J. M. and Pagano, N.J., "Shear deformation in heterogeneous anisotropic plates," *J. App. Mech.*, **37**, 1031, 1970.

## Part II

# Shape Memory Alloys Theory and Numerical Implementation

# Chapter 1

## Introduction

Part II of the report covers our research in the area of constitutive modeling of shape memory alloys, applications, general characteristics of martensitic transformations and a new constitutive model for solid-solid phase transformations. A new algorithm is developed for the thermo-mechanical constitutive model based on trial values of stress and strain. Lastly, the model is implemented into a multi-dimensional truss and a two-dimensional beam element. For each of these cases we consider both linear and finite kinematics.

The objective of this part of the report is the formulation and implementation of a robust and efficient class of finite elements for the treatment of first order solid state martensitic transformations. A constitutive model describing the macroscopic behavior of martensitic transformations is developed in the setting of linear and finite kinematics. Due to its broad use in industry, Nickel-Titanium (NiTi) is considered for the majority of the numerical simulations. However, it should be noted that these developments are applicable to other binary and ternary alloys.

The remainder of this chapter describes the motivation of the present work as well as a brief literature review of martensitic transformations from a material and numerical standpoint. Lastly, an overview of the subsequent chapters is outlined.

## 1.1 Motivation

For the past several decades, researchers have been working in the area of solid-solid phase transformations, specifically martensitic transformations. Some alloys which undergo martensitic phase transformations have the ability to deform up to a strain of approximately 11% for single crystals and approximately 8% for polycrystals FUNAKUBO [1984] AND DUERIG ET.AL. [1990], which is an order of magnitude greater than common engineering alloys used for design structures such as carbon and stainless steels. These alloys are commonly referred to as Shape Memory Alloys (SMA). The range of strain for SMA, although moderate, can be “fully” recovered under either a load and/or a thermal cycle. The conditions for this recovery depend upon a variety of parameters, to be discuss in detail in Chapter 2.

During the transformation process, the crystal structure of the material is altered, resulting in microscopically and macroscopically measurable changes in the mechanical, thermal, acoustical, electrical and magnetic properties DUERIG ET.AL. [1990]. These characteristics, which can be designed into the material by adding alloying elements, make SMA attractive from an engineering standpoint. In addition to the physical changes, the alloys have other features which make them attractive, such as biocompatibility, high resistance to corrosion and fatigue, and a high force to weight ratio.

There are a variety of SMA currently available, but few exhibit the range of motion described above, especially under cyclic conditions. The most common alloys used are a binary alloy Nickel-Titanium (NiTi) and ternary copper alloys CuZnAl and CuAlNi. The alloy which is of most interest for the current study is NiTi commonly referred to as Nitinol (Nickel Titanium Naval Ordnance Laboratory), due to its high recoverable strain, manufacturability and its potential in the medical industry.

As an example of a simple engineering application for SMA, we consider the area of smart structures, namely active vibration control and shape control. Through a variation in the kinetic or thermal fields, the strain level and material properties can be altered to facilitate a desired response of the structure. Figure 1.1 depicts the use of these alloys or “smart materials” in a simple mass-spring system for vibration control.

Figure 1.1 depicts a spring-mass system in two different temperature states. The system on the left is at a low temperature,  $T = T_0$  where the crystal structure of the spring is such that the stiffness is given as  $K = K_0$ . The system on the right is at a high temperature,  $T = T_0 + \Delta T$ , under the same state of stress. At the elevated temperature the crystal structure of the spring is alter such that the resulting stiffness is  $K = \alpha K_0$ . The fundamental

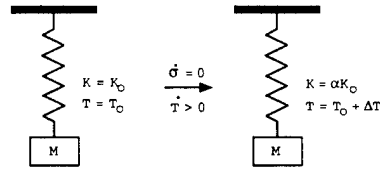


Figure 1.1: Vibration control for a spring-mass system using smart materials for a constant load and variable temperature.

frequency of this simple spring-mass system is given by  $\omega = \sqrt{K/M}$ . We see that ratio in the fundamental frequency between the two states is  $\sqrt{\alpha}$ . As an example, relative changes in the frequency as high as a factor of 2 (i.e.  $\alpha \approx 4$ ) can occur for temperature variations of  $\Delta T = 15 - 40C$  for NiTi, FUNAKUBO [1984].

As previously mentioned, the potential for SMA in the medical industry is increasing. Since biocompatibility is paramount for medical devices, the composition of the alloys must be chosen judiciously. Fortunately, one of the best biocompatible alloys in the class we are concerned with is NiTi. The main concern with regard to biocompatibility or toxicity is the surface of the instrument or device and since NiTi naturally forms an oxidized layer of  $TiO_2$  on its exterior, it is a good candidate for medical applications. One such application is a medical device referred to as a stent, see Figure 1.2. The stent is placed within an artery typically after full balloon angioplasty to aid and give support to deteriorated regions. Traditionally, in this procedure a stainless steel stent structure is placed over the balloon and expanded with the balloon against the artery wall, once the balloon is deflated and removed the stent remains expanded. Although similar in design and construction to their stainless steel counterparts, the NiTi stents give the advantages of: deliverability to the region of choice after the angioplasty has been performed, a reduction in the pressure the stent exerts on the vessel wall (typically the stent is design such that the resulting stiffness of the in-situ stent is low), it detectability under exploratory procedures such as MRI, increased biocompatibility, the ability to recover its geometry in the event of a local bifurcation of the artery due to some external stimuli and its amenability to surface coatings for local drug delivery.

Further applications are discussed in WAYMAN [1980] AND FUNAKUBO [1984], which include package clamps, disc seals, shut off valves, orthodontic arch wires, medical guidewires and catheters, eyeglass frames, orthopedic implants and more.

The key focus of the present work is to develop a robust constitutive model, which is readily

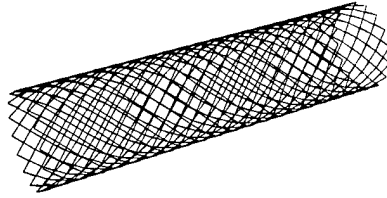


Figure 1.2: NiTi medical stent.

implemented into a numerical setting for the analysis and design of shape memory alloy structures. The particular avenue used to numerically solve the representative equations of the model problem will be the finite element method.

## 1.2 Background

The first recorded observation of a shape memory alloy was in 1932 by CHANG & READ [1951] for AuCd. Subsequent discoveries of various copper and iron based alloys were discovered shortly afterward. However in 1961 the Naval Ordnance Laboratory observed that NiTi had properties of a SMA, BUEHLER ET. AL. [1963]. Since that time significant work has been directed to the understanding of both the microscopic and macroscopic behavior of these alloys.

There are a variety of approaches researchers have taken to model and understand the behavior of shape memory alloys. We overview some of the more outstanding areas and highlight their strategies.

One approach is concerned with describing the process of the phase transformation on a local level. This approach has been to develop models based upon non-convex multi-well free energy formulations with an addition of a non-local interaction terms to account for interfacial energy at the phase boundary. Using a Landau-Devonshire based model FALK [1980] was the first to apply a multi-well free energy function to describe both stress and thermally induced phase transformations for martensitic transformations. Additional work soon followed along these lines and are discussed in FALK [1984], BALL & JAMES [1992], SUN & HWANG [1993AB], ABEYARATNE & KNOWLES [1993], KAFKA [1994AB], ABEYARATNE ET.AL. [1994], KIM & ABEYARATNE [1995], ROGERS [1996], AND PATOOR ET. AL. [1996]. MULLER & XU [1991] extended the developments above to model the characteristics of the phase transformations

at high temperatures, specifically pseudoelasticity.

Utilizing arguments from thermodynamics and statistical mechanics MULLER & WILMANSKI [1981], ACHENBACH & MULLER [1985] ACHENBACH [1986] AND ACHENBACH [1989] have developed a rate-dependent constitutive model to describe the martensitic phase transformation under kinetic and thermal loading.

The significant work done in the area of micro-mechanics and statistical thermodynamics with respect to martensitic transformations has enabled the development of macro-structural models. Specifically, a phenomenological approach in which the micro-structure is accounted for by the introduction of internal variables into the constitutive theory. TANAKA & IWASAKI [1985] AND TANAKA [1986] incorporated the earlier work on free energy functions to develop a rate-independent model which describes the phenomenological behavior of martensitic phase transformations for a one-dimensional bar under a tensile stress state. LIANG & ROGERS [1990] extending this work by integrating Tanaka's rate equations to develop a model in which evolution equations have an explicit form. BRINSON & LAMMERING [1993] incorporated the Tanaka model into a finite element setting with finite kinematics for a one-dimensional bar, again restricted to a tensile state of stress. IVSHIN & PENCE [1994AB] extended the constitutive theory to incorporate thermal effects under a tensile state of stress, but due to the complexity and parameters needed for their model (i.e. specific entropies), their model has not attracted attention from an implementation standpoint. A general phenomenological model for SMA was also developed by AURICCHIO [1995] for both tensile and compressive states for pseudoelasticity.

As seen above, efforts have just recently begun in the area of computational mechanics in regard to general phenomenological shape memory alloys models. The numerical models which have been developed thus far are limited to a high temperature regimes and account for micro-structure production/depletion in tensile states of stress only. To overcome these deficiencies we have developed a one-dimensional constitutive model and algorithm which encompasses the fully thermomechanical regime of the phase transformation space for both tensile and compressive states of stress. The constitutive model is based upon the introduction of internal variables for both tensile and compressive states from which we develop evolution equations which capture the phenomenological behavior of the martensite phase transformations for all temperature and stress states. In addition, an algorithm for state determination is developed which relies on modified trial state variables.

## 1.3 Applications

Shape memory alloy devices have been used commercially for over twenty years, WAYMAN [1980]. With the advent of shape memory alloys in the market place, products have exhibited enhanced functionality with respect to their ability to react and adjust to an external process in real time. These products have a wide range of applications. The two main areas of focus are: commercial and medical applications.

There are two main mechanisms employed for the design and construction of SMA devices, free and constrained recovery. In some designs a combination of both is used. *Free recovery* typically consists of an initial configuration in which the specimen is crystallographically martensite and under the action of external stimuli is deformed into an intermediate configuration. The specimen is then heated and freely recovers the imposed deformation, at the new configuration the specimen is in an austenitic state. This process may be repeated by cooling the specimen from the austenitic state, at zero load, to form martensite, which is then loaded and subsequently heated. This mode of recovery is widely used in medical instruments for the recovery of blood clots or other inclusions within the body. *Constrained recovery* consists again of an initial configuration in which the specimen is crystallographically martensite and under the action of external stimuli is deformed into an intermediate configuration. The specimen is then placed in contact with another component in the system. Upon heating, the specimen attempts to recover the deformation initially imposed on it, but the contact points restrict a full recovery. The resulting contact points firmly join the two parts together. This approach is widely used for couplers and clamping devices.

### 1.3.1 Commercial Devices

Commercial applications include some of the following products: brassiere underwires, antenna rods for cellular telephones, orthodontic bridge wires, temple and bridge components for eye glass frames, pipe couplings, coffee maker components, thermostatic mixing valves, active vibration and shape control of composite structures embedded with shape memory alloy fibers and deployment and release mechanisms in extreme conditions, such as space and deep sea exploration.

The first significant application in the commercial sector were pipe couplers, WAYMAN [1980] employing constrained recovery to join two pipes or repair cracks in existing pipelines, see Figure 1.3 The process for the coupling begins initially at ambient temperature in an

austenitic state. The coupling is cooled below a critical value and loaded and/or deformed mechanically until the coupling has transformed into 100% martensite crystallographically. The expanded coupling is placed over the location to be joined and allowed to heat up to ambient temperature. During the thermal cycle a reverse phase transformation to austenite occurs, along with the associated strain recovery. The resulting parts are securely fasten by the SMA coupling. Years of service have shown remarkable reliability of these shape memory alloy connectors under various conditions leading to the extended use of SMA constrained recovery for other sealing and fastening devices.

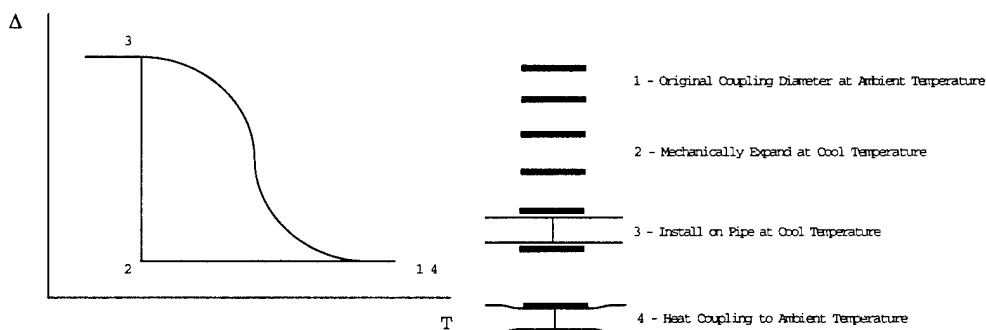


Figure 1.3: Shape memory alloy pipe coupling. The process begins with the specimen at ambient temperature (1) and is then cooled at a constant load (typically zero) transforming the austenite to multiple variant martensite (2). The coupling is then expanded, transforming the specimen to a single variant of martensite and placed over the pipe to be joined (3). Lastly, the coupling is allow to heat to ambient temperature and contracts (4).

### 1.3.2 Medical Devices

The medical applications are numerous and has potential for significant growth in applications. The predominant shape memory alloy structures used in the medical field are guidewires, hingeless and steerable instruments and self expanding stents.

Guidewires are used to access the desired location in the body from an external entry point. Once the guidewire is in place, the device, such as a catheter, is delivered over the guidewire to area of interest. With its inception in 1953 (FERNALD ET. AL. [1994]), stainless steel guidewire have aided the surgeon in many tasks. The recent introduction of Nitinol guidewires in 1987 (FERNALD ET AL [1994]) has gained wide acceptance due to its superior performance

over its stainless steel counterpart. The difference of shape memory alloy guidewire over typically used stainless steel is the superior performance in trackability, kink resistance, flexibility and torquability. These features yield a guidewire which can maneuver through various pathways in arteries without undergoing permanent deformation or buckling, while maintaining excellent controllability.

Self-expanding stents, see Figure 1.2, are utilized for the treatment of stenosis of hollow organs or arteries by aiding in the support of the deteriorated region, see OZAKI [1996] AND SIGWART [1997] for a general review of stents and new technologies. The placement of the stent is described below. The stent with an initial diameter of  $3 - 15\text{mm}$  is cooled below a critical temperature and placed into a delivery tube with an outside diameter of  $1 - 6\text{mm}$ . The delivery tube with the stent inside is then heated to room temperature. The delivery tube is placed on a guidewire and brought to its desired location. Once the delivery tube is at the desired location, the stent is pushed out of the delivery system. The stent undergoes a reverse transformation (martensite to austenite) and expands to its original shape and size. The stents are designed such that the final configuration minimizes the contact pressure with the vessel wall. The placement of the stents keeps the vessel open and allows unimpeded blood flow. The advantage over the stainless steel stent model is its ability to expand and/or contract twice or more its size without the onset of permanent deformation. The ability of contracting the stent without permanent damage reduces the size of the delivery tube in which the stent is placed, which in turn avoids large incisions or surgery for the placement of the delivery tube and reduced trauma to tissue. These benefits result in accelerated recovery for the patient and reduced hospital costs.

## 1.4 Overview

Part II of this report is directed toward constitutive theory and numerical implementation using the finite element method of shape memory alloys. An outline of each section is briefly discussed below.

In Chapter 2 we discuss the general characteristics of martensitic phase transformations and the associated macroscopic behavior. Chapter 3 summarizes the general theory of a thermomechanical continuum with the inclusion of internal variables. Constitutive models for shape memory alloys for linear and finite kinematics are also developed and discussed in Chapter 3. Numerical and algorithmic developments with respect to the finite element method are proposed in Chapter 4 for a multi-dimensional truss-bar and a two-dimensional

beam element. Several simulations are presented which show the qualitative and quantitative behavior of the model under various loading conditions. The development of the algorithm for the determination of state is also presented, along with its advantages over commonly used methods.

## Chapter 2

# Martensitic Phase Transformations

This chapter is dedicated to describing the general characteristics of martensitic phase transformations. Both mechanical and thermodynamic aspects of phase transformation classification and activation will be addressed. We also discuss the characteristic features of the shape memory effect and the pseudoelastic effect for shape memory alloys.

### 2.1 General Characteristics

Martensitic transformations, classified as first order diffusionless displacive transformations, consist of lattice transformations involving shearing deformation, which results from a cooperative motion of atoms over a small distance. This movement is such that there exists a one-to-one correspondence between lattice points in the parent phase (austenite) to the lattice points in the product phase (martensite), known as lattice correspondence. The interface between the parent and the product phases corresponds to the plane on which shearing occurs during the transformation. This plane is commonly referred to as the habit plane and during transformation is accompanied by a macroscopic change in shape. Throughout the transformation, the habit plane experiences no strain or rotation. These conditions lead to preservation of planes and lines between the parent and product phases and is thus termed an invariant plane which can be described by a linear transformation as shown in Figure 2.1.

During a martensite transformation, the motion shown in Figure 2.1 represents an idealization. Typically, a number of martensite crystals are formed with differing habit plane

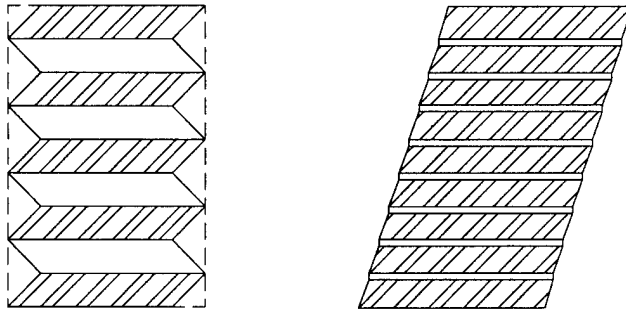


Figure 2.1: Martensitic transformation from a multiple variant state to single variant state. The solid and hatched regions represent different variants of martensite, which coalesce into a single variant under external stimuli. The plane or interface between the variants is called the habit plane.

indices, but all crystallographically equivalent. The differing habit planes' indices are called variants.

Also note from Figure 2.1 the martensitic transformation is predominantly a shearing type of motion, resulting in a quasi-isochoric motion. The relatively small change in volume ( $-0.1\%$  to  $0.1\%$ ) FISHER [1994] and lattice structure allows the transformation to proceed without incurring plastic deformation in the parent phase. Whereas, for ferrous alloys the volume change is typically an order of magnitude larger (although regarded as being isochoric) and plastic deformation is evident in the parent phase.

Lastly, the crystal structure of martensite is relatively less symmetric compared to the parent phase from which various variants of martensite occur. Due to the reduced symmetry, the variety of lattice correspondences between phases involved in the reverse transformation are restricted. A result of its ordered structure, the orientation of the parent phase is automatically preserved.

## 2.2 Classification of Transformations

There are two types of martensitic transformations: athermal and isothermal. For the development of the shape memory alloy model we only need to consider athermal transformations,

outlined below.

An athermal transformation is a transformation which advances when the thermal field is below some critical temperature  $T_{ms}$ <sup>1</sup> in a stress free reference configuration. Above this temperature, the parent phase is stable (i.e. the material has a natural affinity to an austenitic state). The transformation may be non-thermoelastic or thermoelastic. If non-thermoelastic during the transformation, martensite micro-regions are nucleated and grow to their final size over a very small time interval (approximately 1/3 the elastic wave speed of the solid, FISCHER [1994]). Continued cooling will not affect further growth of the martensite crystals. The transformation will continue by further nucleation and growth of martensite until in the remaining parent phase is depleted. Conversely, in thermoelastic transformations after the martensite micro-regions are nucleated they continue to grow at a rate proportional to the thermal field. Shape memory alloys are an example of thermoelastic transformations.

Moreover, most thermoelastic transformations occur in ordered alloys since they are crystallographically reversible. Since the original orientation of the parent phase is necessarily selected during the transformation, alloys which undergo thermoelastic transformations also experience the shape memory effect, which will be discussed in the following sections.

## 2.3 Activation of Transformations

Activation of a martensitic transformation occurs due to the presence of a driving forces, either thermal or kinetic. To initiate a transformation, the chemical free energy difference between the parent and product phases must be greater than the necessary free energy barriers, such as transformational strain energy or interface energy, as shown in Figure 2.2.

The temperature  $T_{ms}$ , indicates the critical value the temperature must be reduced to, from the equilibrium temperature  $T_0$ , in order for the forward transformation to occur. This reduction in temperature and subsequent value for the free energy is the necessary driving force for the martensite transformation. The temperature denoted by  $T_{as}$  indicates the critical temperature at which the reverse transformation will occur, if the temperature is increased. The forward and reverse transformation can be seen as a product wedge within the parent phase, as depicted in Figure 2.3, under the action of an external driving force either thermal or kinetic.

---

<sup>1</sup>The symbol  $T_{ms}$  denotes the critical temperature below which martensite is produced.

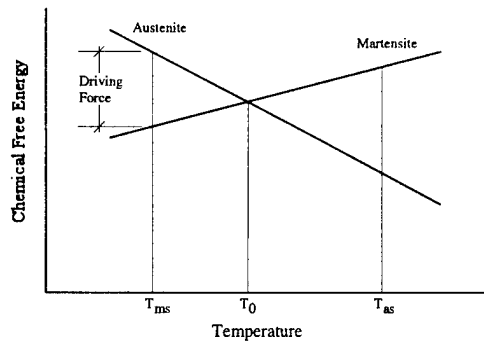


Figure 2.2: Free energy versus temperature. At  $T_0$  we see that both austenite and martensite can co-exist. Whereas, at lower temperatures austenite is unstable and the system has a natural affinity towards martensite. The opposite is true for high temperatures where austenite is stable and martensite is not.

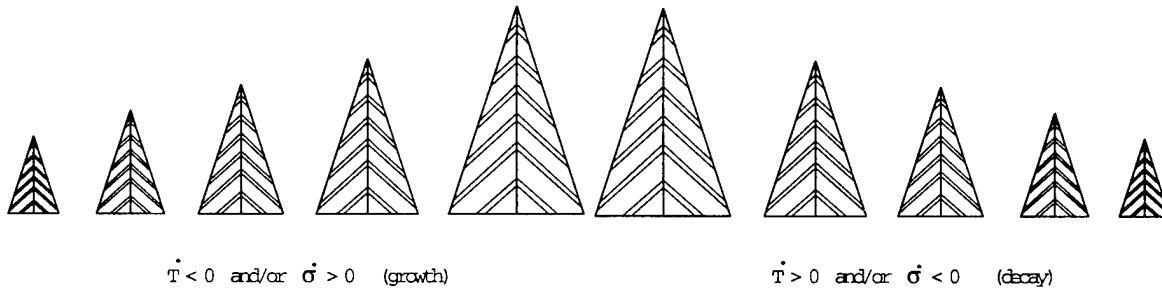


Figure 2.3: Product wedge. The upper diagram shows the progression of the martensite (arrow shape figures) in the austenite matrix (solid background) under the action of external stimuli. Whereas, the lower diagram shows the depletion of the martensite (arrow shape figures) in the austenite matrix (solid background) under the action of external stimuli.

For either the forward or reverse transformation eventually the sum of the chemical and non-chemical free energies approach a certain minimum value and growth is arrested and the transformation is complete.

For the determination of when transformations initiate, the space parameterized by stress and temperature is commonly used, instead of the space parameterized by free energy and temperature. The stress-temperature space is referred to as the phase space and is depicted in Figure 2.4 for tensile states of stress .

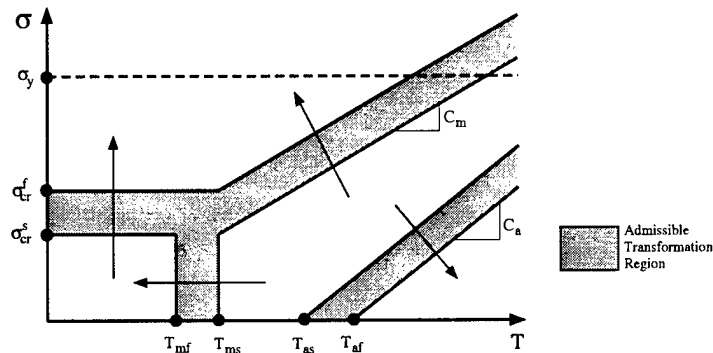


Figure 2.4: Phase space diagram depicting transformation zones and their associated values of stress and temperature for activation.

In Figure 2.4 the arrows indicate the directionality for an active transformation, while  $\sigma_{cr}^s$  and  $\sigma_{cr}^f$  denote the critical start and finish stress of a martensite transformation and  $C_m$  and  $C_a$  represent of the slope of the transformation lines. The transformation temperatures,  $T_{mf}$ ,  $T_{ms}$ ,  $T_{as}$  and  $T_{af}$  indicate the start and finish temperature at zero stress for martensite and austenite, respectively. Lastly,  $\sigma_y$  indicates the value of stress above which plastic slip will occur. Dependant upon the path taken within the phase space, certain characteristic features of the stress-strain space ( $\sigma - \varepsilon$ ) will be manifested. Further discussion of various paths is addressed in the following sections.

## 2.4 Shape Memory Effect

If a martensite transformation is induced purely by a thermal field below a critical temperature,  $T_{af}$ <sup>2</sup>, the resulting effect is called “self accommodation” or “twinning”. The ensuing multiple variants which form tend to average the overall deformation yielding a configuration similar to the parent configuration. Macroscopic deformation is not observable under such a transformation, neglecting the thermal expansion term.

If the martensite transformation is further induced by a kinetic field the multiple variants which are present will coalesce into one variant in the preferred direction of loading, in a process known as detwinning. Upon removal of the kinetic field, a permanent deforma-

<sup>2</sup>The symbol  $T_{af}$  denotes the critical temperature above which austenite is stable.

tion is retained until the specimen is heated above the critical temperature,  $T_{af}$ , leading to a recovery of the residual deformation. Note, to obtain a full reverse transformation, the martensite transformation must undergo a thermoelastic martensite transformation (i.e. crystallographically reversible) and deformation by slip must not occur. The process of an initial thermal/mechanical loading followed by a thermal loading to recover the transformation strain is typically termed the shape memory effect. The basic schematic is shown in Figure 2.5.

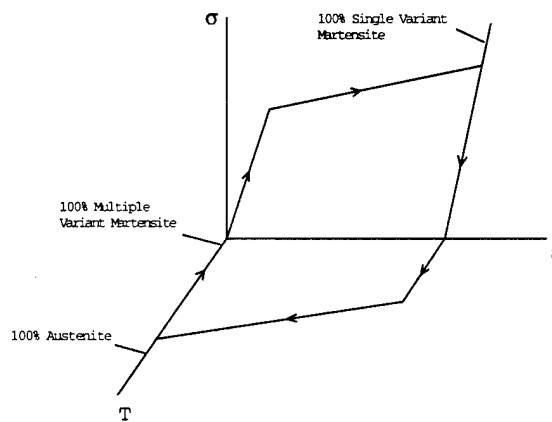


Figure 2.5: Shape memory effect. The process begins stress free at a high temperature and is cooled under zero load to form martensite. The specimen is then loaded and unloaded at constant temperature. Last, the specimen is heat to return to its original austenitic state.

## 2.5 Pseudoelastic Effect

When the thermal field is above the critical temperature  $T_{af}$  and the specimen is loaded mechanically above a critical stress level  $\sigma_{mf}$ <sup>3</sup>, the austenite crystal will transform into a single variant martensite oriented in the direction of loading, accompanied by a macroscopic strain as high as 11%. The strain is recovered upon removal of the mechanical load, since martensite is not stable at low stress and high temperatures. Typically this type of transformation is called pseudoelasticity, since the behavior is such that the material returns to

<sup>3</sup>The symbol  $\sigma_{mf}$  denotes the critical stress above which only martensite is stable.

its initial configuration upon removal of the loading. The basic schematic is shown in Figure 2.6

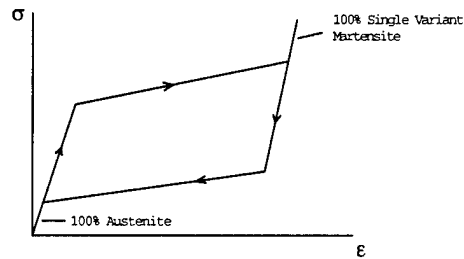


Figure 2.6: Pseudoelastic process begins stress free at a high temperature and is then loaded to a martensitic state and unloaded at constant temperature to its original austenitic state.

For a pseudoelastic transformation to obtain a full reverse transformation the martensite transformation must undergo a thermoelastic martensite transformation (i.e. crystallographically reversible) and deformation by slip must not occur.

## Chapter 3

# One Dimensional Shape Memory Alloy Model

In this chapter we develop the framework for a solid-solid phase transformation model. Internal variables are used to phenomenologically treat the response of the microstructure on a macroscopic level.

We begin with a review of the basic equation of a continuum. Following the review, linearized thermoelasticity is presented in one-dimension for subsequent use. The phenomenological constitutive equation describing the solid-solid phase transformation behavior is presented and discussed. To complete the constitutive equation for the model evolution equations for various transformation zones within the phase space are explicitly derived.

### 3.1 Continuum Mechanics

We shall give a brief introduction to the classical theory of continuum mechanics in the setting of nonlinear elasticity. For a more in-depth background in the area, an excellent exposition on the subject of continuum mechanics is given in TRUESDELL & NOLL [1992], as well as in GURTIN [1981]. This section is given for completeness and is used as a framework for later use.

### 3.1.1 Kinematics

#### Description of Motion

Let  $\kappa_o$ <sup>1</sup> denote the reference configuration of a deformable bounded body  $\mathcal{B} \subset \mathbb{R}^3$ . Identify a material point  $X$  with its place  $\mathbf{X}$  in the configuration  $\kappa_o$  by

$$\mathbf{X} = \kappa_o(X) . \quad (3.1)$$

Let the place of the material point  $X$  at time  $t$  within the body  $\mathcal{B}$  have a position vector  $\mathbf{x}$ , given by

$$\mathbf{x} = \widehat{\chi}(X, t) , \quad (3.2)$$

know as the *material description* of motion. Using (3.1) and (3.2) and assuming invertibility of  $\kappa_o$ , we can develop a relationship between the place of material point,  $\mathbf{x}$  to that of the material point at time  $t$  as

$$\mathbf{x} = \widehat{\chi}(\kappa_o^{-1}(\mathbf{X}), t) = \chi(\mathbf{X}, t) . \quad (3.3)$$

Thus, the material point  $X$  is mapped, upon deformation, into a spatial position  $\mathbf{x}$  in a current configuration at the current time by means of a single-valued, continuously differentiable mapping function called the *motion*. We shall also assume that the mapping  $\mathbf{X}$  to  $\mathbf{x}$  is one-to-one and onto, hence it possesses a unique inverse for all time  $t$ , which describes the *inverse motion*

$$\mathbf{X} = \chi^{-1}(\mathbf{x}, t) . \quad (3.4)$$

---

<sup>1</sup>In general, the subscript zero may not correspond to  $t = 0$  and  $\kappa_o$  need only be an admissible configuration, not necessarily one occupied by the body.

A necessary and sufficient condition for the invertibility of (3.3) to exist is for the Jacobian determinant of the mapping from  $\mathbf{X}$  to  $\mathbf{x}$  not vanish in an  $\epsilon$  - neighborhood about any point within the body  $\mathcal{B}$

$$J = \left| \frac{\partial \mathbf{x}}{\partial \mathbf{X}} \right| \neq 0 . \quad (3.5)$$

We shall also impose the physical restriction that  $J > 0$ , ensuring that any two material points do not occupy the same position in space at the same time. The motion described in (3.3) is traditionally referred to as the *Referential or Lagrangian description* of motion, where  $\mathbf{X}$  and  $t$  are the independent variables, while (3.4) is called the *Spatial or Eulerian description* of motion, with  $\mathbf{x}$  and  $t$  as the independent variables.

## Deformation Gradients

From the motion described in (3.3) we define the *deformation gradient*  $\mathbf{F}$  relative to  $\mathbf{X}$  from some fixed reference configuration  $\kappa_o$  to a current configuration,  $\kappa_t$  as

$$\mathbf{F} = \frac{\partial \mathbf{x}}{\partial \mathbf{X}} . \quad (3.6)$$

We impose the following restrictions; that  $\infty > J = \det(\mathbf{F}) > 0$  to ensure that no region of volume about an  $\epsilon$  - neighborhood of a material point becomes zero or infinite upon deformation and the derivatives of  $\frac{\partial \mathbf{x}}{\partial \mathbf{X}}$  are continuous. The deformation gradient characterizes the transformation of a line element  $d\mathbf{X}$  at the place  $\mathbf{X} \in \kappa_o$  upon deformation to a line element  $d\mathbf{x}$  at the place  $\mathbf{x} \in \kappa_t$ . Similarly, from the inverse motion (3.4) we define the gradient  $\mathbf{f}$  relative to  $\mathbf{x}$  as

$$\mathbf{f} = \frac{\partial \mathbf{X}^{-1}}{\partial \mathbf{x}} , \quad (3.7)$$

again with the restrictions that  $\infty > J^{-1} = \det(\mathbf{f}) > 0$  and the derivatives of  $\frac{\partial \mathbf{X}^{-1}}{\partial \mathbf{x}}$  are continuous.

If we assume for convenience that the reference and current coordinate frames coincide, then the *displacement vector*  $\mathbf{u}$  from the two coordinate frames can be expressed as

$$\mathbf{u} = \mathbf{x} - \mathbf{X} . \quad (3.8)$$

Thus, the deformation gradient and its inverse may be cast in terms of displacements as

$$\mathbf{F} = \mathbf{I} + \frac{\partial \mathbf{u}}{\partial \mathbf{X}} = \mathbf{I} + \mathbf{H} \quad \text{and} \quad \mathbf{f} = \mathbf{I} - \frac{\partial \mathbf{u}}{\partial \mathbf{x}} = \mathbf{I} - \mathbf{h} , \quad (3.9)$$

where  $\mathbf{H}$  and  $\mathbf{h}$  are called the *Lagrangian and Eulerian* displacement gradients, respectfully. Defined as

$$\mathbf{H} = \mathbf{F} - \mathbf{I} \quad \text{and} \quad \mathbf{h} = \mathbf{I} - \mathbf{f} = \mathbf{H}\mathbf{F}^{-1} . \quad (3.10)$$

### Deformation and Strain Measures

To introduce a deformation measure we will examine the magnitude of a differential line segment

$$ds^2 = d\mathbf{x} \cdot d\mathbf{x} = (\mathbf{F}d\mathbf{X}) \cdot (\mathbf{F}d\mathbf{X}) = (\mathbf{F}\mathbf{N}) \cdot (\mathbf{F}d\mathbf{N})dS^2 , \quad (3.11)$$

$$\frac{ds^2}{dS^2} = \lambda^2 = \mathbf{N} \cdot \mathbf{F}^T \mathbf{F} \mathbf{N} = \mathbf{N} \cdot \mathbf{C} \mathbf{N} , \quad (3.12)$$

where  $\lambda$  is the stretch of the differential line element. Note from (3.12) that  $\mathbf{C}$  is a second order, symmetric, positive definite tensor, which is a common measure of deformation in the reference configuration called the *right Cauchy-Green deformation tensor* defined as

$$\mathbf{C} = \mathbf{F}^T \mathbf{F} . \quad (3.13)$$

Similar arguments can be used to obtain the symmetric positive definite second order tensor  $\mathbf{b}$ , which is a common measure of deformation in the current configuration called the *left Cauchy-Green deformation tensor* defined as

$$\mathbf{b} = \mathbf{F} \mathbf{F}^T . \quad (3.14)$$

When a motion is rigid, the line segment magnitudes  $dS$  and  $ds$  are equal and thus the motion is distance preserving. Since the line segments  $dS$  and  $ds$  are equal for a rigid motion, the two deformation measures are also equal and unity (i.e.  $\mathbf{C} = \mathbf{b} = \mathbf{I}$ ). We would expect a strain measure to vanish for such a motion. Hence, we shall introduce strain measures for the reference and current configurations. Using the difference of the magnitudes of the line segments squared as our measure of strain, we obtain

$$ds^2 - dS^2 = (\mathbf{C} - \mathbf{I}) d\mathbf{X} d\mathbf{X} = 2 \mathbf{E} d\mathbf{X} d\mathbf{X} , \quad (3.15)$$

where  $\mathbf{E}$  is known as the *Green or Lagrangian strain tensor*. Defined as

$$\mathbf{E} = \frac{1}{2} (\mathbf{C} - \mathbf{I}) . \quad (3.16)$$

Similarly, we can define a strain measure in the current configuration known as the *Almansi or Eulerian strain tensor* by

$$\mathbf{e} = \frac{1}{2} (\mathbf{I} - \mathbf{b}^{-1}) . \quad (3.17)$$

## Rotation and Stretch Tensors

Since the deformation gradient  $\mathbf{F}$  is non-singular by (3.5), the polar decomposition theorem states that there exist positive symmetric tensors  $\mathbf{U}$  and  $\mathbf{V}$ , and a proper orthogonal tensor  $\mathbf{R}$  such that

$$\mathbf{F} = \mathbf{R}\mathbf{U} = \mathbf{V}\mathbf{R} . \quad (3.18)$$

Moreover, the right and left polar decompositions are unique. Where the tensors  $\mathbf{U}$  and  $\mathbf{V}$  are called the *right and left stretch tensors* respectively, while  $\mathbf{R}$  is called the *rotation tensor*. Using (3.13), (3.14) and (3.18) we can relate the right Cauchy-Green deformation tensor  $\mathbf{C}$  to the right stretch  $\mathbf{U}$  and the left Cauchy-Green deformation tensor  $\mathbf{b}$  to the left stretch  $\mathbf{V}$  by

$$\mathbf{C} = \mathbf{U}^2 \quad \text{and} \quad \mathbf{b} = \mathbf{V}^2 . \quad (3.19)$$

We may also relate  $\mathbf{U}$  and  $\mathbf{V}$  by

$$\mathbf{V} = \mathbf{R}\mathbf{U}\mathbf{R}^T . \quad (3.20)$$

Note, as a consequence of the similarity transformation of (3.20),  $\mathbf{U}$  and  $\mathbf{V}$  have the same eigenvalues.

### 3.1.2 Balance Laws

#### Conservation of Mass

We assume there exists a function  $m(\Omega)$ , termed the mass of the body  $\Omega$  such that

$$m(\Omega) \geq 0 \quad (3.21)$$

where  $m(\Omega)$  is independent of the configuration  $\kappa_t$  of the body such that

$$\frac{d}{dt}m(\Omega) = 0 . \quad (3.22)$$

The function  $m(\Omega)$  may be expressed in terms of a density function (a scalar) field  $\rho$  defined for a particular configuration as

$$m(\Omega) = \int_{\kappa_t} \rho(\mathbf{x}, t) dv = 0 \quad (3.23)$$

where  $\mathbf{x}$  is the place occupied by the material point  $X$  in the configuration  $\kappa_t$ ,  $t$  is time,  $dv$  is the volume element corresponding to  $\kappa_t$  and  $\rho$  is the mass density of the body in the configuration  $\kappa_t$ , assumed to be smooth and continuous. Since  $m(\Omega)$  is independent of the configuration, we may express equation (3.23) as

$$\int_{\kappa_t} \rho(\mathbf{x}, t) dv = \int_{\kappa_0} \rho_0(\mathbf{X}, t_0) dV \quad (3.24)$$

for an arbitrary reference configuration  $\kappa_0$ , where  $\mathbf{X}$  is the place occupied by the material point  $X$  in the configuration  $\kappa_0$ ,  $dV$  is the volume element corresponding to  $\kappa_0$  and  $\rho_0$  is the mass density of the body in the configuration  $\kappa_0$ . Noting that (3.24) holds for an arbitrary body  $\Omega$  and the mass density is smooth and continuous, we may express the local form of (3.24) as

$$J\rho = \rho_0 \quad (3.25)$$

where we have used the relation  $dv = JdV$  which relates a material volume in the reference configuration  $\kappa_0$  to an arbitrary configuration  $\kappa_t$ ,  $J$  given in the previous section. We may take the time rate of change of (3.24) to yield

$$\frac{d}{dt} \int_{\kappa_t} \rho(\mathbf{x}, t) dv = 0 \quad (3.26)$$

or locally as

$$\dot{\rho} + \rho \operatorname{div} [\mathbf{v}] = 0 \quad (3.27)$$

where the superposed dot indicates the material time derivative. Equations (3.24) through (3.27) are all different forms of the conservation of mass.

### Linear and Angular Momentum

The balance of linear momentum is expressed as an equality between the rate of change of linear momentum of an arbitrary volume of the body to the resultant force acting on that volume or simply

$$\frac{d}{dt} \int_{\mathcal{P}} \mathbf{v} dm = \int_{\mathcal{P}} \mathbf{b} dm + \int_{\partial\mathcal{P}} \mathbf{t} da \quad (3.28)$$

where  $dm = \rho dv$  is the element of mass,  $da$  is the area element,  $\mathbf{v}$  is the velocity,  $\mathbf{b}$  is the body force per unit mass,  $\mathbf{t}$  is the contact force per unit area,  $\mathcal{P}$  is an arbitrary volume of the body  $\mathcal{B}$  and  $\partial\mathcal{P}$  is the boundary surface of  $\mathcal{P}$ .

Likewise, the balance of angular momentum is expressed as the balance between the rate of change of angular momentum for an arbitrary volume and the resultant moment of the force acting on that volume or

$$\frac{d}{dt} \int_{\mathcal{P}} \mathbf{x} \times \mathbf{v} dm = \int_{\mathcal{P}} \mathbf{x} \times \mathbf{b} dm + \int_{\partial\mathcal{P}} \mathbf{x} \times \mathbf{t} da \quad (3.29)$$

where  $\mathbf{x}$  is the position vector from the origin  $\mathbf{o}$ .

Recall Cauchy's theorem: There exists a 2<sup>nd</sup> order tensor field  $\mathbf{T}$  independent of  $\mathbf{n}$  such that

$$\mathbf{t}(\mathbf{x}, \mathbf{n}) = \mathbf{T}(\mathbf{x})\mathbf{n} \quad (3.30)$$

for all  $\mathbf{x} \in \mathcal{B}$  and for arbitrary unit vectors  $\mathbf{n}$ . The tensor  $\mathbf{T}$  is referred to as the Cauchy stress tensor.

Substituting (3.30) into (3.28) and utilizing the divergence theorem, the continuity of  $\rho$ ,  $\mathbf{b}$  and  $\mathbf{v}$  and assuming  $\mathbf{T}$  is once continuously differentiable we arrive at

$$\text{div}[\mathbf{T}^T] + \rho\mathbf{b} = \rho\dot{\mathbf{v}} \quad \text{in } \Omega \times I \quad (3.31)$$

where  $\Omega$  is the domain under consideration,  $\text{div}[\cdot]$  is the divergence operator with respect to the spatial configuration and  $I = [0, t]$  represents an interval of time.

Substitution of (3.27), (3.30) and (3.31) into (3.29) yields symmetry of the stress tensor

$$\mathbf{T}^T = \mathbf{T} \quad \text{in } \Omega \times I. \quad (3.32)$$

Upon application of Nanson's formula<sup>2</sup>, the resultant contact forces may be expressed in terms of the reference configuration and subsequently the local form of the balance of linear momentum is expressed as

$$\text{Div}[\mathbf{P}] + \rho_0\mathbf{B} = \rho_0\dot{\mathbf{V}} \quad \text{in } \Omega \times I \quad (3.33)$$

where  $\mathbf{P}$  is the first Piola-Kirchhoff stress,  $\mathbf{B}$  is the body force,  $\text{Div}[\cdot]$  is the divergence operator with respect to the reference configuration and  $\mathbf{V} = \dot{\boldsymbol{\kappa}}$  is the material velocity. While the local form of the balance of angular momentum is

$$\mathbf{FP} = \mathbf{P}^T\mathbf{F}^T \quad \text{in } \Omega \times I. \quad (3.34)$$

---

<sup>2</sup>Nanson's formula relates the reference and current area elements via  $\mathbf{n}da = J\mathbf{F}^{-T}\mathbf{N}dA$

## Balance of Energy

The balance of energy or the first law of thermodynamics is expressed as an equality between the rate of change of the internal energy plus the kinetic energy and the rate of working of the applied forces plus any heat energy entering the body

$$\frac{d}{dt} \int_{\mathcal{P}} \left( \rho e + \frac{1}{2} \rho \mathbf{v} \cdot \mathbf{v} \right) dv = \int_{\mathcal{P}} (\rho r + \rho \mathbf{b} \cdot \mathbf{v}) dv + \int_{\partial \mathcal{P}} (\mathbf{t} \cdot \mathbf{v} - h) da \quad (3.35)$$

where  $\rho$  is the current mass density,  $e$  is the specific internal energy,  $\mathbf{v}$  is the velocity,  $r$  specific heat supply,  $\mathbf{b}$  is the body force per unit mass,  $\mathbf{t}$  is the contact force per unit area,  $h = \mathbf{q} \cdot \mathbf{n}$  is the heat flux across the boundary surface,  $\mathcal{P}$  is an arbitrary volume of the body  $\mathcal{B}$  and  $\partial \mathcal{P}$  is the boundary surface of  $\mathcal{P}$ .

Utilizing the conservation of mass, the balance of linear momentum, Cauchy's theorem, the transport theorem and the divergence theorem we obtain

$$\int_{\mathcal{P}} (\mathbf{T} : \mathbf{L} - \rho \dot{e} + \rho r - \text{div} [\mathbf{q}]) dv = 0 \quad (3.36)$$

where  $\mathbf{L}$  is the spatial velocity gradient.

Since (3.36) holds for an arbitrary volume  $\mathcal{P}$  of the body  $\mathcal{B}$  and we assume continuity of the arguments within the integrand, we obtain the local form for the balance of energy

$$\mathbf{T} : \mathbf{L} - \rho \dot{e} + \rho r - \text{div} [\mathbf{q}] = 0 \quad \text{in } \Omega \times I \quad (3.37)$$

where the the first term above is referred to as the stress or mechanical power. An alternative material form for the balance of energy expressed in terms of entropy is given as

$$(\dot{T}\eta) = -\text{Div} [\mathbf{Q}] + R \quad (3.38)$$

where  $T$  is the thermal field,  $\eta$  is the entropy,  $\mathbf{Q}$  is the nominal heat flux and  $R$  is the heat supply. Lastly, the Clausius-Duhem form for the second law of thermodynamics is expressed as

$$\mathbf{P} : \dot{\mathbf{F}} + T\dot{\eta} - \dot{e} - \frac{1}{T}\text{Grad}[T] \cdot \mathbf{Q} . \quad (3.39)$$

## 3.2 Linearized Thermoelasticity

We consider the linearization of the kinematic quantities from the previous section; for the following developments see Appendix D for further discussion. Note that all the stress measures are equivalent for the linearized theory and we will therefore use  $\boldsymbol{\sigma}$  to represent the stress tensor.

Recall the local form of the balance of linear momentum may be expressed as

$$\rho \dot{\mathbf{v}} = \text{div}[\boldsymbol{\sigma}] + \rho \mathbf{b} \quad \text{in } \Omega \times I \quad (3.40)$$

while the balance of angular momentum leads to symmetry of the stress tensor

$$\boldsymbol{\sigma} = \boldsymbol{\sigma}^T \quad \text{in } \Omega \times I \quad (3.41)$$

where  $\rho > 0$  is the density,  $\dot{\mathbf{v}}$  is the acceleration and  $\mathbf{b}$  is the body force. The local form of the balance of energy or first law of thermodynamics may be expressed as

$$\rho \dot{e} = -\text{div}[\mathbf{q}] + \boldsymbol{\sigma} : \dot{\boldsymbol{\epsilon}} + \rho r \quad \text{in } \Omega \times I \quad (3.42)$$

where  $e$  is the internal energy,  $\mathbf{q}$  is the heat flux,  $\boldsymbol{\epsilon}$  is the infinitesimal strain tensor and  $r$  denotes the heat supply. The local form of the second law of thermodynamics is

$$\rho\dot{\eta} + \operatorname{div} \left[ \frac{\mathbf{q}}{T} \right] - \rho \frac{r}{T} \geq 0 \quad \text{in } \Omega \times I \quad (3.43)$$

where  $\eta$  is the entropy and  $\theta$  is the absolute temperature. The Clausius-Duhem inequality is obtained by eliminating the heat source term,  $r$ , from (3.42) by substituting from (3.43) to obtain

$$\underbrace{\rho T \dot{\eta} - \rho \dot{e} + \boldsymbol{\sigma} : \dot{\boldsymbol{\varepsilon}}}_{\mathcal{D}_{loc}} - \underbrace{\frac{1}{T} \operatorname{grad} [T] \cdot \mathbf{q}}_{\mathcal{D}_{con}} \geq 0 \quad \text{in } \Omega \times I \quad (3.44)$$

where  $\mathcal{D}_{loc}$  represents the local or internal dissipation and  $\mathcal{D}_{con}$  the dissipation due to heat conduction after TRUESDELL & NOLL [1992]. Incorporating a generic form for the internal energy,  $e = \widehat{e}(\varepsilon, \eta, \boldsymbol{\xi}; \mathbf{x})$  we obtain the time derivative of the internal energy as

$$\dot{e} = \frac{\partial \widehat{e}}{\partial \varepsilon} : \dot{\boldsymbol{\varepsilon}} + \frac{\partial \widehat{e}}{\partial \eta} \dot{\eta} + \frac{\partial \widehat{e}}{\partial \boldsymbol{\xi}} \cdot \dot{\boldsymbol{\xi}} \quad (3.45)$$

where  $\boldsymbol{\xi}$  represents a general set of internal variables representing the inelastic response of the material. Substituting (3.45) into (3.44) yields

$$\left( \rho \theta - \frac{\partial \widehat{e}}{\partial \eta} \right) \dot{\eta} + \left( \boldsymbol{\sigma} - \frac{\partial \widehat{e}}{\partial \varepsilon} \right) : \dot{\boldsymbol{\varepsilon}} - \frac{\partial \widehat{e}}{\partial \boldsymbol{\xi}} \cdot \dot{\boldsymbol{\xi}} - \frac{1}{\theta} \operatorname{grad} [\theta] \cdot \mathbf{q} \geq 0. \quad (3.46)$$

Assuming Fourier's law for the constitutive equation for the heat flux,  $\mathbf{q} = -\kappa \operatorname{grad} [\theta]$ , the heat conduction dissipation is nonnegative,  $\mathcal{D}_{con} \geq 0$ . Noting that (3.46) is linear in  $\dot{\eta}$ ,  $\dot{\boldsymbol{\varepsilon}}$  and  $\dot{\boldsymbol{\xi}}$ , independent of their arguments and that the dissipation inequality must hold for all admissible processes we obtain

$$\rho T = \frac{\partial \widehat{e}}{\partial \eta}, \quad \boldsymbol{\sigma} = \frac{\partial \widehat{e}}{\partial \varepsilon} \quad \text{and} \quad - \frac{\partial \widehat{e}}{\partial \boldsymbol{\xi}} \cdot \dot{\boldsymbol{\xi}} \geq 0. \quad (3.47)$$

We introduce an alternative form for the balance of energy for subsequent use when casting the balance equations into a numerical setting<sup>3</sup>. Substituting the definition for  $\mathcal{D}_{loc}$  into (3.42) results in

$$\rho T \dot{\eta} = -\text{div} [\mathbf{q}] + \rho r + \mathcal{D}_{loc} \quad \text{in } \Omega \times I . \quad (3.48)$$

Introduce the Helmholtz free energy density

$$\psi = \widehat{\psi}(\boldsymbol{\varepsilon}, T, \boldsymbol{\xi}; \mathbf{x}) = \widehat{e}(\boldsymbol{\varepsilon}, \eta, \boldsymbol{\xi}; \mathbf{x}) - T\eta . \quad (3.49)$$

Substituting (3.49) into the constitutive equations (3.47) yields

$$\rho\eta = -\frac{\partial \widehat{\psi}}{\partial T}, \quad \boldsymbol{\sigma} = \frac{\partial \widehat{\psi}}{\partial \boldsymbol{\varepsilon}} \quad (3.50)$$

Taking the time derivative of the entropy results in

$$\dot{\eta} = - \left[ \frac{\partial^2 \widehat{\psi}}{\partial \boldsymbol{\varepsilon} \partial T} : \dot{\boldsymbol{\varepsilon}} + \frac{\partial^2 \widehat{\psi}}{\partial T \partial T} \dot{T} + \frac{\partial^2 \widehat{\psi}}{\partial \boldsymbol{\xi} \partial T} \cdot \dot{\boldsymbol{\xi}} \right] . \quad (3.51)$$

Substituting (3.51) into (3.48) yields

$$\begin{aligned} -\rho T \frac{\partial^2 \widehat{\psi}}{\partial T \partial T} \dot{T} &= -\text{div} [\mathbf{q}] + \rho r + \mathcal{D}_{loc} + T \frac{\partial^2 \widehat{\psi}}{\partial \boldsymbol{\varepsilon} \partial T} : \dot{\boldsymbol{\varepsilon}} + T \frac{\partial^2 \widehat{\psi}}{\partial \boldsymbol{\xi} \partial T} \dot{\boldsymbol{\xi}} \\ c \dot{T} &= -\text{div} [\mathbf{q}] + \rho r + \mathcal{D}_{loc} - H \end{aligned} \quad (3.52)$$

---

<sup>3</sup>Typically, algorithms found in the literature for coupled thermomechanical problems consider the motion and the temperature as the independent variables.

where  $c = T \frac{\partial^2 \hat{\psi}}{\partial T \partial T} > 0$  is referred to as the heat capacity and  $H = T \frac{\partial^2 \hat{\psi}}{\partial \epsilon \partial T} : \dot{\epsilon} + T \frac{\partial^2 \hat{\psi}}{\partial \xi \partial T} \dot{\xi}$  is the structural heating.

Specializing the above results to a one-dimensional bar, neglecting inertia and transient effects, we obtain

$$\begin{aligned} \sigma_{,x} + \rho b &= 0 \\ -q_{,x} + \rho r + \mathcal{D}_{loc} - H &= 0 \quad \text{in } \Omega \times I \end{aligned} \quad (3.53)$$

The respective boundary conditions for (3.53) are given as

$$\begin{aligned} u &= \bar{u} \quad \text{on } \Gamma_u \quad \text{and} \quad T = \bar{T} \quad \text{on } \Gamma_T \\ \sigma &= \bar{\sigma} \quad \text{on } \Gamma_\sigma \quad \text{and} \quad q = \bar{q} \quad \text{on } \Gamma_q \end{aligned} \quad (3.54)$$

where we have decomposed the boundary into two parts for each problem

$$\Gamma = \overline{\Gamma_u \cup \Gamma_\sigma} = \overline{\Gamma_T \cup \Gamma_q} \quad \text{and} \quad \Gamma_u \cap \Gamma_\sigma = \Gamma_T \cap \Gamma_q = \emptyset. \quad (3.55)$$

When supplemented with the proper boundary conditions (3.54), the balance laws (3.53) constitute a Boundary Value Problem.

### 3.3 Constitutive Equation

To complete the boundary value problem for the linearized theory of thermoelasticity we shall assume that the one-dimensional stress response function has the form

$$\sigma = E [\epsilon - \epsilon_L (\xi^+ - \xi^-) - \alpha (T - T_0)] \quad (3.56)$$

where  $\sigma$  is the stress,  $E$  is the elastic modulus,  $\epsilon$  is the total strain,  $\epsilon_L$  is the maximum residual strain obtained by detwinning multiple variant martensite (Bain or transformation

strain),  $\xi^+$  and  $\xi^-$  are the volume fractions of the positive and negative variants of the martensite twins ACHENBACH ET.AL. [1986] (see Figure 3.1),  $\alpha$  is the coefficient of thermal expansion and  $T$  and  $T_0$  are the current and reference temperature fields respectfully.

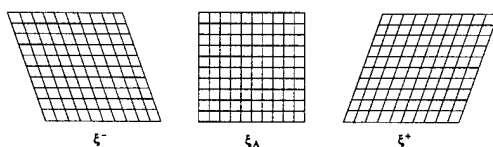


Figure 3.1: Variants associated with various lattice configurations.

**Remark 3.1.**

1. For any state, the simple algebraic relation holds  $\xi^+ + \xi^- + \xi_A = 1$ , where  $\xi_A$  represents the volume fraction of austenite present. Note that the total martensite fraction is the sum of the variants  $\xi = \xi^+ + \xi^-$ , while the absence of both  $\xi^+$  and  $\xi^-$  indicate the material is completely austenite.
2. For states where  $\xi^+ = \xi^-$  the material is considered to be in a self-accommodating state in which that material is 100% multiple variant martensite. Although its configuration is similar to 100% austenite with regard to the overall deformation on the crystal being zero, the crystal structure is not the same.
3. For a one-dimensional state we may accurately capture the behavior of the phase transformation using two internal variables, namely  $\xi^+$  and  $\xi^-$ . For higher dimensions, the underlining physics is more complicated and thus additional internal variables or variants should be accounted for; see BOYD & LAGOUDAS [1996A,B].
4. Different authors TANAKA [1986], LIANG & ROGERS. [1990], BRINSON [1993] AND BRINSON ET. AL. [1993] have utilized linear mixture rules for the elastic material modulus  $E = E_a + \xi(E_m - E_a)$  and coefficient of thermal expansion  $\alpha = \alpha_a + \xi(\alpha_m - \alpha_a)$ , where  $E_a$ ,  $E_m$ ,  $\alpha_a$  and  $\alpha_m$  are the elastic moduli and thermal coefficient of expansion for pure austenite and martensite. The mixture rules enhance the model by accounting for different material properties at each pure state. The introduction of these mixture rules may or may not be justifiable depending upon the particular alloy. However, the addition of these mixtures rules presents no difficulty in the present formulation; for simplicity we will assume the moduli to be constant.

### 3.4 Evolution Equations

In the following subsections, we develop explicit expression for the evolution equations for various regions within the phase diagram.

To account for both tensile and compressive behavior, we consider a mapping of the standard phase diagram in the tensile stress region into the compressive region. For the present work, the transformation parameters are denoted with either a  $^+$  or a  $^-$  representing the parameters in the tensile and compressive regions of stress, respectively. The ability to differentiate between the various transformation parameters enables the model to qualitatively capture the behavior observed in experimental data.

#### 3.4.1 Production of Austenite

Since austenite has only one form (variant), it is sufficient to consider the evolution of the total martensite fraction. The positive and negative variants are assumed to evolve proportional to the total martensite fraction. The evolution of the total martensite fraction may be expressed in an integrated form as a linear interpolation between the start and finish transformation lines within the phase transformation region shown in Figure 3.2

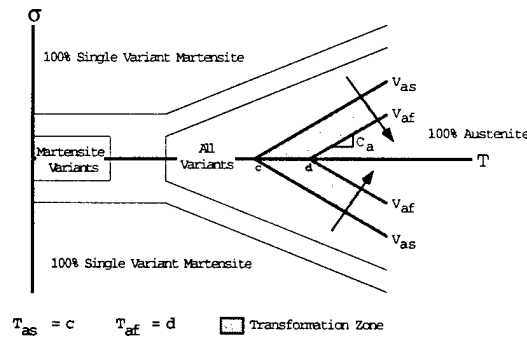


Figure 3.2: Admissible transformation regions for the production of austenite. The points 'c' and 'd' denote the start and finish temperatures for the transformation, while  $V_{as}$  and  $V_{af}$  are the start and finish lines for the transformation and the directionality of the evolution is indicated by the arrows.

The evolution equation is expressed as follows:

$$\xi = \xi_p - \xi_p \left( \frac{\sigma - V_{as}}{V_{af} - V_{as}} \right) . \quad (3.57)$$

The parameter  $\xi_p$  is introduced to account for cyclic behavior within the transformation zone and represents the maximum value of  $\xi$  for any previous loading history. The parameters  $V_{as}$  and  $V_{af}$  denote the critical values of stress between which the phase transformation occurs at a fixed temperature, where the subscripts  $as$  and  $af$  designate stress values on modified (by the initial conditions) austenite start and finish lines, respectively. The starting value of the phase transformation is taken to be a function of the initial fractions present, while the finish value is taken to be constant; thus

$$\begin{aligned} V_{as} &= \sigma_{as} + \frac{\xi_p - \xi_0}{1 - \xi_0} (\sigma_{af} - \sigma_{as}) \\ V_{af} &= \sigma_{af} \end{aligned} \quad (3.58)$$

where  $\xi_0$  represents the initial fraction of martensite for the first occurrence of the transformation and  $\sigma_{as}$  and  $\sigma_{af}$  are defined from the virgin phase transformation lines in the stress-temperature space as

$$\sigma_{as} = C_a (T - T_{as}) \quad \text{and} \quad \sigma_{af} = C_a (T - T_{af}) \quad (3.59)$$

and  $C_a$  is the slope of the transformation lines, assumed fixed. The evolution of the positive and negative variants are assumed to occur in proportion to their existence at the beginning of the phase transformation

$$\xi^+ = \frac{\xi_p^+}{\xi_p} \xi \quad \text{and} \quad \xi^- = \frac{\xi_p^-}{\xi_p} \xi . \quad (3.60)$$

**Remark 3.2.**

- To accommodate experimental data the transformation parameters ( $C_a, V_{as}, V_{af}$ ) may be altered to reflect differing values in tension and compression.

## State and Internal Variables

To complete the model for the production of austenite, explicit expressions for the state and internal variables are derived below. In addition, material tangents will also be derived in order to facilitate coding the model into a numerical setting, such as the finite element method where a tangent matrix is required for a solution of the global variables.

If the phase transformation is occurring, the inelastic state and internal variables must be determined. Utilizing the constitutive equation (3.56) and the evolution equation for the production of austenite (3.57), we may solve these two linear equations for the stress and martensite fractions during the inelastic process:

$$\begin{aligned}\sigma &= \frac{E}{b_0} \left( \varepsilon - \varepsilon^p - \varepsilon_L [\xi_p^+ - \xi_p^-] + [b_0 - 1] \frac{V_{as}}{E} - \alpha [T - T_0] \right) \\ \xi &= \xi_p - \xi_p \left( \frac{\sigma - V_{as}}{V_{af} - V_{as}} \right)\end{aligned}\quad (3.61)$$

where

$$b_0 = 1 + \frac{\varepsilon_L E}{\xi_p} (\xi_p^+ - \xi_p^-) \left( \frac{-\xi_p}{V_{af} - V_{as}} \right) \quad (3.62)$$

whereas, during an elastic process we simply have

$$\begin{aligned}\sigma &= E (\varepsilon - \varepsilon^p - \varepsilon_L [\xi_p^+ - \xi_p^-] - \alpha [T - T_0]) \\ \xi &= \xi_p.\end{aligned}\quad (3.63)$$

To obtain the mechanical and thermal material moduli for the inelastic case we take the variation of the stress response (3.61)<sub>1</sub>. If  $\delta$  is taken as the variation operator, then:

$$\delta\sigma = \frac{\partial\sigma}{\partial\varepsilon} \delta\varepsilon + \frac{\partial\sigma}{\partial T} \delta T = \frac{E}{b_0} \delta\varepsilon + \frac{E}{b_0} \left[ (b_0 - 1) \frac{C_a}{E} - \alpha \right] \delta T. \quad (3.64)$$

For the case of an elastic process we simply obtain

$$\delta\sigma = \frac{\partial\sigma}{\partial\varepsilon}\delta\varepsilon + \frac{\partial\sigma}{\partial T}\delta T = E\delta\varepsilon - \alpha E\delta T. \quad (3.65)$$

### 3.4.2 Production of Positive Single Variant Martensite

For the production of positive single variant martensite it is sufficient to consider the evolution of one of the variants, namely the positive variant. The remaining negative variant is then evolved proportional to the positive variant martensite. The evolution of the single positive variant martensite fraction may be expressed in an integrated form as a linear interpolation within the phase transformation shown in Figure 3.3:

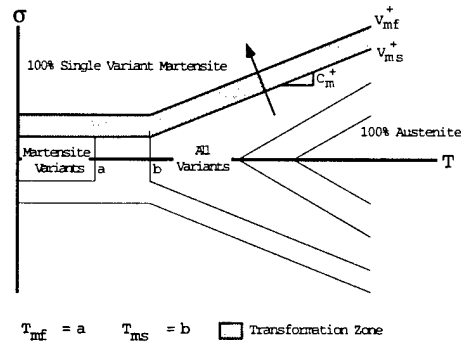


Figure 3.3: Admissible transformation regions for the production of positive single variant martensite. The point 'b' denotes the temperature below which austenite is not stable. The parameters  $V_{ms}^+$  and  $V_{mf}^+$  are the start and finish lines for the transformation and the directionality of the transformation is indicated by the arrow.

$$\xi^+ = 1 + (1 - \xi_p^+) \left( \frac{\sigma - V_{mf}^+}{V_{mf}^+ - V_{ms}^+} \right). \quad (3.66)$$

The parameter  $\xi_p^+$  is introduced to account for cyclic behavior within the transformation zone and represents the maximum value of  $\xi^+$  for the previous loading history. The parameters

$V_{ms}^+$  and  $V_{mf}^+$  denote the critical values of stress between which the phase transformation occurs, where the subscripts  $ms$  and  $mf$  designate stress values on a modified (by the initial conditions) martensite start and finish lines, respectively. The starting value of the phase transformation is taken to be a function of the initial fractions present, while the finish value is taken to be constant; thus

$$\begin{aligned}
 V_{ms}^+ &= \bar{V}_{ms}^+ + \frac{\xi_p^+ - \xi_0^+}{1 - \xi_0^+} (V_{mf}^+ - \bar{V}_{ms}^+) & (3.67) \\
 V_{mf}^+ &= \sigma_{mf} \\
 \bar{V}_{ms}^+ &= \sigma_{ms} + (\mathcal{H}(\sigma)\xi_0^+ + [1 - \mathcal{H}(\sigma)]\xi_0^- - \min[\xi_0^+, \xi_0^-]) (\sigma_{mf} - \sigma_{ms})
 \end{aligned}$$

where  $\xi_0^+$  represents the initial fraction of martensite for the first occurrence of the transformation,  $\mathcal{H}(\sigma)$  is the step function defined as

$$\mathcal{H}(\sigma) = \begin{cases} 0, & \sigma < 0 \\ 1, & \sigma > 0 \end{cases} \quad (3.68)$$

and  $\sigma_{ms}$  and  $\sigma_{mf}$  are defined from the virgin phase transformation lines in the stress-temperature space as

$$\sigma_{ms} = \sigma_{cr}^s + C_m \langle T - T_{ms} \rangle \quad \text{and} \quad \sigma_{mf} = \sigma_{cr}^f + C_m \langle T - T_{ms} \rangle \quad (3.69)$$

where the Macauley bracket  $\langle \cdot \rangle$  is defined by

$$\langle a \rangle = \begin{cases} 0, & a \leq 0 \\ a, & a > 0 \end{cases} \quad (3.70)$$

and  $C_m$  is the slope of the transformation lines, assumed fixed. The evolution of the negative variant is assumed to occur in proportion to its existence at the beginning of the phase transformation:

$$\xi^- = \left( \frac{1 - \xi^+}{1 - \xi_p^+} \right) \xi_p^- . \quad (3.71)$$

**Remark 3.3.**

- In equation (3.67)<sub>3</sub> the second term on the right hand side is introduced to ensure that only the single variant states effect the initial critical stress.

**State and Internal Variables**

The model is completed by developing expressions for the state and internal variables and material tangents outlined below.

During this phase transformation, the inelastic state and internal variables must be determined. Utilizing the constitutive equation (3.56) and the evolution equation for the production of positive single variant martensite (3.66), we may explicitly determine the stress and martensite fractions during the inelastic process as

$$\begin{aligned} \sigma &= \frac{E}{b_0} \left( \varepsilon - \varepsilon^p - \varepsilon_L + (b_0 - 1) \frac{V_{mf}^+}{E} - \alpha[T - T_0] \right) \\ \xi^+ &= 1 + (1 - \xi_p^+) \left( \frac{\sigma - V_{mf}^+}{V_{mf}^+ - V_{ms}^+} \right) \end{aligned} \quad (3.72)$$

where

$$b_0 = 1 + \varepsilon_L E \left( \frac{1 - \xi_p^+ + \xi_p^-}{V_{mf}^+ - V_{ms}^+} \right) . \quad (3.73)$$

whereas, for the elastic state we simply have

$$\begin{aligned}\sigma &= E (\varepsilon - \varepsilon^p - \varepsilon_L [\xi_p^+ - \xi_p^-] - \alpha [T - T_0]) \\ \xi^+ &= \xi_p^+ .\end{aligned}\quad (3.74)$$

To obtain the mechanical and thermal material moduli for the inelastic case we take the variation of the stress response (3.72)<sub>1</sub>

$$\delta\sigma = \frac{\partial\sigma}{\partial\varepsilon}\delta\varepsilon + \frac{\partial\sigma}{\partial T}\delta T = \frac{E}{b_0}\delta\varepsilon + \frac{E}{b_0} \left[ (b_0 - 1) \frac{C_m}{E} (T - T_{ms}) - \alpha \right] \delta T . \quad (3.75)$$

For the case of an elastic state we simply obtain

$$\delta\sigma = \frac{\partial\sigma}{\partial\varepsilon}\delta\varepsilon + \frac{\partial\sigma}{\partial T}\delta T = E\delta\varepsilon - \alpha E\delta T . \quad (3.76)$$

### 3.4.3 Production of Negative Single Variant Martensite

For the production of negative single variant martensite it is sufficient to consider the evolution of one of the variants, namely the negative variant. The remaining positive variant is then evolved proportional to the single negative variant martensite. The evolution of the single negative variant martensite fraction may be expressed in an integrated form as a linear interpolation within the phase transformation shown in Figure 3.4.

The evolution equation is expressed as follows

$$\xi^- = 1 + (1 - \xi_p^-) \left( \frac{\sigma - V_{mf}^-}{V_{mf}^- - V_{ms}^-} \right) . \quad (3.77)$$

The parameter  $\xi_p^-$  is introduced to account for cyclic behavior within the transformation zone and represents the maximum value of  $\xi^-$  for the previous loading history. The parameters  $V_{ms}^-$  and  $V_{mf}^-$  are defined as

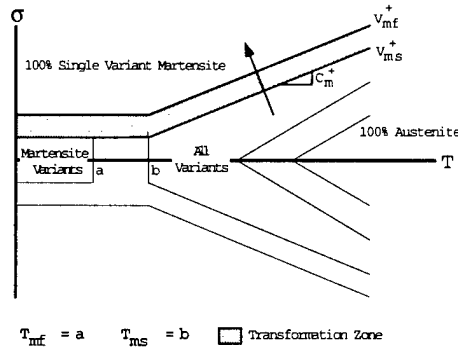


Figure 3.4: Admissible transformation regions for the production of positive single variant martensite. The point 'b' denotes the temperature below which austenite is not stable. The parameters  $V_{ms}^+$  and  $V_{mf}^+$  are the start and finish lines for the transformation and the directionality of the transformation is indicated by the arrow.

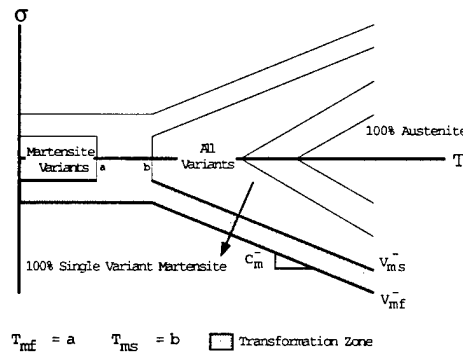


Figure 3.5: Admissible transformation regions for the production of negative single variant martensite. The parameters  $V_{ms}^-$  and  $V_{mf}^-$  indicate the start and finish lines for the transformation and the direction for the production of single variant martensite is depicted by the arrow.

$$V_{ms}^- = \bar{V}_{ms}^- + \frac{\xi_p^- - \xi_0^-}{1 - \xi_0^-} (V_{mf}^- - \bar{V}_{ms}^-) \quad (3.78)$$

$$V_{mf}^- = \sigma_{mf}$$

$$\bar{V}_{ms}^- = \sigma_{ms} + (\mathcal{H}(\sigma)\xi_0^- + [1 - \mathcal{H}(\sigma)]\xi_0^- - \min[\xi_0^-, \xi_0^-]) (\sigma_{mf} - \sigma_{ms}) .$$

The evolution of the positive variant is assumed to occur in proportion to its existence at the beginning of the phase transformation

$$\xi^+ = \left( \frac{1 - \xi^-}{1 - \xi_p^-} \right) \xi_p^+ . \quad (3.79)$$

### State and Internal Variables

The state and internal variables and material tangents are developed below to complete the model.

During this phase transformation, the inelastic state and internal variables must be determined. Utilizing the constitutive equation (3.56) and the evolution equation for the production of negative single variant martensite (3.77), we may explicitly determine the stress and martensite fractions during the inelastic process as

$$\begin{aligned} \sigma &= \frac{E}{b_0} \left( \varepsilon - \varepsilon^p + \varepsilon_L + (b_0 - 1) \frac{V_{mf}^-}{E} - \alpha[T - T_0] \right) \\ \xi^- &= 1 + (1 - \xi_p^-) \left( \frac{\sigma - V_{mf}^-}{V_{mf}^- - V_{ms}^-} \right) \end{aligned} \quad (3.80)$$

where

$$b_0 = 1 - \varepsilon_L E \left( \frac{1 + \xi_p^+ - \xi_p^-}{V_{mf}^- - V_{ms}^-} \right) \quad (3.81)$$

whereas, for the elastic state we simply have

$$\begin{aligned} \sigma &= E \left( \varepsilon - \varepsilon^p - \varepsilon_L [\xi_p^+ - \xi_p^-] - \alpha[T - T_0] \right) \\ \xi^- &= \xi_p^- . \end{aligned} \quad (3.82)$$

To obtain the mechanical and thermal material moduli for the inelastic case we take the variation of the stress response (3.80)<sub>1</sub>

$$\delta\sigma = \frac{\partial\sigma}{\partial\varepsilon}\delta\varepsilon + \frac{\partial\sigma}{\partial T}\delta T = \frac{E}{b_0}\delta\varepsilon + \frac{E}{b_0} \left[ (b_0 - 1) \frac{C_m}{E} \langle T - T_{ms} \rangle - \alpha \right] \delta T . \quad (3.83)$$

### 3.4.4 Production of Multiple Variant Martensite

Since multiple variant martensite has equally distributed proportions of positive and negative variants of martensite, from a zero initial state<sup>4</sup>, it is sufficient to consider the evolution of the total martensite fraction. The total positive and negative variants are then evolved proportional to the total martensite fraction present. The evolution of the total martensite fraction may be expressed in an integrated form as a linear interpolation within the phase transformation zone shown in Figure 3.6.

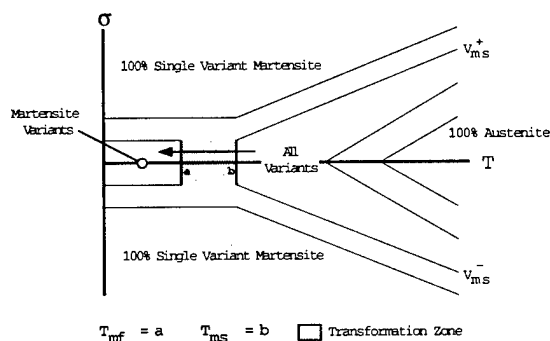


Figure 3.6: Admissible transformation regions for the production of multiple variant martensite. The points 'a' and 'b' denote the start and finish temperatures for the phase transformation and the direction of the evolution is depicted by the arrow.

The evolution equation for the production of multiple variant martensite is expressed as

$$\xi = 1 + (1 - \xi_p) \left( \frac{T - \theta_{mf}}{\theta_{mf} - \theta_{ms}} \right) . \quad (3.84)$$

<sup>4</sup>Producing multiple variant martensite from 100 % austenite.

The parameter  $\xi_p$  is introduced to account for cyclic behavior within the transformation zone and represents the maximum value of  $\xi$  for the previous loading history. The parameters  $\theta_{ms}$  and  $\theta_{mf}$  denote the critical values of temperature between which the phase transformation occurs, where the subscripts  $ms$  and  $mf$  designate temperature values on modified (by the initial conditions) martensite start and finish lines, respectively. The starting value of the phase transformation is taken to be a function of the initial fractions present, while the finish value is taken to be constant; thus

$$\begin{aligned}\theta_{ms} &= T_{ms} + \frac{\xi_p - \xi_0}{1 - \xi_0} (T_{mf} - T_{ms}) \\ \theta_{mf} &= T_{mf}\end{aligned}\tag{3.85}$$

where  $\xi_0$  represents the initial fraction of martensite for the first occurrence of the transformation and  $T_{ms}$  and  $T_{mf}$  are material parameters taken from the virgin phase transformation lines in the stress-temperature space.

The evolution of the positive and negative variants are assumed to occur in proportion to their existence at the beginning of the phase transformation

$$\xi^+ = \xi_p^+ + \frac{1}{2} (\xi - \xi_p) \quad \text{and} \quad \xi^- = \xi_p^- + \frac{1}{2} (\xi - \xi_p) .\tag{3.86}$$

### State and Internal Variables

The model is completed by deriving expressions for the state and internal variables and material tangents outlined below.

During this phase transformation, the inelastic state and internal variables must be determined. Note that the evolution equation for the production of multiple variant martensite (3.84) is independent of the stress field, hence we may simply calculate the martensite fraction (assuming a known temperature) and substitute those results into the constitutive equation (3.56) as

$$\xi = 1 + (1 - \xi_p) \left( \frac{T - \theta_{mf}}{\theta_{mf} - \theta_{ms}} \right) \quad (3.87)$$

$$\sigma = E (\varepsilon - \varepsilon^p - \varepsilon_L [\xi^+ - \xi^-] - \alpha [T - T_0]) .$$

To obtain the mechanical and thermal material moduli for the inelastic case we take the variation of the stress response (3.87)<sub>2</sub>

$$\delta\sigma = \frac{\partial\sigma}{\partial\varepsilon} \delta\varepsilon + \frac{\partial\sigma}{\partial T} \delta T = E\delta\varepsilon - \alpha E\delta T . \quad (3.88)$$

# Chapter 4

## Finite Element Developments

This section covers the algorithmic approximation of the constitutive theory in the setting of the finite element method. Due to the nature of the nested elastic and inelastic regions, the determination of when a transformation is active becomes paramount to the model's implementation. This detection procedure is known as state determination. An outline of the algorithmic procedure is described and discussed below.

Lastly, to examine the properties of the resulting equations the model is implemented within the context of line elements in the finite element method. Specifically, we numerically assess the behavior of a class of shape memory alloys with linear and non-linear kinematics for multi-dimensional truss bars and a two-dimensional beam.

### 4.1 State Determination

In this section we outline the procedure used for state determination at time  $t_{n+1}$  using information from the current global iterate  $(\cdot)_{n+1}^{(k+1)}$  and the previous time step  $(\cdot)_n$  for various phase transformations. Also note we consider that the temperature is given at time  $t_{n+1}$  by either a prescribed load history or solving the heat conduction problem.

The phase space diagram in Figure 2.4 has lead many researcher to use existing schemes for state determination, such as trial state methods in classical plasticity. Unfortunately, classical algorithms fail to determine the correct state even for simple simulations due to

the wide range of trial states. As an example, during the loading portion of a pseudoelastic process, both elastic and inelastic states are admissible, since the inelastic region is bounded by two elastic regions. Simply checking the trial value of stress with the “yield function” and its directionality will not guarantee the correct state.

We introduce a new algorithm which accounts for nested elastic and inelastic regimes. The underlining concept relies on the use of modified trial state variables and the determination of trial states within an admissible transformation region. The resulting trial states are checked for consistency with respect to the phase diagram, i.e. directionality and magnitude of the stress, temperature and internal variables (martensite fractions).

### 4.1.1 Production of Austenite

Consider the production of austenite with initial conditions at time  $t_n$  shown in Figure 4.1. Given a temperature increase to  $T_{n+1}$  we wish to determine the state for time  $t_{n+1}$ .

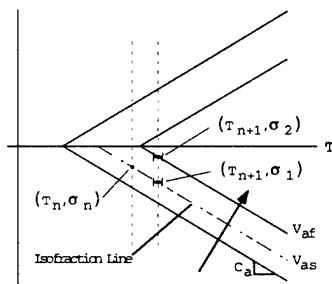


Figure 4.1: Bounds for martensite fraction in phase space. From  $t_n$  we may develop an isofraction line on the phase diagram, below which transformations are elastic.

For the production of austenite, we consider the state  $(T_n, \sigma_n)$  on the phase diagram in Figure 4.2 and two critical states  $(T_{n+1}, \sigma_1)$  and  $(T_{n+1}, \sigma_2)$  at time  $t_{n+1}$ . The pair  $(T_{n+1}, \sigma_1)$  corresponds to a point on the iso-fraction line, while the pair  $(T_{n+1}, \sigma_2)$  corresponds to the point at which the martensite transformation is completed. From these two points we see at time  $t_{n+1}$  there exist three possible regions for the solution, see Figure 4.2.

To determine the correct trajectory for the state at  $t_{n+1}$ , we evaluate the constitution for all three regions. The three possible choices are:

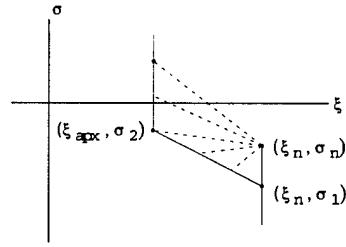


Figure 4.2: Possible trajectories in stress-strain space. We see that values of stress greater than  $\sigma_2$  and less than  $\sigma_1$  result in elastic states.

1. ( $\sigma < \sigma_1$  - Elastic State) Evaluate the constitution using the previous converged value for the internal variables:

$$\sigma = E \left( \varepsilon_{n+1}^{(k+1)} - \varepsilon_n^p - \varepsilon_L [\xi_n^+ - \xi_n^-] - \alpha [T_{n+1} - T_0] \right) \quad (4.1)$$

2. ( $\sigma_1 \leq \sigma \leq \sigma_2$  - Production of Austenite) Simultaneously solve for the constitution and the evolution:

$$\sigma = \frac{E}{b_0} \left( \varepsilon_{n+1}^{(k+1)} - \varepsilon_n^p - \varepsilon_L [\xi_{pn}^+ - \xi_{pn}^-] + [b_0 - 1] \frac{V_{as}}{E} - \alpha [T_{n+1} - T_0] \right) \quad (4.2)$$

$$\xi = \xi_{pn} - \xi_{pn} \left( \frac{\sigma - V_{as}}{V_{af} - V_{as}} \right)$$

3. ( $\sigma > \sigma_2$  - Elastic State) Evaluate the constitution assuming that the martensite transformation is completed:

$$\sigma = E \left( \varepsilon_{n+1}^{(k+1)} - \varepsilon_n^p - \varepsilon_L [\xi_{apx}^+ - \xi_{apx}^-] - \alpha [T_{n+1} - T_0] \right) \quad (4.3)$$

where

$$\xi_{apx} = \max \left\{ \xi_0 - \xi_0 \frac{\langle T - T_{as} \rangle}{T_{af} - T_{as}}, 0 \right\} \quad (4.4)$$

$$\xi_{apx}^+ = \xi_p^+ / \xi_p \xi_{apx}$$

$$\xi_{apx}^- = \xi_p^- / \xi_p \xi_{apx}$$

**Remark 4.1.**

- The fraction  $\xi_{apx}$  represents the maximum amount of martensite which may be transformed into austenite for a particular temperature  $T$  and initial conditions  $(\xi_0, \xi_p)$ .

For the production of austenite to occur  $T \geq T_{as} + (1 - \xi_0)(T_{af} - T_{as})$  and  $\xi_n > \xi_{apx}$ . If this criteria is met then paths 1, 2 and 3 are evaluated. The additional consistency checks on the directionality and magnitudes of the stress and the internal variables for each path are outlined below.

#### Path 1

- If  $\sigma > 0$  and  $\sigma \leq \sigma_{as} + (1 - \xi_n)(\sigma_{af} - \sigma_{as})$  then admissible.
- If  $\sigma < 0$  and  $\sigma \leq -\sigma_{as} - (1 - \xi_n)(\sigma_{af} - \sigma_{as})$  then admissible.

#### Path 2

- If  $\sigma > 0$ ,  $\sigma \leq V_{as}^+$ ,  $-d\sigma + C_a^+ dT > 0$  and  $\xi < \xi_n$  then admissible, where  $d\sigma = \sigma - \sigma_n$  and  $dT = T_{n+1} - T_n$ .
- If  $\sigma < 0$ ,  $V_{as}^- \leq \sigma$ ,  $d\sigma - C_a^- dT > 0$  and  $\xi < \xi_n$  then admissible.

#### Path 3

- If  $\sigma_n > 0$  and  $\sigma \leq \max[0, V_{af}^+]$  then admissible.
- If  $\sigma_n < 0$  and  $\sigma \geq \min[0, V_{af}^-]$  then admissible.

If multiple states are admissible we select the state which is closest to the previous converged state via distance metric in stress space. By choosing the closest state to the previous state we restrict the local behavior of the local constitution from returning spurious states. The metric is minimized using the admissible current states and the previous converged state, i.e.  $\sigma = \min_i [d(\sigma_n, \sigma_i)]$  where  $d(x, y) = |x - y|$ . The resulting state is returned to the element and the residual and tangent arrays are built.

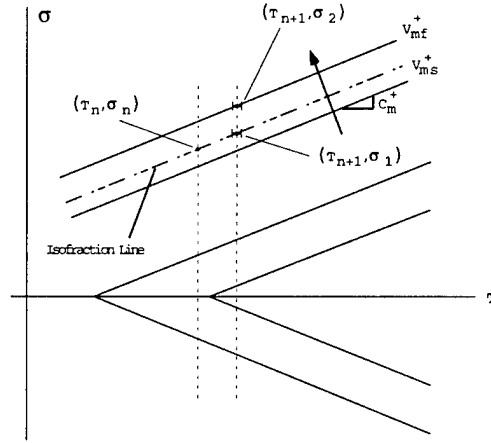


Figure 4.3: Bounds for martensite fraction in phase space. The parameters  $V_{ms}^+$  corresponds to the minimum value of stress required to initiate a transformation and the arrow indicates the direction of the transformation.

#### 4.1.2 Production of Positive Single Variant Martensite

Consider now the production of positive single variant martensite with initial conditions at time  $t_n$  shown in Figure 4.3. Given a temperature increase to  $T_{n+1}$  we wish to determine the state for time  $t_{n+1}$ .

For the production of single variant positive martensite we consider the state  $(T_n, \sigma_n)$  on the phase diagram in Figure 4.3 and two critical states  $(T_{n+1}, \sigma_1)$  and  $(T_{n+1}, \sigma_2)$  at time  $t_{n+1}$ . The pair  $(T_{n+1}, \sigma_1)$  corresponds to a point on the iso-fraction line, while the pair  $(T_{n+1}, \sigma_2)$  corresponds to the point at which the martensite transformation is completed. From these two points we see at time  $t_{n+1}$  there exists three possible regions for the solution, see Figure 4.4.

To determine the correct trajectory for the state at  $t_{n+1}$  we evaluate the constitution for all three regions. The three possible choices are:

1. ( $\sigma < \sigma_1$  - Elastic State) Evaluate the constitution using the previous converged value for the internal variables:

$$\sigma = E \left( \varepsilon_{n+1}^{(k+1)} - \varepsilon_n^p - \varepsilon_L [\xi_n^+ - \xi_n^-] - \alpha [T_{n+1} - T_0] \right) \quad (4.5)$$

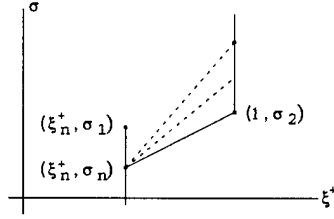


Figure 4.4: Possible trajectories in stress-fraction space. We observe that values of stress greater than  $\sigma_2$  and less than  $\sigma_n$  result in elastic states.

2. ( $\sigma_1 \leq \sigma \leq \sigma_2$  - Production of Single Variant Martensite) Simultaneously solve for the constitution and the evolution:

$$\sigma = \frac{E}{b_0} \left( \varepsilon_{n+1}^{(k+1)} - \varepsilon_n^p - \varepsilon_L + (b_0 - 1) \frac{V_{mf}^+}{E} - \alpha [T_{n+1} - T_0] \right) \quad (4.6)$$

$$\xi^+ = 1 + (1 - \xi_n^+) \left( \frac{\sigma - V_{mf}^+}{V_{mf}^+ - V_{ms}^+} \right)$$

3. 3B ( $\sigma > \sigma_2$  - Elastic State) Evaluate the constitution assuming that the martensite transformation is completed:

$$\sigma = E \left( \varepsilon_{n+1}^{(k+1)} - \varepsilon_n^p - \varepsilon_L - \alpha [T_{n+1} - T_0] \right) \quad (4.7)$$

For the production of positive single variant martensite to occur  $\xi_n^+ < 1$  and  $\sigma_n \geq 0$ . If this criteria is met then paths 1, 2 and 3 are evaluated. The additional consistency checks on the directionality and magnitudes of the stress and the internal variables for each path are outlined below.

#### Path 1

- If  $\sigma \leq \sigma_{ms} + \xi_n^+(\sigma_{mf} - \sigma_{ms})$  then admissible.

#### Path 2

- If  $\sigma \geq \sigma_{ms} + \xi_n^+(\sigma_{mf} - \sigma_{ms})$ ,  $d\sigma - C_a^+ dT > 0$  and  $\xi^+ > \xi_n^+$  then admissible.

### Path 3

- If  $\sigma \geq V_{mf}^+$  then admissible.

If multiple states are admissible we select the state which is closest to the previous converged state via the metric  $\sigma = \min_i [d(\sigma_n, \sigma_i)]$ . The resulting state is returned to the element and the residual and tangent arrays are built.

### 4.1.3 Production of Negative Single Variant Martensite

Consider now the production of negative single variant martensite with initial conditions at time  $t_n$  shown in Figure 4.5. Given a temperature increase to  $T_{n+1}$  we wish to determine the state for time  $t_{n+1}$ .

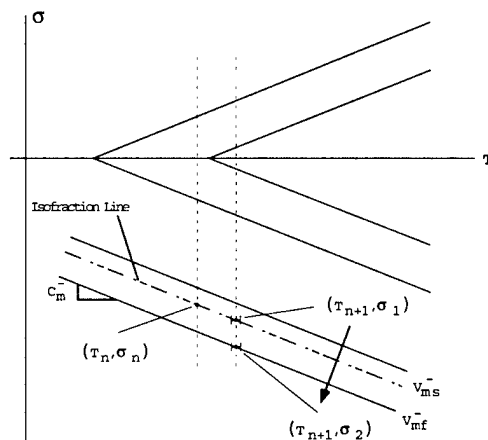


Figure 4.5: Bounds for martensite fraction in phase space. Note for the production of single variant martensite to occur the stress must be greater than  $\sigma_n$  and less than  $\sigma_2$  and the resulting state must be evolving in the direction of the arrow.

For the production of single variant negative martensite we consider the state  $(T_n, \sigma_n)$  on the phase diagram in Figure 4.5 and two critical states  $(T_{n+1}, \sigma_1)$  and  $(T_{n+1}, \sigma_2)$  at time  $t_{n+1}$ . The pair  $(T_{n+1}, \sigma_1)$  corresponds to a point on the iso-fraction line, while the pair  $(T_{n+1}, \sigma_2)$  corresponds to the point at which the martensite transformation is completed. From these

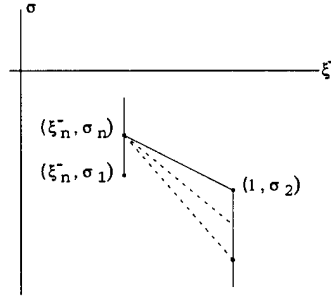


Figure 4.6: Possible trajectories in stress-fraction space. We observe from the diagram that elastic states exist for  $\sigma > \sigma_n$  or  $\sigma < \sigma_2$ . For values of stress within these elastic state exist the possibility of a phase transformation.

two points we see at time  $t_{n+1}$  there exists three possible regions for the solution, see Figure 4.6.

To determine the correct trajectory for the state at  $t_{n+1}$  we evaluate the constitution for all three regions. The three possible choices are:

1. ( $\sigma > \sigma_1$  - Elastic State) Evaluate the constitution using the previous converged value for the internal variables:

$$\sigma = E \left( \varepsilon_{n+1}^{(k+1)} - \varepsilon_n^p - \varepsilon_L [\xi_n^+ - \xi_n^-] - \alpha [T_{n+1} - T_0] \right) \quad (4.8)$$

2. ( $\sigma_1 \geq \sigma \geq \sigma_2$  - Production of Single Variant Martensite) Simultaneously solve for the constitution and the evolution:

$$\sigma = \frac{E}{b_0} \left( \varepsilon_{n+1}^{(k+1)} - \varepsilon_n^p + \varepsilon_L + (b_0 - 1) \frac{V_{mf}^-}{E} - \alpha [T_{n+1} - T_0] \right) \quad (4.9)$$

$$\xi^- = 1 + (1 - \xi_{pn}^-) \left( \frac{\sigma - V_{mf}^-}{V_{mf}^- - V_{ms}^-} \right)$$

3. ( $\sigma < \sigma_2$  - Elastic State) Evaluate the constitution assuming that the martensite transformation is completed:

$$\sigma = E \left( \varepsilon_{n+1}^{(k+1)} - \varepsilon_n^p - \varepsilon_L - \alpha [T_{n+1} - T_0] \right) \quad (4.10)$$

For the production of negative single variant martensite to occur  $\xi_n^- < 1$  and  $\sigma_n \leq 0$ . If this criteria is met then paths 1, 2 and 3 are evaluated. The additional consistency checks on the directionality and magnitudes of the stress and the internal variables for each path are outlined below.

#### Path 1

- If  $\sigma \geq -\sigma_{ms} - \xi_n^-(\sigma_{mf} - \sigma_{ms})$  then admissible.

#### Path 2

- If  $\sigma \leq -\sigma_{ms} - \xi_n^-(\sigma_{mf} - \sigma_{ms})$ ,  $d\sigma - C_a^- dT < 0$  and  $\xi^- > \xi_n^-$  then admissible.

#### Path 3

- If  $\sigma \leq V_{mf}^-$  then admissible.

If multiple states are admissible we select the state which is closest to the previous converged state via the metric  $\sigma = \min_i [d(\sigma_n, \sigma_i)]$ . The resulting state is returned to the element and the residual and tangent arrays are built.

### 4.1.4 Production of Multiple Variant Martensite

Consider now the production of multiple variant martensite with initial conditions at time  $t_n$  shown in Figure 4.7. Given a temperature increase to  $T_{n+1}$  we wish to determine the state for time  $t_{n+1}$ .

For the production of multiple variant martensite we consider the state  $(T_n, \sigma_n)$  on the phase diagram in Figure 4.7 and two critical states  $(T_{n+1}, \sigma_1)$  and  $(T_{n+1}, \sigma_2)$  at time  $t_{n+1}$ . The pairs  $(T_{n+1}, \sigma_1)$  and  $(T_{n+1}, \sigma_2)$  corresponds to limit points between which a multiple variant martensite transformation occurs. From these two points we see at time  $t_{n+1}$  there exists one possible region for the solution, see Figure 4.8, provided  $dT < 0$ .

To determine the correct trajectory for the state at  $t_{n+1}$  we evaluate the constitution and evolution for this region:

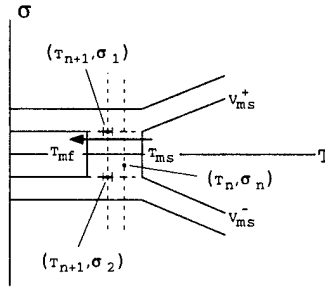


Figure 4.7: Bounds for martensite fraction in phase space. For the production of multiple variant martensite to occur  $V_{ms}^+ > \sigma > V_{ms}^-$ , and  $\dot{T} < 0$ .

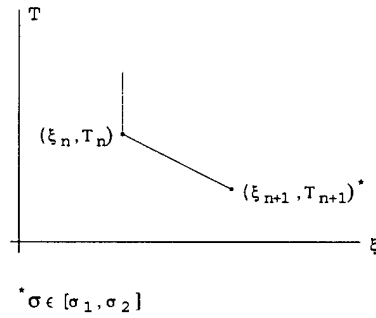


Figure 4.8: Possible trajectories in stress-fraction space. Note that during this transformation the evolution is decoupled from the constitution and hence only an evaluation is required to determine the state and internal variables.

- ( $\sigma_2 \geq \sigma \geq \sigma_1$  - Production of Multiple Variant Martensite) Simultaneously solve for the constitution and the evolution:

$$\xi = 1 + (1 - \xi_p) \left( \frac{T_{n+1} - \theta_{mf}}{\theta_{mf} - \theta_{ms}} \right) \quad (4.11)$$

$$\sigma = E \left( \varepsilon_{n+1}^{(k+1)} - \varepsilon^p - \varepsilon_L [\xi_n^+ - \xi_n^-] - \alpha [T_{n+1} - T_0] \right)$$

The resulting state is returned to the element and the residual and tangent arrays are built.

## 4.1.5 Outline of Algorithm

The previous sections outline the various constitutive and evolution equations which need to be evaluated. To minimize the computational effort, we may exclude states by simple conditional checks with the previous state. Once a reduced set of states is determined, additional checks are performed to ensure that the directionality and magnitude of the resulting state is consistent with its location on the phase diagram.

We now consider the various transformations which can occur and their associated consistency check.

### Production of Austenite

For the production of austenite to occur  $T \geq T_{as} + (1 - \xi_0)(T_{af} - T_{as})$  and  $\xi_n > \xi_{apx}$  must be met. If this criteria is met then paths 1, 2 and 3 are evaluated. The additional consistency checks on the directionality and magnitudes of the stress and the internal variables for each path are outlined below.

#### Path 1: Elastic

- If  $\sigma > 0$  and  $\sigma \geq V_{as}^+$  then admissible.
- If  $\sigma < 0$  and  $\sigma \leq V_{as}^-$  then admissible.

#### Path 2: Transformation

- If  $\sigma > 0$ ,  $\sigma \leq V_{as}^+$ ,  $-d\sigma + C_a^+ dT > 0$  and  $\xi_{apx} \leq \xi < \xi_n$  then admissible.
- If  $\sigma < 0$ ,  $V_{as}^- \leq \sigma$ ,  $d\sigma - C_a^- dT > 0$  and  $\xi_{apx} \leq \xi < \xi_n$  then admissible.

#### Path 3: Transformation with overshoot

- If  $\sigma_n > 0$  and  $\sigma \leq \max[0, V_{af}^+]$  then admissible.
- If  $\sigma_n < 0$  and  $\sigma \geq \min[0, V_{af}^-]$  then admissible.

## Production of Positive Single Variant Martensite

For the production of positive single variant martensite to occur  $\xi_n^+ < 1$  and  $\sigma_n \geq 0$  must be met. If this criteria is met then paths 1, 2 and 3 are evaluated. The additional consistency checks on the directionality and magnitudes of the stress and the internal variables for each path are outlined below.

### Path 1: Elastic

- If  $\sigma \leq V_{ms}^+$  then admissible.

### Path 2: Transformation

- If  $\sigma \geq V_{ms}^+$ ,  $d\sigma - C_a^+ dT > 0$  and  $1 \geq \xi^+ > \xi_n^+$  then admissible.

### Path 3: Transformation with overshoot

- If  $\sigma \geq V_{mf}^+$  then admissible.

## Production of Negative Single Variant Martensite

For the production of negative single variant martensite to occur  $\xi_n^- < 1$  and  $\sigma_n \leq 0$  must be met. If this criteria is met then paths 1, 2 and 3 are evaluated. The additional consistency checks on the directionality and magnitudes of the stress and the internal variables for each path are outlined below.

### Path 1: Elastic

- If  $\sigma \geq V_{ms}^-$  then admissible.

### Path 2: Transformation

- If  $\sigma \leq V_{ms}^-$ ,  $d\sigma - C_a^- dT < 0$  and  $1 \geq \xi^- > \xi_n^-$  then admissible.

### Path 3: Transformation with overshoot

- If  $\sigma \leq V_{mf}^-$  then admissible.

## Production of Multiple Variant Martensite

For the production of multiple variant martensite to occur  $\xi_n < 1$  must be met. If this criteria is met then the path 1D is evaluated. The additional consistency checks on the directionality and magnitude of the stress temperature and the internal variables for the path is outlined below.

### Path 2: Transformation

- If  $V_{ms}^- \leq \sigma \leq V_{ms}^+$ ,  $dT < 0$ , and  $1 \geq \xi > \xi_n$  then admissible.

### Multiple States

Once the respective constitution and evolution equations have been evaluated and consistency checks performed the state is returned to the main driver element for the construction of the residual and tangent arrays described in the following sections. If multiple states are admissible, we select the state which is closest to the previous converged state<sup>1</sup> and is implemented with a metric. The metric is minimized using the admissible current states and the previous converged state, i.e.  $\sigma = \min_i [d(\sigma_n, \sigma_i)]$  where  $d(x, y) = |x - y|$ . The resulting state is returned to the element and arrays built.

## 4.2 Multi-Dimensional Truss-Bar Element

In this section we consider the formulation of a multi-dimensional bar element for both linear and nonlinear kinematics, see Figure 4.9 for a representation of the geometry. In addition to the physically nonlinear mechanical response of the material, we also consider the thermomechanical effects for the material. We begin with a brief outline of the basic notation used throughout the developments and then proceed with a description of the strain measure used. A variational equation for elastostatics is reviewed and the finite element interpolations for a line element are presented. Lastly, the finite element arrays necessary for implementation are developed.

---

<sup>1</sup>By choosing the closest point, we restrict the local behavior of the local constitution from returning spurious states.

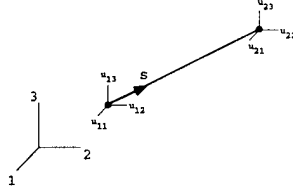


Figure 4.9: Reference configuration for the bar element.

### 4.2.1 Notation

We consider an initially straight bar of length  $L$  and cross section  $\Omega_0 \in \mathbb{R}^2$  with smooth boundary  $\partial\Omega_0$  to represent a bounded reference configuration  $\mathcal{B}$  for the continuum body. We admit the decomposition of the boundary into two parts:  $\Gamma_u \subset \partial\mathcal{B}$  where the displacement is prescribed as  $u = \bar{u}$  and  $\Gamma_t \subset \partial\mathcal{B}$  where the traction is prescribed as  $\sigma_s = \bar{\sigma}$  subject to

$$\partial\mathcal{B} = \overline{\Gamma_u \cup \Gamma_t} \quad \text{and} \quad \Gamma_u \cap \Gamma_t = \emptyset \quad (4.12)$$

where  $\sigma_s$  is the stress directed along the axis or principal direction of the bar. For subsequent treatment of the variational formulation we distinguish two classes of functions, namely, the space admissible solutions and the space of admissible variations.

Let  $\mathcal{U}$  be the space of admissible displacements written as

$$\mathcal{U} = \{u \mid u \in H^1(L) \text{ and } u = \bar{u} \text{ on } \Gamma_u\} \quad (4.13)$$

and  $\mathcal{V}$  be the space of admissible displacement variations written as

$$\mathcal{V} = \{\delta u \mid \delta u \in H^1(L) \text{ and } \delta u = 0 \text{ on } \Gamma_u\} \quad (4.14)$$

where  $H^1$  is the Sobolev space of degree 1, consisting of functions which possess square-integrable first order derivative and are themselves square-integrable.

## 4.2.2 Strain Measure

The infinitesimal increment of the strain due to a change in the length is expressed as

$$d\varepsilon_s = \frac{dl}{l} \quad (4.15)$$

where  $d\varepsilon_s$  is the increment in the strain directed along the principal axis of the bar,  $dl$  is the incremental change in length of the bar and  $l$  is the deformed length of the bar. By integrating the incremental strain from the initial length  $L$  to the deformed length  $l$  we obtain the total strain

$$\varepsilon_s = \int_L^l d\varepsilon_s = \ln\left(\frac{l}{L}\right) = \ln\left(\frac{L + \Delta L}{L}\right) = \ln(1 + \epsilon) \quad (4.16)$$

where  $\Delta L$  represents the change in length of the bar. The linear strain measure may be obtained by a series expansion of (4.16), retaining only the linear terms of the expansion. Expanding the last expression in (4.16) results in

$$\varepsilon_s = \ln(1 + \epsilon) = \epsilon - \frac{\epsilon^2}{2} + \frac{\epsilon^3}{3} - \frac{\epsilon^4}{4} + \dots = \epsilon + o(\epsilon^2) \quad (4.17)$$

subject to  $-1 < \epsilon \leq 1$ . From (4.17) the linearized strain measure becomes

$$\varepsilon_s = \frac{\Delta L}{L} = \frac{\partial u_s}{\partial s} \quad (4.18)$$

where  $u_s$  is the deformation directed along the principal axis of the member and  $s$  is a distance measure directed along the principal axis of the member.

### 4.2.3 Variational Formulation

An approximate solution of the boundary value problem is constructed from a variational statement of the problem. The basic field equations may be included in a variational statement for the elasticity problem using a potential functional. Accordingly, we have a functional in which the displacement field,  $u_s \in \mathcal{U}$  is regarded as the independent variable. The proposed functional  $\Pi : \mathcal{U} \rightarrow \mathbb{R}$  may be expressed as

$$\Pi(u_s) = \int_{\mathcal{B}} W(\varepsilon_s) dV + \Pi_{ext}(u_s) \quad (4.19)$$

where  $W(\varepsilon_s)$  is a stored energy function and for conservative external loading

$$\Pi_{ext}(u_s) = - \int_{\mathcal{B}} b_s u dV - \int_{\Gamma_t} \bar{\sigma} u dA \quad (4.20)$$

$b_s$  being the body force per unit volume.

We may state the problem as: Find  $u_s \in \mathcal{U}$  which makes the functional  $\Pi(u_s)$  stationary for all admissible variations  $\delta u_s \in \mathcal{V}$ .

The stationary point of  $\Pi$  is obtained by setting to zero the first variation of (4.19) with respect to the independent field. Accordingly,

$$\delta \Pi = \int_{\mathcal{B}} \frac{\partial W}{\partial \varepsilon_s} \delta \varepsilon_s dV - \int_{\mathcal{B}} \delta u b_s dV - \int_{\Gamma_t} \delta u \bar{\sigma} dA = 0 \quad \text{in } \mathcal{B} \quad (4.21)$$

for all admissible variations  $\delta u_s \in \mathcal{V}$ .

We may recast the first term of (4.21) as

$$\delta \Pi_{int} = \int_L \delta \varepsilon_s \frac{\partial W}{\partial \varepsilon_s} \Omega_0 ds \int_L \delta \varepsilon_s \sigma_s \Omega_0 ds = \delta \varepsilon_s \sigma_s \Omega_0 L \quad (4.22)$$

which represents the internal virtual work.

## 4.2.4 Finite Element Interpolations

To enable numerical implementation of the variational formulation a discretization with respect to the global variables is performed. We begin by discretizing the bar into a finite number of points called nodes. Connecting two nodes constitutes an element on which the formulation is developed. In the following the interpolations for the global variables are introduced.

The selection of the displacement interpolation functions for the element must satisfy certain basic requirements such that the solution converges to the exact solution under certain special cases.

The displacement interpolation functions must

1. be continuous within the element,
2. be able to capture rigid body modes,
3. be able to capture constant strain states,
4. ensure inter-element compatibility.

The bar element used for the subsequent developments consists of an initially straight bar with two nodal points located on the boundary of the line segment. The obvious selection for the interpolation functions which satisfy the above criteria are

$$N_1 = 1 - \frac{s}{L} \quad \text{and} \quad N_2 = \frac{s}{L} . \quad (4.23)$$

Utilizing the interpolation functions in (4.23) we may express the displacement vector  $\mathbf{u}$ , as well as the position vector  $\mathbf{X}$  for the bar as

$$u_i(s) = \sum_{I=1}^2 N_I \hat{u}_{Ii} \quad \text{and} \quad X_i(s) = \sum_{I=1}^2 N_I \hat{X}_{Ii} \quad (4.24)$$

where  $i = 1, \dots, ndm$  is the dimension of the space and  $\hat{u}$  and  $\hat{X}$  are the nodal quantities of the displacement and coordinates, respectively. For further elaboration on the development of finite element interpolation see HUGHES [1987] OR ZIENKIEWICZ & TAYLOR [1989].

## 4.2.5 Linear Kinematic Element

We proceed by defining the strain measure used for the formulation, develop the expression for the internal virtual work from which the residual equations may be expressed. Lastly, the resulting nonlinear residual equation is linearized to afford a solution of the nonlinear set of equations via Newton's method.

### Strain Measure

Recall from the previous section the expression for the linearized strain measure is

$$\varepsilon_s = \frac{\partial u_s}{\partial s} = \sum_{i=1}^{ndm} l_i \frac{\partial u_i}{\partial s} \quad (4.25)$$

where  $u_i$  is the displacement in the coordinate direction  $i$  and  $l_i$  is the direction cosine in the  $i^{th}$  coordinate direction defined in terms of the nodal locations as

$$l_i = \frac{X_{2i} - X_{1i}}{L} = \frac{\Delta X_i}{L} \quad \text{and} \quad L^2 = \sum_{i=1}^{ndm} (X_{2i} - X_{1i})^2 . \quad (4.26)$$

Utilizing (4.26) we may express the strain in the principal direction as

$$\varepsilon_s = \frac{\Delta X_i}{L} \frac{\Delta u_i}{L} \quad (4.27)$$

where summation over  $i$  is implied and  $\Delta u_i = u_{2i} - u_{1i}$  represents the relative displacement in the  $i^{th}$  coordinate direction.

## Residual and Tangent Arrays

Substitution of (4.27) into the expression for the internal virtual work yields

$$\delta\Pi_{int} = \frac{\Delta X_i}{L} \frac{\delta\Delta u_i}{L} \sigma_s \Omega_0 L = \delta\Delta u_i \sigma_s l_i \Omega_0 \quad (4.28)$$

or in matrix notation we have

$$\delta\Pi_{int} = \left\{ \delta u_{1i} \quad \delta u_{2i} \right\} \begin{Bmatrix} -F_i \\ F_i \end{Bmatrix} \quad (4.29)$$

where  $F_i = \sigma_s l_i \Omega_0$  is the internal force.

To introduce one-way thermal effects<sup>2</sup> into the formulation we introduce an additional nodal quantity or degree of freedom, namely temperature into (4.29)

$$\delta\Pi_{int} = \left\{ \delta u_{1i} \quad \delta T_{1i} \quad \delta u_{2i} \quad \delta T_{2i} \right\} \begin{Bmatrix} -F_i \\ 0 \\ -F_i \\ 0 \end{Bmatrix} . \quad (4.30)$$

The vector post-multiplying the virtual displacements and temperatures in (4.30) is commonly referred to as the internal load vector and is denoted as  $F_{int}$  for future developments.

### Remark 4.2.

Recall from Chapter 3 that the stress  $\sigma_s$  is in general a function of the mechanical and thermal state and internal variables, i.e.  $\sigma_s = \widehat{\sigma}(\varepsilon, T, \xi)$ . Hence, its variation with respect to the added degree of freedom is nonzero in general and must be considered when constructing the solution.

---

<sup>2</sup>The one-way coupling used throughout refers to the ability of a thermal gradient to produce mechanical strains, but the reverse process is uncoupled and hence not considered.

To facilitate a solution of the mixed boundary value problem the nonlinear equation (4.21) is linearized and solved by a Newton's method as a sequence of linearized problems. Hence, linearizing (4.21), neglecting external work terms we obtain

$$d(\delta\Pi) = \delta\varepsilon_s d\sigma_s \Omega_0 L \quad (4.31)$$

where

$$d\sigma_s = D_M d\varepsilon_s + D_T dT \quad (4.32)$$

and  $D_M$  and  $D_T$  are the mechanical and thermal material moduli. Substituting (4.32) into (4.31) with the aid of (4.27) yields

$$d(\delta\Pi) = \sum_{i=1}^{ndm} \sum_{j=1}^{ndm} \frac{\delta\Delta u_i l_i}{L} \left[ D_M \frac{d\Delta u_j l_j}{L} + D_T \frac{dT_j}{2} \right] \Omega_0 L \quad (4.33)$$

and expressed in matrix notation we have

$$d(\delta\Pi) = \begin{Bmatrix} \delta u_{1i} \\ \delta T_{1i} \\ \delta u_{2i} \\ \delta T_{2i} \end{Bmatrix}^T \begin{bmatrix} k_{ij} & -h_i & -k_{ij} & -h_i \\ 0 & 0 & 0 & 0 \\ -k_{ij} & h_i & k_{ij} & h_i \\ 0 & 0 & 0 & 0 \end{bmatrix} \begin{Bmatrix} du_{1j} \\ dT_{1j} \\ du_{2j} \\ dT_{2j} \end{Bmatrix} = \delta\eta^T \mathbf{k} d\eta \quad (4.34)$$

where

$$k_{ij} = D_M l_i l_j \frac{\Omega_0}{L} \quad \text{and} \quad h_i = D_T l_i \frac{\Omega_0}{2} . \quad (4.35)$$

The matrix post-multiplying the virtual displacements and temperatures in (4.34) is commonly referred to as the tangent matrix and is denoted as  $\mathbf{k}$ . The terms  $D_M$  and  $D_T$  are

the tangent moduli from the previous sections depending on the state of the material. Note that the continuum and algorithmic tangents are the same since the evolution of the internal variables is treated exactly.

## 4.2.6 Non-Linear Kinematic Element

We proceed by defining the strain measure used for the formulation and then develop the expression for the internal virtual work from which the residual equations may be expressed. Lastly, the resulting nonlinear residual equation is linearized to allow solution of the nonlinear set of equations via Newton's method.

### Strain Measure

Recall from the previous sections that the expression for the nonlinear strain measure is

$$\varepsilon_s = \int_L^l d\varepsilon_s = \ln \left( \frac{l}{L} \right) . \quad (4.36)$$

### Variational Formulation

The functional for the current formulation is altered such that the bounds of the integration are performed on the current volume. The resulting expression for the internal virtual work now becomes

$$\delta\Pi_{int} = \delta\varepsilon_s \sigma_s \Omega l = \delta l \sigma_s \Omega \quad (4.37)$$

where the constraint  $\Omega l = \Omega_0 L$  is assumed for the case of material inelasticity<sup>3</sup>.

<sup>3</sup>Recall from Chapter 2 the volumetric change during a transformation is negligible.

## Residual and Tangent Arrays

The interpolation functions are taken to be the same as the linear model, resulting in the following expression for the variation of the bar length

$$\delta l = \sum_{i=1}^{ndm} \frac{\Delta x_i}{l} \delta \Delta u_i \quad (4.38)$$

where the square deformed length is expressed as

$$l^2 = \sum_{i=1}^{ndm} (\Delta X_i + \Delta u_i)^2 = \sum_{i=1}^{ndm} (\Delta x_i)^2 \quad (4.39)$$

where  $\Delta X_i = X_{2i} - X_{1i}$  and  $\Delta u_i = u_{2i} - u_{1i}$ .

Substitution of (4.38) into the expression for the internal virtual work (4.37) yields

$$\delta \Pi = \delta \Delta u_i \sum_{i=1}^{ndm} \frac{\Delta x_i}{l} \sigma \Omega \quad (4.40)$$

and expressed in matrix notation we have

$$\delta \Pi = \{ \delta u_{1i} \quad \delta u_{2i} \} \left\{ \begin{array}{c} -F_i \\ F_i \end{array} \right\} \quad (4.41)$$

where  $F_i = (\sigma \Omega) \frac{\Delta x_i}{l}$  is the internal force.

As in the previous section we introduce one-way thermal effects into the formulation by adding an additional nodal quantity or degree of freedom, namely temperature into (4.41)

$$\delta\Pi_{int} = \left\{ \delta u_{1i} \quad \delta T_{1i} \quad \delta u_{2i} \quad \delta T_{2i} \right\} \begin{Bmatrix} -F_i \\ 0 \\ -F_i \\ 0 \end{Bmatrix}. \quad (4.42)$$

The vector post-multiplying the virtual displacements and temperatures in (4.42) is commonly referred to as the internal load vector and is denoted as  $\mathbf{F}_{int}$  for future developments.

To facilitate a solution of the mixed boundary value problem the nonlinear equation (4.37) is linearized and solved by Newton's method as a sequence of linearized problems. Hence, linearizing (4.37) we obtain

$$d(\delta\Pi) = d(\delta l) \sigma_s \Omega + \delta l d\sigma_s \Omega + \delta l \sigma_s d\Omega \quad (4.43)$$

where

$$\begin{aligned} d(\delta l) &= \frac{1}{l} \sum_{i=1}^{ndm} \sum_{j=1}^{ndm} \delta\Delta u_i d\Delta u_j - \frac{1}{l} \sum_{i=1}^{ndm} \frac{\Delta x_i}{l} \delta\Delta u_i \sum_{j=1}^{ndm} \frac{\Delta x_j}{l} d\Delta u_j \\ d\Omega &= -\Omega \frac{dl}{l} = -\Omega \sum_{j=1}^{ndm} \frac{\Delta x_j}{l^2} d\Delta u_j \\ d\sigma_s &= D_M d\varepsilon_s + D_T dT \end{aligned} \quad (4.44)$$

and  $D_M$  and  $D_T$  are the mechanical and thermal material moduli and are unchanged from the linear case. Substituting (4.44) into (4.43) with the aid of (4.38) yields

$$d(\delta\Pi) = \sum_{i=1}^{ndm} \sum_{j=1}^{ndm} \delta\Delta u_i \left\{ d\Delta u_j \left( \frac{\sigma_s}{l} + \frac{\Delta x_i}{l} \frac{\Delta x_j}{l} \frac{(D_M - 2\sigma_s)}{l} \right) + \frac{\Delta x_i}{2l} D_T dT_j \right\} \Omega \quad (4.45)$$

and expressed in matrix notation we have

$$d(\delta\Pi) = \begin{Bmatrix} \delta u_{1i} \\ \delta T_{1i} \\ \delta u_{2i} \\ \delta T_{2i} \end{Bmatrix}^T \begin{bmatrix} k_{ij} & -h_i & -k_{ij} & -h_i \\ 0 & 0 & 0 & 0 \\ -k_{ij} & h_i & k_{ij} & h_i \\ 0 & 0 & 0 & 0 \end{bmatrix} \begin{Bmatrix} du_{1j} \\ dT_{1j} \\ du_{2j} \\ dT_{2j} \end{Bmatrix} = \delta\eta^T \mathbf{k} d\eta \quad (4.46)$$

where

$$k_{ij} = \left( \frac{\sigma_s}{l} + \frac{\Delta x_i}{l} \frac{\Delta x_j}{l} \frac{(D_M - 2\sigma_s)}{l} \right) \Omega \quad \text{and} \quad h_i = \frac{\Delta x_i}{l} D_T \frac{\Omega}{2}. \quad (4.47)$$

The matrix post-multiplying the virtual displacements and temperatures in (4.46) is commonly referred to as the tangent matrix and is denoted as  $\mathbf{k}$ . As presented it includes both the “material” tangent and the “geometric” tangent.

## 4.2.7 Solution Procedure

Noting that the variations  $\delta\eta$  in the previous sections are arbitrary we obtain the finite element residual equations

$$\mathbf{F}_{int}(\boldsymbol{\eta}) - \mathbf{F}_{ext}(\boldsymbol{\eta}) = \mathbf{A}_{e=1}^{nelm} [\mathbf{F}_{int}^e(\boldsymbol{\eta}_e) - \mathbf{F}_{ext}^e(\boldsymbol{\eta}_e)] = \mathbf{0} \quad (4.48)$$

where  $\mathbf{F}_{int}$  and  $\mathbf{F}_{ext}$  are the internal and external load vectors, respectively,  $e$  is an element within the discretization,  $nelm$  denotes the total number of elements within the discretization,  $\boldsymbol{\eta}_e = \{u_{Ii} \ T_{Ii}\}$  is the solution vector and  $\mathbf{A}$  is the standard finite element assembly operator.

Linearizing (4.48) about an intermediate state  $(\boldsymbol{\eta}_e^{(k)})$  yields

$$L[\mathbf{F}_{int}] = \mathbf{F}_{int}^{(k)} + \mathbf{k}^{(k)} d\boldsymbol{\eta}_e \quad (4.49)$$

The resulting system of equations involves the nodal solution vector at the global level expressed as

$$\mathbf{K}^{(k)} d\boldsymbol{\eta} = \mathbf{R}^{(k)} \quad (4.50)$$

where

$$\begin{aligned} \mathbf{K}^{(k)} &= \mathbf{A}_{e=1}^{nelm} [\mathbf{k}]_e^{(k)} \\ \mathbf{R}^{(k)} &= \mathbf{A}_{e=1}^{nelm} [\mathbf{F}^{ext} - \mathbf{F}^{int}]_e^{(k)}. \end{aligned} \quad (4.51)$$

The system (4.50) is solved and then the unknown fields are updated additively by

$$\boldsymbol{\eta}_e^{(k+1)} = \boldsymbol{\eta}_e^{(k)} + d\boldsymbol{\eta}_e \quad (4.52)$$

The process is repeated within a particular time step  $t_n$  until convergence of the  $(k + 1)^{th}$  iterate is obtained, the solution is then advanced to the next time step  $t_{n+1}$ . An overview of the algorithmic implementation is outlined in Table 4.1 below

### 4.2.8 Numerical Simulations

We consider several simulations encompassing both isothermal and isostress loading histories to demonstrate the features of the model. The material under consideration is NiTi and its associated material parameters can be found in Table 4.2.

#### **Isothermal NiTi Bar Under Cyclic Loading, $T < T_{mf}$**

We consider a three element discretization of a NiTi bar of length  $L = 1$  and initial area  $\Omega_0 = 1$ . The bar is fixed against translation on the initial end ( $X = 0$ ) and loaded at the

Table 4.1: Solution outline for the truss-bar element

---

```

Initialize Variables
Loop over time,  $t$ 
  Loop until convergence
    Initialize Variables
    Loop over elements
      Compute  $l_i$  and  $\Delta x_i$ 
      Compute axial strain  $\varepsilon_s$ 
      Compute stress and moduli  $\sigma_s$ ,  $D_M$  and  $D_T$ 
      Compute  $\mathbf{F}_{int}^e$  and  $\mathbf{k}^e$ 
      Assemble  $\mathbf{R}^{(k)}$  and  $\mathbf{K}^{(k)}$ 
    End loop
    Solve  $\mathbf{K}^{(k)} d\mathbf{u} = \mathbf{R}^{(k)}$ 
  End loop
End loop

```

---

Table 4.2: Material Properties for NiTi.(BRINSON & LAMMERING [1993])

---

```

Young's Moduli  $E_m = E_a = 67$  GPa
Critical stresses for de-twinning  $\sigma_{cr}^s = 100$  MPa and  $\sigma_{cr}^f = 170$  MPa
Martensite production temperatures  $T_{ms} = 18.4$  C and  $T_{mf} = 9$  C
Austenite production temperatures  $T_{as} = 34.5$  C and  $T_{af} = 49$  C
Austenite production slope  $C_a = 13.8$  MPa/C
Martensite production slope  $C_m = 8$  MPa/C
Maximum transformation strain  $\varepsilon_L = 0.067$ 
Thermal expansion coefficient  $\alpha = 6.5$   $\mu$ strain/C

```

---

terminal end ( $X = L$ ). The temperature of the bar is held constant at  $T = 5$  C, which is below the martensite finish temperature. The initial state is assumed to be 100% multiple variant martensite (i.e.  $\xi_0^+ = \xi_0^- = 0.5$ ) and the loading and response curves are outlined in the figures below.

From Figures 4.10 and 4.11 we can conclude that:

1. The algorithm accurately determines the onset and completion of negative and positive martensitic phase transformations.
2. The evolution of the positive and negative variants is continuous and smooth during

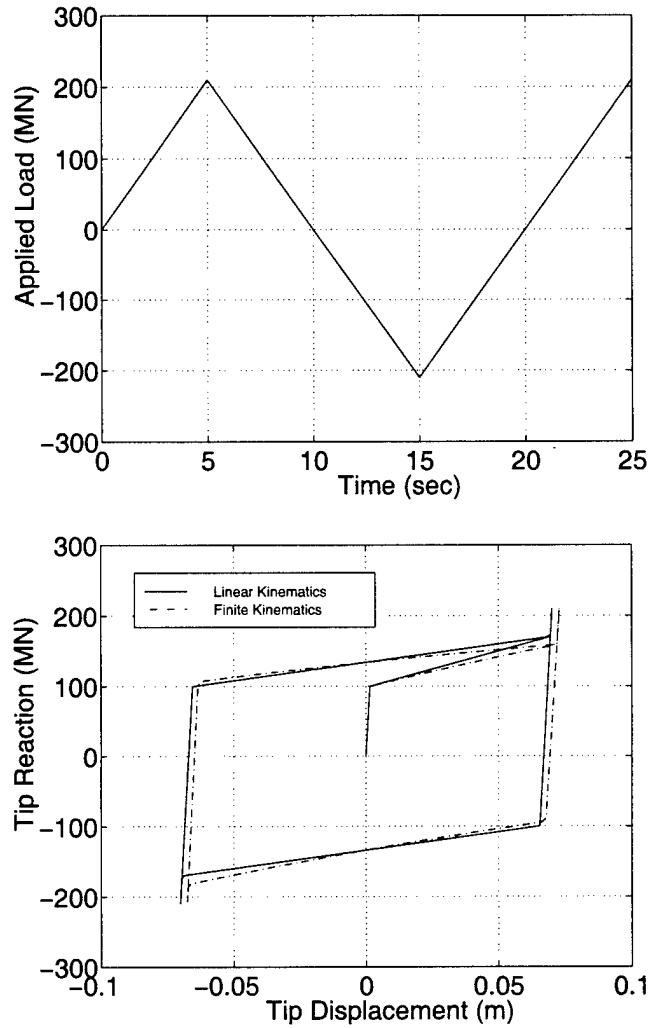


Figure 4.10: Loading and response curves for an isothermal NiTi bar under cyclic loading,  $T < T_{mf}$ .

the transformations. Note, the production of one variant at the expense of the other, while their sum remains unity, i.e 100% martensite.

3. Both the linear and non-linear models given similar results, since the strain level is moderate.

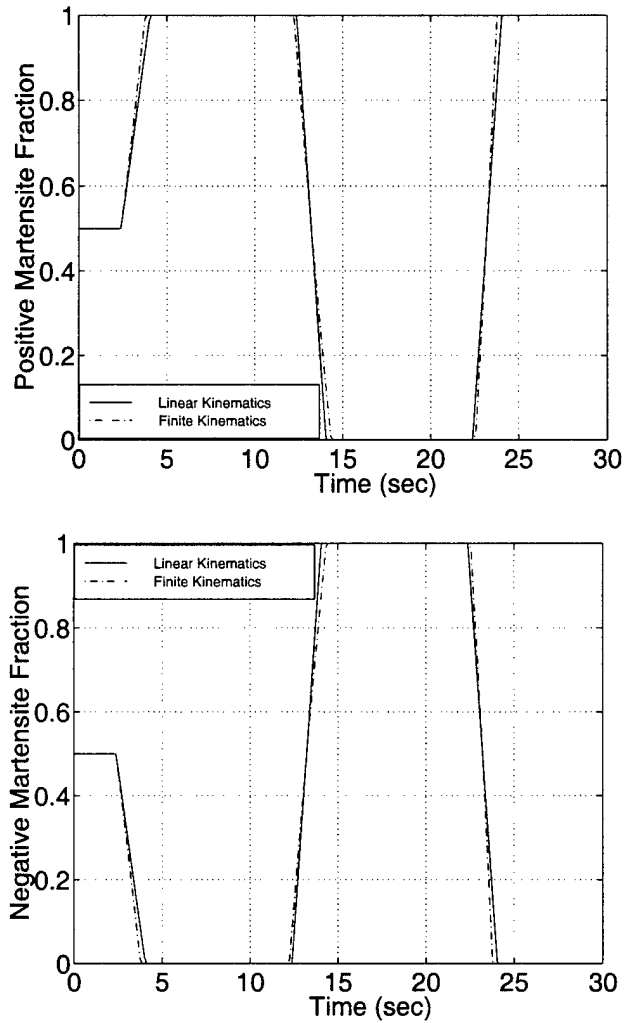


Figure 4.11: Time history of the internal variables for an isothermal NiTi bar under cyclic loading,  $T < T_{mf}$ .

4. For the completion of the positive variant martensite the algorithm has a possibility of three choices: a) elastic unloading with  $\xi^+ = \xi_n^+$ , b) elastic loading  $\xi^+ = 1$  and c) positive single variant martensitic phase transformation. Upon computing the three states the algorithm determines a) is inadmissible since  $d\sigma > 0$  and  $\dot{\xi}^+ = 0$ . The remaining paths are admissible with b) selected based on the distance measure of the

computed and previous values of stress. The algorithm continues to choose b) until the current time step converges. Advancing to the next time step the external loading continues to increase and the algorithm determines that b) is the only admissible path. A similar process continues throughout the remainder of the loading history.

### Isothermal NiTi Bar Under Cyclic Loading, $T_{as} < T < T_{af}$

We consider a three element discretization of a NiTi bar of length  $L = 1$  and initial area  $\Omega_0 = 1$ . The bar is fixed against translation on the initial end ( $X = 0$ ) and loaded at the terminal end ( $X = L$ ). The temperature of the bar is held constant at  $T = 41.75$  C, which is above the austenite start temperature and below the austenite finish temperature. The initial state is assumed to be 50% multiple variant martensite (i.e.  $\xi_0^+ = \xi_0^- = 0.25$ ) and the loading and response curves are outlined in the figures below.

From Figures 4.12 and 4.13 we can conclude that:

1. The algorithm accurately determines the onset and completion of negative and positive martensitic phase transformations.
2. The model predicts the termination of a austenite transformation when crossing over the stress axis.
3. The evolution of the positive and negative variants is continuous and smooth during the transformations. Note, the production of one variant at the expense of the other.
4. Both the linear and non-linear models given similar results, since the strain level is moderate.
5. For the termination of the austenite production from a positive stress state the algorithm has a possibility of three choices: a) elastic loading with  $\xi = \xi_n$ , b) elastic unloading  $\xi = \xi_{apx}$  and c) an austenitic phase transformation. Upon computing the three states the algorithm determines a) is inadmissible since  $d\sigma < 0$  and  $\xi = 0$ . The remaining paths are admissible with c) selected based on the distance measure of the computed and previous values of stress. The algorithm continues to choose c) until the current time step converges. Advancing to the next time step the external loading continues to decrease and the only admissible path determined from the algorithm is b).

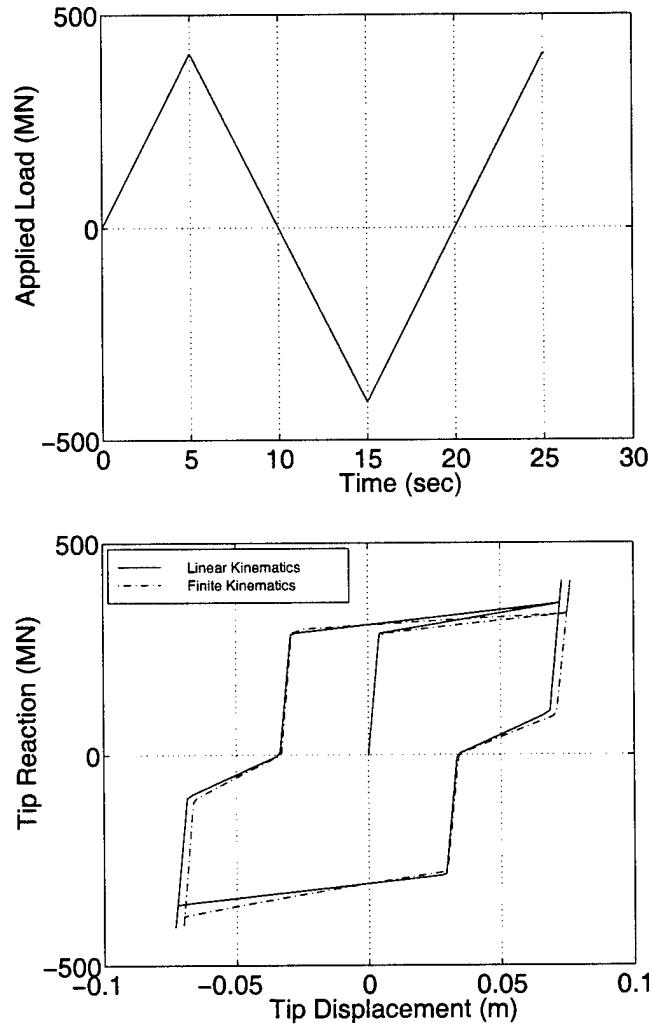


Figure 4.12: Loading and response curves for an isothermal NiTi bar under cyclic loading,  $T_{as} < T < T_{af}$ .

### Isothermal NiTi Bar Under Cyclic Loading, $T > T_{af}$

We consider a three element discretization of a NiTi bar of length  $L = 1$  and initial area  $\Omega_0 = 1$ . The bar is fixed against translation on the initial end ( $X = 0$ ) and loaded at the terminal end ( $X = L$ ). The temperature of the bar is held constant at  $T = 55$  C, which is

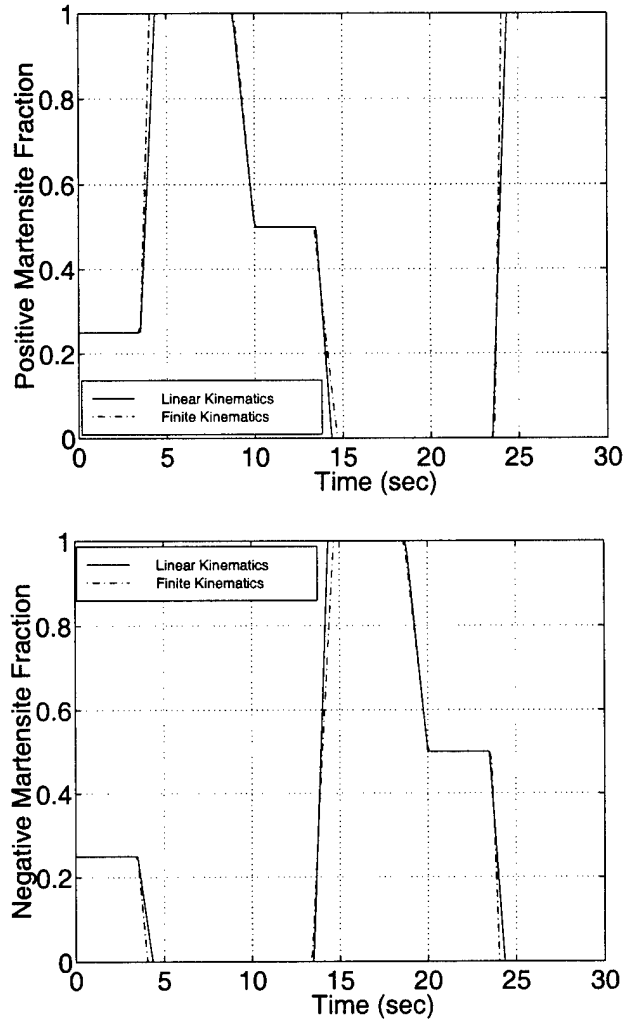


Figure 4.13: Time history of the internal variables for an isothermal NiTi bar under cyclic loading,  $T_{as} < T < T_{af}$ .

above the austenite finish temperature. The initial state is assumed to be 100% austenite (i.e.  $\xi_0^+ = \xi_0^- = 0$ ) and the loading and response curve are outlined in the figures below.

From Figures 4.14 and 4.15 we can conclude that:

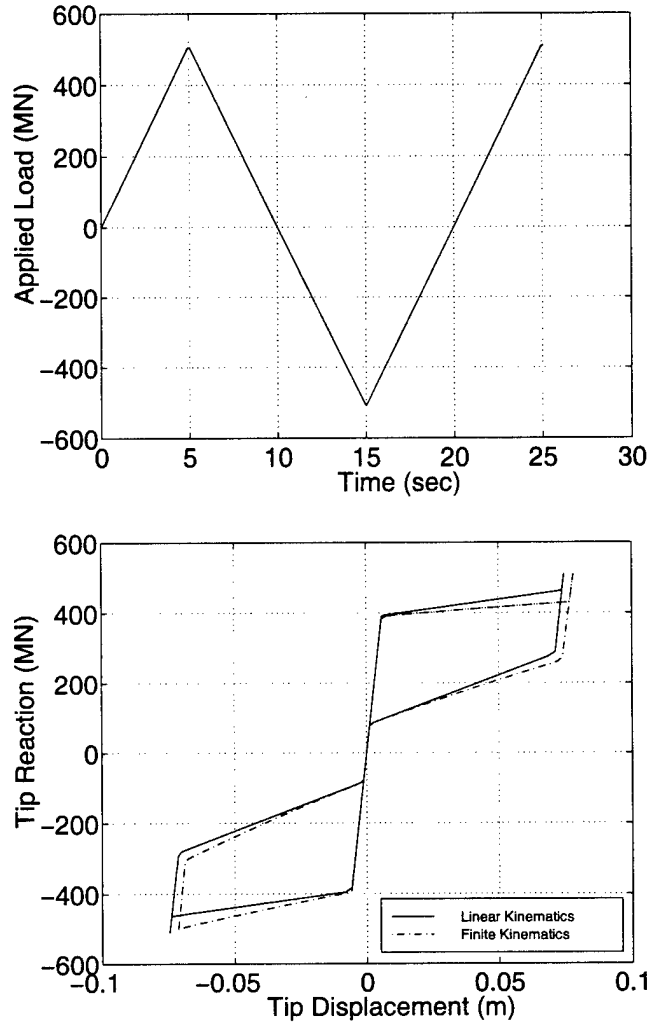


Figure 4.14: Loading and response curves for an isothermal NiTi bar under cyclic loading,  $T > T_{af}$ .

1. The algorithm accurately models the pseudoelastic behavior by determining the onset and completion of negative and positive martensitic phase transformations.
2. The evolution of the positive and negative variants is continuous and smooth during the transformations. Note, only one variant is evolved while the other remains zero, since only one variant can exist at temperatures greater than  $T_{af}$ .

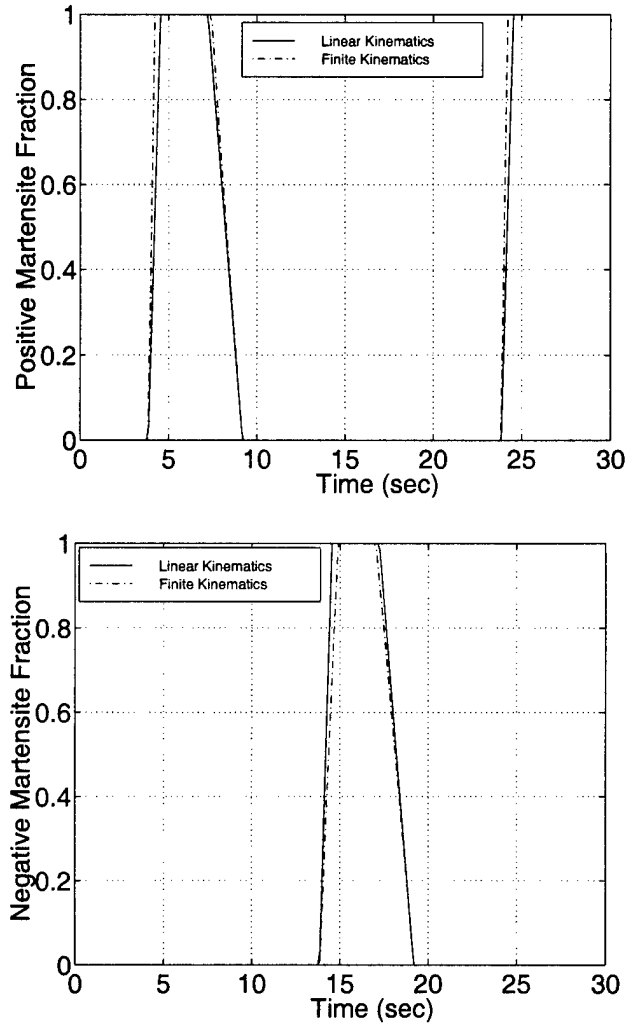


Figure 4.15: Time history of the internal variables for an isothermal NiTi bar under cyclic loading,  $T > T_{af}$ .

3. Both the linear and non-linear models given similar results, since the strain level is moderate.
4. For both the single variant martensite and austenite productions the algorithmic behavior is similar to the simulations in the previous sections.

5. The termination of the single variant martensite and austenite production follow from the previous cases.

### NiTi Bar Under Thermo-mechanical Cyclic Loading

We consider a three element discretization of a NiTi bar of length  $L = 1$  and initial area  $\Omega_0 = 1$ . The bar is fixed against translation on the initial end ( $X = 0$ ) and loaded at the terminal end ( $X = L$ ). The temperature of the bar is initially held at 65 C; cooled to 5 C under zero load; then loaded and unloaded isothermally at 5 C, and lastly heated to 65 C under zero load. The initial state is assumed to be 100% austenite (i.e.  $\xi_0^+ = \xi_0^- = 0$ ) and the loading and response curves are outlined in the figures below.

From Figures 4.16-4.18 we can conclude that:

1. The algorithm accurately models the shape memory effect by determining the onset and completion of various phase transformations.
2. During the initial cooling process, note the strain developed is negligible (thermal expansion effects) due to the self-accommodating state which arises during the production of multiple variant martensite.
3. During the loading process the evolution of the positive variant continues to grow at the expense of the negative variant until the transformation is completed.
4. Upon heating the bar we see that the residual strain goes to zero as experimental observation shows.
5. Both the linear and non-linear models given similar results, since the strain level is moderate.
6. The algorithmic treatment for the termination of the single variant martensite follows from previous sections. Whereas, for the austenite transformation the algorithm picks three paths: a) elastic loading with  $\xi = \xi_n$ , b) an austenitic phase transformation assuming a positive value for the stress and c) an austenitic phase transformation assuming a negative value for the stress. Upon computing the three states the algorithm determines a) is inadmissible since  $dT > 0$  and  $\dot{\xi} = 0$ . The remaining paths are admissible with c) selected based on the distance measure of the computed and previous values of stress. The algorithm continues to choose c) until the current time step

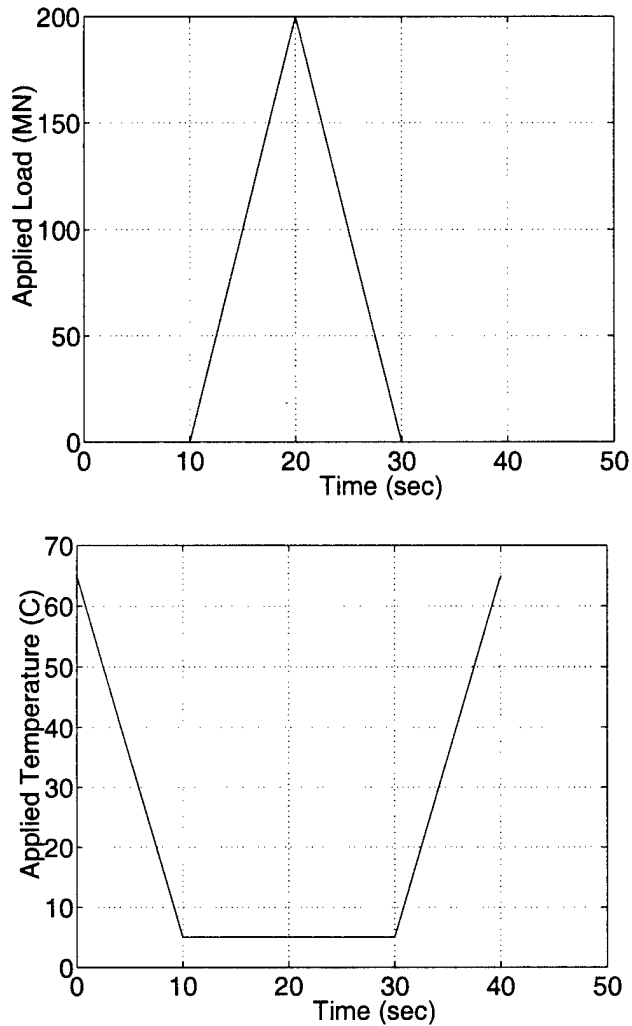


Figure 4.16: Loading and response curves for an NiTi bar under thermo-mechanical cyclic loading

converges. The transformation advances until the martensite is fully depleted. After the martensite fraction is depleted the algorithm only chooses an elastic state.

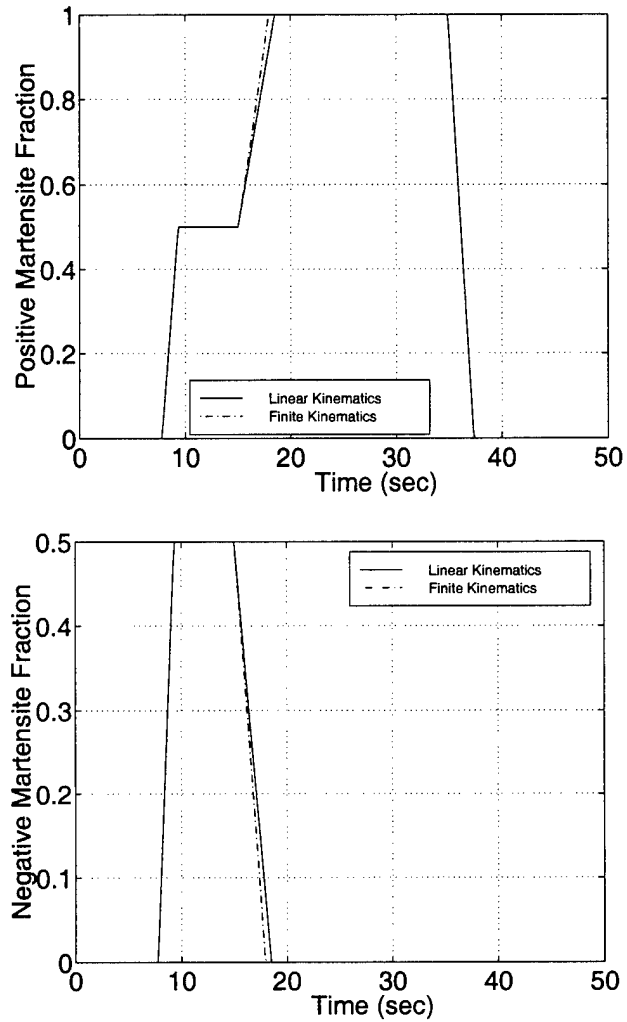


Figure 4.17: Time history of the internal variables for an NiTi bar under thermo-mechanical cyclic loading.

### NiTi Truss-Bridge Under Cyclic Loading

We consider a NiTi cantilever truss-bridge consisting of 53 elements shown in Figure 4.19. The bridge is 20 units long by 2 units deep and all elements have an initial area  $\Omega_0 = 1$ .

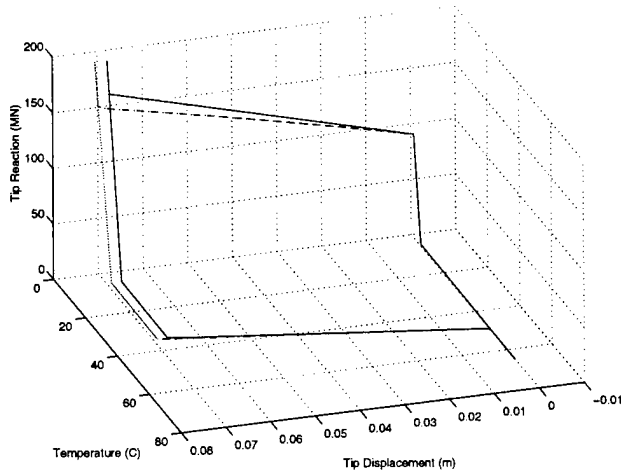


Figure 4.18: Thermo-mechanical response for an NiTi bar under thermo-mechanical cyclic loading.

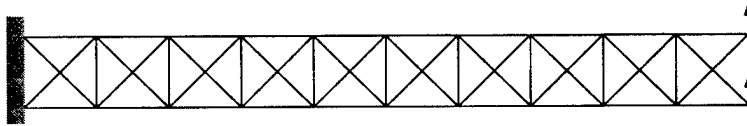


Figure 4.19: Reference configuration for the truss-bridge.

Four simulations are performed to demonstrate the ability of the algorithm to predict the behavior of a system with spatial inhomogeneities for various loading conditions

**Simulation #1**

The truss-bridge is isothermally loaded to a peak load of 156 MN and then unloaded at temperature of 5 C. The initial state of the material is 100% multiple variant martensite (i.e.  $\xi_0^+ = \xi_0^- = 0.5$ ). The response curve is outlined in the figure below.

**Simulation #2**

The truss-bridge is isothermally loaded to a peak load of 25 MN and then unloaded at temperature of 41.75 C. The initial state of the material is 50% multiple variant martensite (i.e.  $\xi_0^+ = \xi_0^- = 0.25$ ). The response curve is outlined in the figure below.

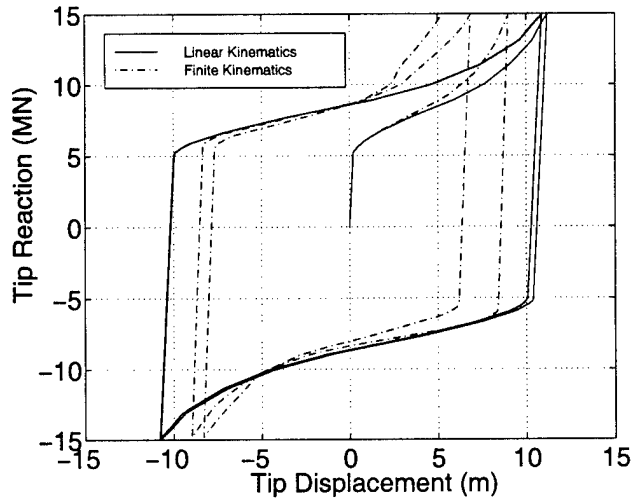


Figure 4.20: Response curve for isothermal conditions at 5 C for a NiTi truss bridge.

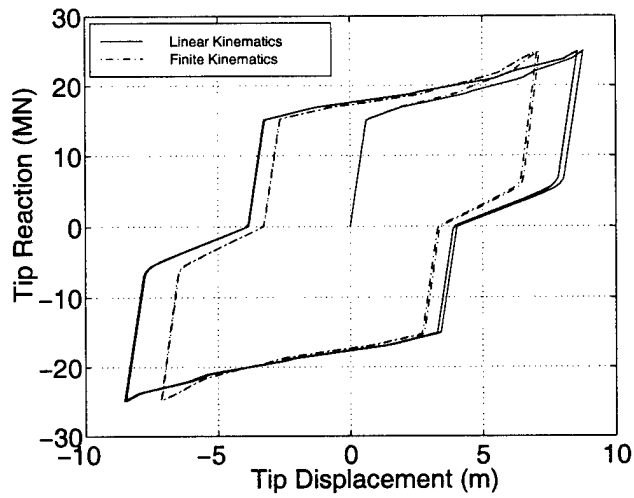


Figure 4.21: Response curve for isothermal conditions at 41.75 C for a NiTi truss bridge.

**Simulation #3**

The truss-bridge is isothermally loaded to a peak load of 35 MN and then unloaded at

temperature of 55 C. The initial state of the material is 100% austenite (i.e.  $\xi_0^+ = \xi_0^- = 0$ ). The response curve is outlined in the figure below.

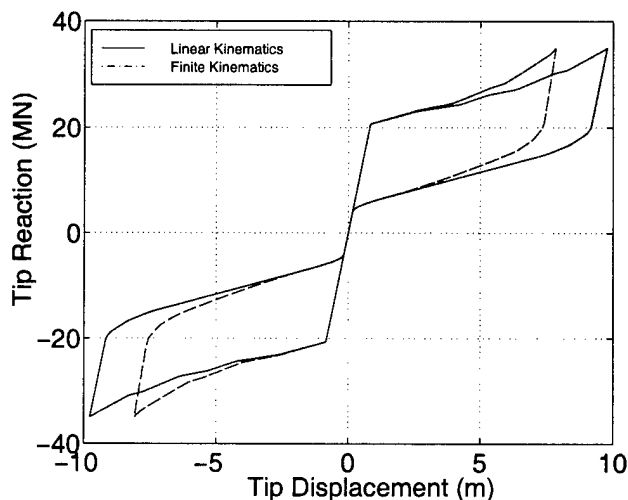


Figure 4.22: Response curve for isothermal conditions at 55 C for a NiTi truss bridge.

#### ***Simulation #4***

The truss-bridge is isothermally loaded to a peak load of 15 MN and then unloaded at temperature of 5 C. The initial state of the material is 100% multiple variant martensite (i.e.  $\xi_0^+ = \xi_0^- = 0.5$ ). The truss-beam is then heated to 65 C to facilitate the recovery of the residual strain incurred during the mechanical loading stage. The response curve is outlined in the figure below.

From Figures 4.20-4.23 we can conclude that:

1. The algorithm accurately models the global effects demonstrated in the previous uni-axial cases.
2. For temperatures below  $T_{af}$  we see that there exists a global evolution in the response. This evolution is manifested as a result of the fractions changing to different degrees from the initial conditions for the various bars. These oscillations reach a limit cycle in a few load cycles and repeatability of the response is then seen.

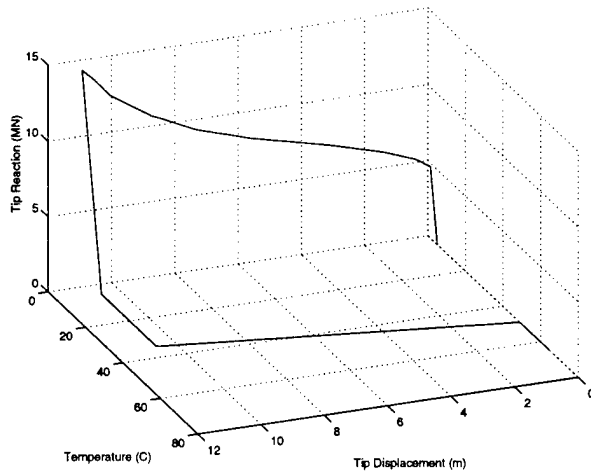


Figure 4.23: Thermo-mechanical response curve for a NiTi truss bridge.

3. For Figure 4.23 the simulation was performed using the linear element only since some bars have material moduli which are negative (due to the softening effect of the transformation) resulting in an ill posed problem for the log-stretch model. An alternative formulation using the second Piola-Kirchhoff stress and the Green-Lagrange strain tensor would circumvent this problem.
4. The difference between the linear and non-linear models is more pronounced since the strains are larger than previous cases especially for elements near the support.

## Summary of Numerical Simulations

We have considered several simulations encompassing both isothermal, isostress and non-isostress paths to demonstrate the features of the model for NiTi. Several noteworthy characteristics are:

1. The algorithm accurately activates the correct evolution equation for the corresponding state on the phase diagram.
2. The algorithm accurately models both the pseudoelastic and shape memory effect.

3. The algorithm accurately determines the onset and completion of the various phase transformations.
4. The inclusion of a simple plastic model poses no difficulty and accurately represents the behavior of the material, see VANDERMEER ET.AL. [1981] and GOVINDJEE & KASPER [1997].

### 4.3 Two-Dimensional Beam Element

In this section we consider the formulation of a two-dimensional beam element, following SIMO ET. AL. [1984] for both linear and nonlinear kinematics; see Figure 4.24 for a representation of the geometry. In the following developments we regard the thermal field as prescribed such that no additional degrees of freedom are necessary. We begin with a brief outline of the basic notation used throughout and then proceed with a description of the strain measure used. A variational equation for elastostatics and the finite element interpolations for a line element are reviewed. Lastly, the finite element arrays necessary for implementation are developed.

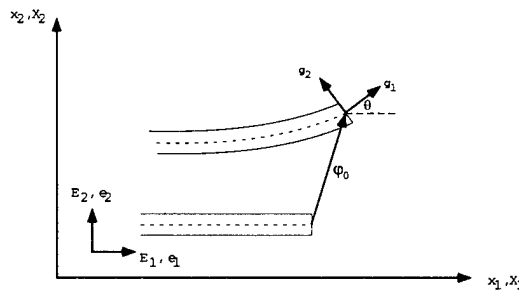


Figure 4.24: Reference and deformed configurations for the beam element.

#### 4.3.1 Notation

We consider an initially straight beam of length  $L$  and cross section  $\Omega_0 \in \mathbb{R}^2$  with smooth boundary  $\partial\Omega_0$  to represent a bounded reference configuration  $\mathcal{B}$  for the continuum body. We admit the decomposition of the boundary into two parts:  $\Gamma_w \subset \partial\mathcal{B}$  where the generalized

displacements are prescribed as  $w = \bar{w}$  and  $\Gamma_R \subset \partial\mathcal{B}$  where the generalized forces are prescribed as  $\mathbf{R} = \bar{\mathbf{R}}$  subject to

$$\partial\mathcal{B} = \overline{\Gamma_w \cup \Gamma_R} \quad \text{and} \quad \Gamma_w \cap \Gamma_R = \emptyset \quad (4.53)$$

where  $w = [u, v, \theta]^T$  denotes the generalized displacements, two translations and a rotations, and  $\mathbf{R} = [N, V, M]^T$  denotes the generalized forces of the beam, a normal and shear force and a moment.

For subsequent treatment of the variational formulation we distinguish two classes of functions as before, namely, the space of admissible solutions and the space of variations.

Let  $\mathcal{U}$  be the space of admissible generalized displacements written as

$$\mathcal{U} = \{w \mid w \in H^1(L) \text{ and } w = \bar{w} \text{ on } \Gamma_w\} \quad (4.54)$$

and  $\mathcal{V}$  be the space of admissible displacement variations written as

$$\mathcal{V} = \{\delta w \mid \delta w \in H^1(L) \text{ and } \delta w = 0 \text{ on } \Gamma_w\} . \quad (4.55)$$

### 4.3.2 Deformation Measure

We assume that plane sections remain plane, but not necessarily normal after deformation. Hence, we consider the two-dimensional motion of the centroid of the beam in the form

$$\begin{aligned} x_1 &= X_1 + u(X_1) \\ x_2 &= v(X_1) . \end{aligned} \quad (4.56)$$

From (4.56) we see that the motion of the line of centroids of the beam takes the form

$$\chi_0 = x_1 \mathbf{e}_1 + x_2 \mathbf{e}_2 = (X_1 + u(X_1)) \mathbf{e}_1 + v(X_1) \mathbf{e}_2 \quad (4.57)$$

By application of (3.6) the deformation gradient of the line of centroids for the motion  $\chi_0$  becomes

$$\mathbf{F}_0 \mathbf{E}_1 = \frac{\partial \chi_0}{\partial \mathbf{X}} \mathbf{E}_1 = (1 + u') \mathbf{e}_1 + v' \mathbf{e}_2 \quad (4.58)$$

where  $(\cdot)'$  denotes differentiation with respect to the  $X_1$  coordinate direction. The axial stretching normal to the deformed beam and shearing tangential to the deformed beam are simply the dot product between the deformation gradient of the line of centroids and the bases  $\mathbf{g}_\alpha$  on the deformed configuration

$$\begin{aligned} \delta_1 &= \mathbf{F}_0 \mathbf{E}_1 \cdot \mathbf{g}_1 = (1 + u') \cos(\theta) + v' \sin(\theta) \\ \delta_2 &= \mathbf{F}_0 \mathbf{E}_1 \cdot \mathbf{g}_2 = -(1 + u') \sin(\theta) + v' \cos(\theta) . \end{aligned} \quad (4.59)$$

From (4.59) we see that the measures of deformation take the form

$$\mathbf{\Gamma} = \mathbf{\Lambda} \mathbf{F} - \mathbf{E}_1 = \begin{Bmatrix} \delta_1 - 1 \\ \delta_2 \\ \theta' \end{Bmatrix} \quad \text{where} \quad \mathbf{F} = \begin{Bmatrix} 1 + u' \\ v' \\ \theta' \end{Bmatrix} \quad (4.60)$$

and  $\mathbf{\Lambda}$  is the transformation matrix between the Gaussian and spatial frames

$$\mathbf{g}_i = \mathbf{\Lambda} \mathbf{e}_i \quad \text{with} \quad \mathbf{\Lambda} = \begin{bmatrix} \cos(\theta) & \sin(\theta) & 0 \\ -\sin(\theta) & \cos(\theta) & 0 \\ 0 & 0 & 1 \end{bmatrix} . \quad (4.61)$$

Note from (4.60) the linearized deformation measures becomes

$$\boldsymbol{\Gamma} = \left\{ \begin{array}{c} u' \\ -\theta + v' \\ \theta' \end{array} \right\} \quad (4.62)$$

which agrees with Timoshenko beam theory, see GERE & TIMOSHENKO [1984].

**Remark 4.3.**

If the beam is initially rotated within the reference frame an appropriate coordinate transformation is performed before the computation of the deformation measure, see SACK [1989] for further details.

### 4.3.3 Variational Formulation

An approximate solution of the boundary value problem is constructed from a variational statement of the problem. The basic field equations may be included in a variational statement for the elasticity problem using a potential functional. Accordingly, we have a functional in which the deformation vector,  $\boldsymbol{w} \in \mathcal{U}$  is regarded as the independent variable. The proposed functional  $\Pi : \mathcal{U} \rightarrow \mathbb{R}$  may be expressed as

$$\Pi(\boldsymbol{w}) = \int_{\mathcal{B}} W(\boldsymbol{\Gamma}) dV + \Pi_{ext}(\boldsymbol{w}) \quad (4.63)$$

where  $W(\boldsymbol{\Gamma})$  is a stored energy function and for conservative external loading

$$\Pi_{ext}(\boldsymbol{w}) = - \int_{\mathcal{B}} \boldsymbol{b} \cdot \boldsymbol{w} dV - \int_{\Gamma_R} \bar{\boldsymbol{R}} \cdot \boldsymbol{w} dA \quad (4.64)$$

$\boldsymbol{b}$  being the body force per unit volume.

We may state the problem as: Find the  $\boldsymbol{w} \in \mathcal{U}$  which makes the functional  $\Pi(\boldsymbol{w})$  stationary for all admissible variations  $\delta\boldsymbol{w} \in \mathcal{V}$ .

The stationary point of  $\Pi$  is obtained by setting to zero the first variation of (4.63) with respect to the independent field. Accordingly,

$$\delta\Pi = \int_{\mathcal{B}} \frac{\partial W}{\partial \Gamma} \cdot \delta\Gamma \, dV - \int_{\mathcal{B}} \delta\mathbf{w} \cdot \mathbf{b} \, dV - \int_{\Gamma_t} \delta\mathbf{w} \cdot \bar{\mathbf{R}} \, dA = 0 \quad \text{in } \mathcal{B} \quad (4.65)$$

for all admissible variations  $\delta\mathbf{w} \in \mathcal{V}$ .

We may recast the first term of (4.65) as

$$\delta\Pi_{int} = \int_L \frac{\partial W}{\partial \Gamma} \cdot \delta\Gamma \, \Omega \, dX \quad (4.66)$$

which represents the internal virtual work, where for a general singly symmetric cross section

$$\frac{\partial W(\Gamma)}{\partial \Gamma} = \mathbf{R} = \begin{Bmatrix} N \\ V \\ M \end{Bmatrix} = \begin{bmatrix} D_M \Omega & 0 & -D_M Q \\ 0 & G \Omega & 0 \\ -D_M Q & 0 & D_M I \end{bmatrix} \begin{Bmatrix} \Gamma_1 \\ \Gamma_2 \\ \Gamma_3 \end{Bmatrix} = \mathbb{D} \Gamma \quad (4.67)$$

where  $\Omega$ ,  $Q$  and  $I$  are the integrated area, first moment of area and second moment of area, respectively and the variation of the deformation is

$$\delta\Gamma = \delta\Lambda \mathbb{F} + \Lambda \delta\mathbb{F} = \delta\theta \bar{\Lambda} \mathbb{F} + \Lambda \delta\mathbb{F} . \quad (4.68)$$

Substituting (4.68) into (4.65) yields

$$\delta\Pi = \int_L \left( \delta\theta^T \mathbb{F}^T \bar{\Lambda}^T + \delta\mathbb{F}^T \Lambda^T \right) \mathbf{R} \, dX - \delta\Pi_{ext} . \quad (4.69)$$

### 4.3.4 Finite Element Interpolations

The selection of the generalized displacement interpolation functions for the two node initially straight beam element will be the same as those for the bar element in the previous sections, namely,

$$N_1 = 1 - \frac{s}{L} \quad \text{and} \quad N_2 = \frac{s}{L} . \quad (4.70)$$

The position vector and generalized displacement vector follow as before.

### 4.3.5 Linear Kinematic Element

We proceed by defining the deformation measures used for the formulation, develop the expression for the internal virtual work from which the residual equations may be expressed. Lastly, the resulting nonlinear residual equations are linearized to afford a solution of the nonlinear set of equations via a Newton's method.

#### Deformation Measure

Recall the expression for the linearized deformation measure is

$$\Gamma = \left\{ \begin{array}{c} u' \\ -\theta + v' \\ \theta' \end{array} \right\} \quad (4.71)$$

where  $u$  is the displacement in the  $X_1$  coordinate direction,  $v$  is the displacement in the  $X_2$  coordinate direction and  $\theta$  is the rotation about the  $X_3$  coordinate direction.

We may express the virtual generalized deformation vector, with the aid of the interpolation functions and (4.71) as

$$\delta \Gamma = \begin{Bmatrix} \delta u' \\ -\delta \theta + \delta v' \\ \delta \theta' \end{Bmatrix}^T = \begin{Bmatrix} \delta \hat{u}_I \\ \delta \hat{v}_I \\ \delta \hat{\theta}_I \end{Bmatrix}^T \begin{bmatrix} N'_I & 0 & 0 & 0 \\ 0 & N'_I & 0 & 0 \\ 0 & 0 & N'_I & N_I \end{bmatrix} \begin{bmatrix} 1 & 0 & 0 \\ 0 & 1 & 0 \\ 0 & 0 & 1 \\ 0 & -1 & 0 \end{bmatrix} = \delta \mathbf{w}^T \mathbf{B}^T \quad (4.72)$$

where the index  $I = 1, 2$  is the local node number and  $\mathbf{w}^T = [\hat{u}_I, \hat{v}_I, \hat{\theta}_I]$ .

### Residual and Tangent Arrays

Substitution of (4.72) into the expression for the internal virtual work yields

$$\delta \Pi_{int} = \delta \mathbf{w}^T \int_L \mathbf{B}^T \mathbf{R} \Omega dX . \quad (4.73)$$

The vector postmultiplying the virtual generalized displacements in (4.73) is commonly referred to as the internal load vector and is denoted as  $\mathbf{F}_{int}$  for future developments.

#### Remark 4.4.

Recall from Chapter 3 that the stress and hence the resultant stresses  $\mathbf{R}$  are in general a function of the mechanical and thermal state and internal variables, i.e.  $\mathbf{R} = \hat{\mathbf{R}}(\varepsilon, T, \xi)$ .

To facilitate a solution of the mixed boundary value problem the nonlinear equation (4.65) is linearized and solved by a Newton's method as a sequence of linearized problems. Hence, linearizing (4.65) we obtain

$$d(\delta \Pi) = \int_L d\Gamma \frac{\partial^2 W(\Gamma)}{\partial \Gamma^2} \delta \Gamma \quad (4.74)$$

where for convenience define

$$\mathbb{D} := \frac{\partial^2 W(\boldsymbol{\Gamma})}{\partial \boldsymbol{\Gamma}^2} \quad (4.75)$$

and substituting (4.72) and (4.75) into (4.74) and collecting terms gives

$$d(\delta\Pi) = \delta\mathbf{w}^T \int_L \mathbf{B}^T \mathbb{D} \mathbf{B} dX . \quad (4.76)$$

The matrix postmultiplying the virtual generalized displacements in (4.76) is commonly referred to as the tangent matrix and is denoted as  $\mathbf{k}$ .

### 4.3.6 Non-Linear Kinematic Element

We proceed by defining the deformation measures used for the formulation, develop the expression for the internal virtual work from which the residual equations may be expressed. Lastly, the resulting nonlinear residual equations are linearized to afford a solution of the nonlinear set of equations via Newton's method.

#### Deformation Measure

Recall from previous sections the expression for the nonlinear strain measure is

$$\boldsymbol{\Gamma} = \boldsymbol{\Lambda}\mathbb{F} - \mathbf{E}_1 = \left\{ \begin{array}{c} \delta_1 - 1 \\ \delta_2 \\ \theta' \end{array} \right\} . \quad (4.77)$$

where  $\delta_1 - 1$ ,  $\delta_2$  and  $\theta'$  are interpreted as the axial strain, shear strain and curvature, respectively.

We may express the virtual generalized deformation vector with the aid of the interpolation functions as

$$\delta\eta = \begin{Bmatrix} \delta u' \\ \delta v' \\ \delta\theta' \\ \delta\theta \end{Bmatrix}^T = \begin{Bmatrix} \delta\hat{u}_I \\ \delta\hat{v}_I \\ \delta\hat{\theta}_I \end{Bmatrix} \begin{bmatrix} N'_I & 0 & 0 & 0 \\ 0 & N'_I & 0 & 0 \\ 0 & 0 & N'_I & N_I \end{bmatrix} = \delta\mathbf{w}^T \mathbf{B}^T \quad (4.78)$$

where the index  $I = 1, 2$  is the local node number and  $\mathbf{w}^T = [\hat{u}_I, \hat{v}_I, \hat{\theta}_I]$ .

### Residual and Tangent Arrays

Substitution of (4.78) into the expression for the internal virtual work yields

$$\delta\Pi_{int} = \delta\mathbf{w}^T \int_L \mathbf{B}^T \boldsymbol{\Sigma}^T \mathbf{R} \Omega \, dX \quad (4.79)$$

where

$$\boldsymbol{\Sigma}^T = \begin{bmatrix} \boldsymbol{\Lambda}^T \\ \mathbb{F}^T \bar{\boldsymbol{\Lambda}}^T \end{bmatrix} \quad \text{and} \quad \bar{\boldsymbol{\Lambda}} = \begin{bmatrix} -\sin(\theta) & \cos(\theta) & 0 \\ -\cos(\theta) & -\sin(\theta) & 0 \\ 0 & 0 & 0 \end{bmatrix} \quad (4.80)$$

The vector postmultiplying the virtual generalized displacements in (4.79) is commonly referred to as the internal load vector and is denoted as  $\mathbf{F}_{int}$  for future developments.

To facilitate a solution of the mixed boundary value problem the nonlinear equation (4.65) is linearized and solved by Newton's method as a sequence of linearized problems. Hence, linearizing (4.65) we obtain

$$d(\delta\Pi) = \int_L d\Gamma \frac{\partial^2 W(\Gamma)}{\partial \Gamma^2} \delta\Gamma + \frac{\partial W(\Gamma)}{\partial \Gamma} d(\delta\Gamma) \, dX \quad (4.81)$$

where

$$d(\delta\Gamma) = d(\delta\Lambda)\mathbb{F} + \delta\Lambda d\mathbb{F} + d\Lambda\delta\mathbb{F}, \quad (4.82)$$

$$d(\delta\Lambda) = \delta\theta\bar{\bar{\Lambda}}d\theta \quad \text{and} \quad \bar{\bar{\Lambda}} = \begin{bmatrix} -\cos(\theta) & -\sin(\theta) & 0 \\ \sin(\theta) & -\cos(\theta) & 0 \\ 0 & 0 & 0 \end{bmatrix}. \quad (4.83)$$

Substituting (4.82) and (4.83) into (4.81) and collecting terms gives

$$d(\delta\Pi) = \delta w^T \left( \int_L \mathbf{B}^T \boldsymbol{\Sigma}^T \mathbb{D} \boldsymbol{\Sigma} \mathbf{B} \, dX + \int_L \mathbf{B}^T \mathbb{G} \mathbf{B} \, dX \right) dw \quad (4.84)$$

where

$$\mathbb{G} = \begin{bmatrix} \mathbf{0} & \bar{\bar{\Lambda}}^T \mathbf{R} \\ \mathbf{R}^T \bar{\bar{\Lambda}} & \mathbb{F}^T \bar{\bar{\Lambda}}^T \mathbf{R} \end{bmatrix}. \quad (4.85)$$

The matrix postmultiplying the virtual generalized displacements in (4.84) is commonly referred to as the tangent matrix and is denoted as  $\mathbf{k}$ . Note the first term of (4.84) represents the material part of the tangent and the second term the geometric part of the tangent.

### 4.3.7 Solution Procedure

Noting that the variations  $\delta\boldsymbol{\eta}$  in the previous sections are arbitrary we obtain the finite element residual equations

$$\mathbf{F}_{int}(\boldsymbol{\eta}) - \mathbf{F}_{ext}(\boldsymbol{\eta}) = \mathbf{A} \sum_{e=1}^{nelm} [\mathbf{F}_{int}^e(\boldsymbol{\eta}_e) - \mathbf{F}_{ext}^e(\boldsymbol{\eta}_e)] = \mathbf{0} \quad (4.86)$$

where  $F_{int}$  and  $F_{ext}$  are the internal and external load vectors, respectively,  $e$  is an element within the discretization,  $nelm$  denotes the total number of elements within the discretization,  $\eta_e = \{u_{I_i} v_{I_i} \theta_{I_i}\}$  is the solution vector and  $\mathbf{A}$  is the standard finite element assembly operator.

Linearizing (4.86) about an intermediate state ( $\eta_e^{(k)}$ ) yields

$$L[F_{int}] = F_{int}^{(k)} + k^{(k)} d\eta_e \quad (4.87)$$

The resulting system of equations involves the nodal solution vector at the global level expressed as

$$\mathbf{K}^{(k)} d\eta = \mathbf{R}^{(k)} \quad (4.88)$$

where

$$\begin{aligned} \mathbf{K}^{(k)} &= \mathbf{A}_{e=1}^{nelm} [k]_e^{(k)} \\ \mathbf{R}^{(k)} &= \mathbf{A}_{e=1}^{nelm} [F^{ext} - F^{int}]_e^{(k)} \end{aligned} \quad (4.89)$$

The system (4.88) is solved and then the unknown fields are updated additively by

$$\eta_e^{(k+1)} = \eta_e^{(k)} + d\eta_e \quad (4.90)$$

The process is repeated within a particular time step  $t_n$  until convergence of the  $(k+1)^{th}$  iterate is obtained, the solution is then advanced to the next time step  $t_{n+1}$ . An overview of the algorithmic implementation is outlined in Table 4.3 below

Table 4.3: Solution outline for the beam element

---

```

Initialize Variables
Loop over time,  $t$ 
  Loop until convergence
    Initialize Variables
    Loop over elements
      Compute  $N_I$  and  $N'_I$ 
      Loop over integration points along length
        Compute  $\mathbf{F}$ 
        Loop over integration points thru depth
          Compute axial strain  $\varepsilon_s$ 
          Compute stress and material moduli  $\sigma_s$  and  $D_M$ 
          Compute  $\Omega$ ,  $Q$  and  $I$ 
          Compute and accumulate  $\mathbf{R}$ 
        End loop
      Compute  $\mathbf{F}_{int}$  and  $\mathbf{k}$ 
    End loop
    Assemble  $\mathbf{R}^{(k)}$  and  $\mathbf{K}^{(k)}$ 
  End loop
  Solve  $\mathbf{K}^{(k)}dw = \mathbf{R}^{(k)}$ 
End loop
End loop

```

---

### 4.3.8 Numerical Simulations

We consider several simulations encompassing isothermal and non-isostress loading histories to demonstrate the features of the model. The material under consideration is NiTi and its associated material parameters can be found in Table 4.2

#### **Isothermal NiTi Beam Under Cyclic Loading, $T < T_{mf}$**

We consider a ten element discretization of a NiTi cantilever beam of length  $L = 20m$  having a rectangular cross section of  $2m \times 1m$ . The cross section is divided into four layers, each of which is evaluated using a 5-pt Gauss-Lobatto quadrature rule. Standard 1-pt Gaussian quadrature was used along the axis of each element. The beam is fixed against translations

and rotations on the initial end ( $X = 0$ ) and loaded via displacement control in the  $X_2$  direction at the terminal end ( $X = L$ ). The temperature of the bar is held constant at  $T = 5$  C, which is below the martensite finish temperature. The initial state is assumed to be 100% multiple variant martensite (i.e.  $\xi_0^+ = \xi_0^- = 0.5$ ) and the loading and response curves are outlined in the figures below.

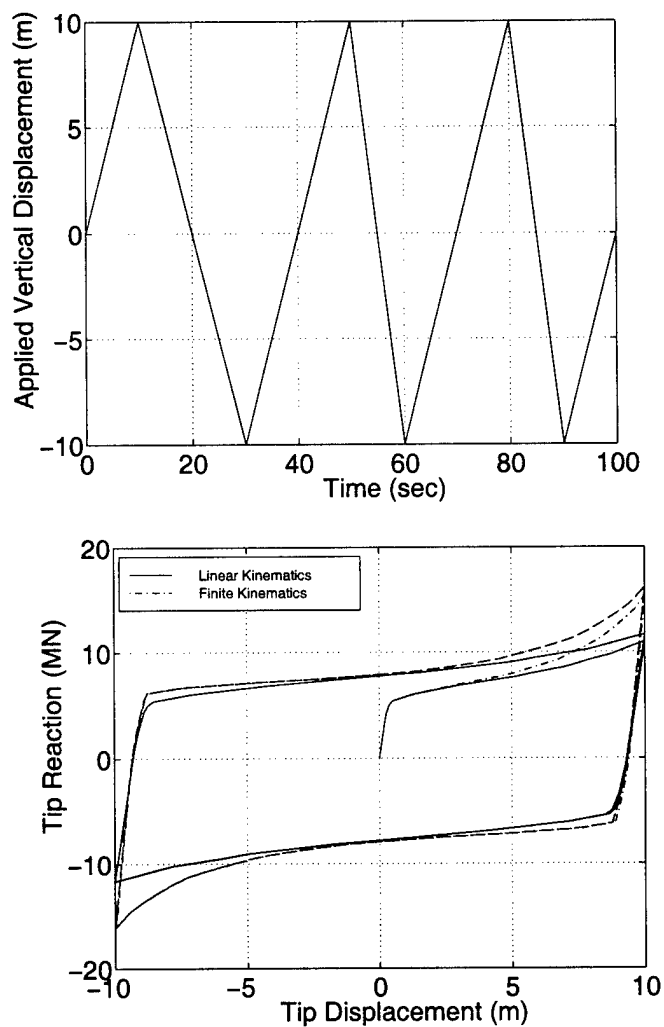


Figure 4.25: Loading and response curves for an NiTi beam under a under cyclic loading,  $T < T_{mf}$ .

From Figure 4.25 we can make the following observations:

1. The algorithm accurately determines the onset and completion of negative and positive martensitic phase transformations for each quadrature point through the depth of the beam resulting in a behavior which is qualitatively correct.
2. Although the strain levels within the beam are moderate the rotations are large and their effects are pronounced.

### **Isothermal NiTi Beam Under Cyclic Loading, $T_{as} < T < T_{af}$**

We consider a ten element discretization of a NiTi cantilever beam of length  $L = 20m$  having a rectangular cross section of  $2m \times 1m$ . The cross section is divided into four layers, each of which is evaluated using a 5-pt Gauss-Lobatto quadrature rule. Standard 1-pt Gaussian quadrature was used along the axis of each element. The beam is fixed against translations and rotations on the initial end ( $X = 0$ ) and loaded via displacement control in the  $X_2$  direction at the terminal end ( $X = L$ ). The temperature of the bar is held constant at  $T = 41.75$  C, which is above the austenite start temperature and below the austenite finish temperature. The initial state is assumed to be 50% multiple variant martensite (i.e.  $\xi_0^+ = \xi_0^- = 0.25$ ) and the loading and response curves are outlined in the figures below.

From Figure 4.26 we can make the following observations:

1. The algorithm accurately determines the onset and completion of negative and positive martensitic phase transformations for each quadrature point through the depth of the beam resulting in a behavior which is qualitatively correct.
2. The model predicts the termination of a austenite transformation when the net reaction is zero.
3. Although the strain levels within the beam are moderate the rotations are large and their effects are pronounced.

### **Isothermal NiTi Beam Under Cyclic Loading, $T > T_{af}$**

We consider a ten element discretization of a NiTi cantilever beam of length  $L = 20m$  having a rectangular cross section of  $2m \times 1m$ . The cross section is divided into four layers, each

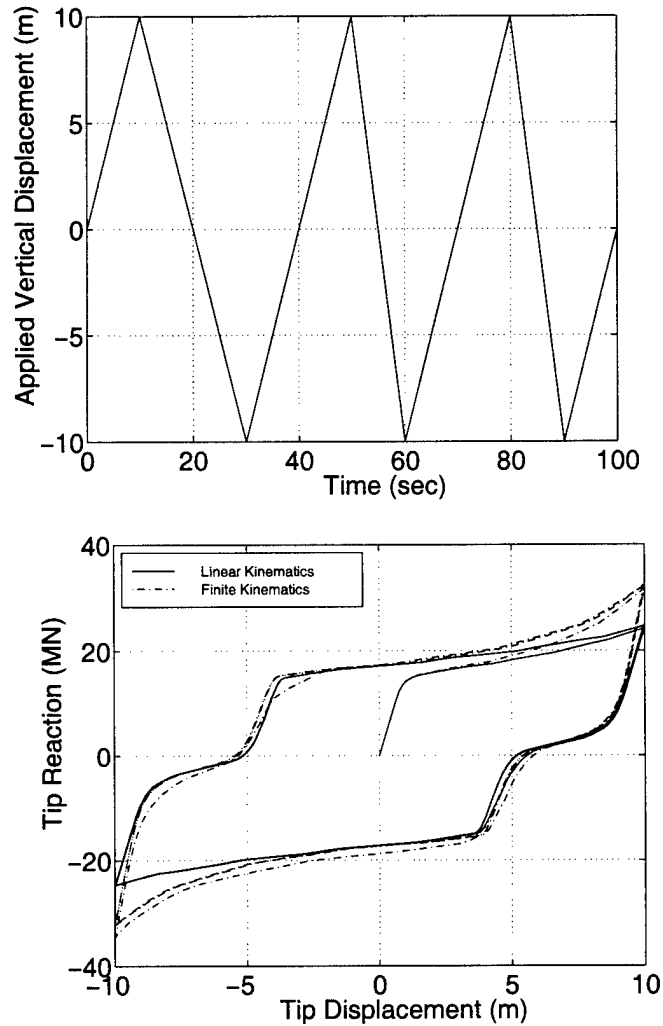


Figure 4.26: Loading and response curves for an NiTi beam under a under cyclic loading,  $T_{as} < T < T_{af}$ .

of which is evaluated using a 5-pt Gauss-Lobatto quadrature rule. Standard 1-pt Gaussian quadrature was used along the axis of each element. The beam is fixed against translations and rotations on the initial end ( $X = 0$ ) and loaded via displacement control in the  $X_2$  direction at the terminal end ( $X = L$ ). The temperature of the bar is held constant at  $T = 55$  C, which is above the austenite finish temperature. The initial state is assumed to

be 100% austenite (i.e.  $\xi_0^+ = \xi_0^- = 0$ ) and the loading and response curve are outlined in the figures below.

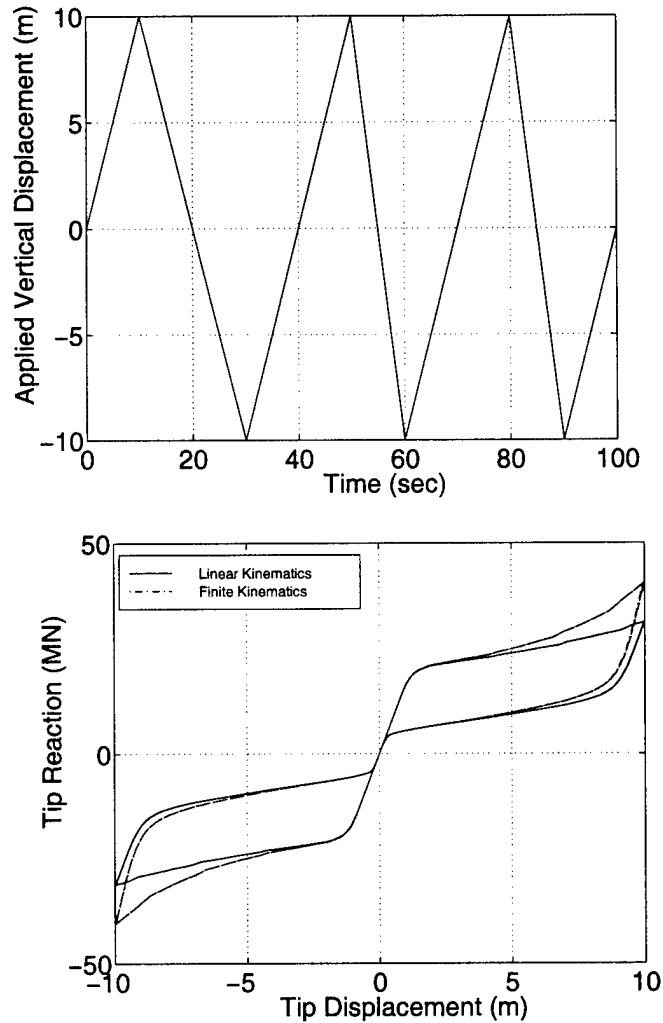


Figure 4.27: Loading and response curves for an NiTi beam under a under cyclic loading,  $T > T_{af}$ .

From Figure 4.27 we can make the following observations:

1. The algorithm accurately determines the onset and completion of negative and positive

martensitic phase transformations for each quadrature point through the depth of the beam resulting in a behavior which is qualitatively correct.

2. From the experimental data within AURICCHIO ET.AL. [1995] the model qualitatively captures the essential behavior of the pseudoelastic effect.
3. Although the strain levels within the beam are moderate the rotations are large and their effects are pronounced.

### NiTi Beam Under Thermo-mechanical Cyclic Loading

We consider a ten element discretization of a NiTi cantilever beam of length  $L = 20m$  having a rectangular cross section of  $2m \times 1m$ . The cross section is divided into two layers, each of which is evaluated using a 3-pt Gauss-Lobatto quadrature rule. Standard 1-pt Gaussian quadrature was used along the axis of each element. The beam is fixed against translations and rotations on the initial end ( $X = 0$ ) and loaded via load control in the  $X_2$  direction at the terminal end ( $X = L$ ). The bar is initially loaded and unloaded isothermally at 5 C, and lastly heated to 80 C under zero load. The initial state is assumed to be 100% multiple variant martensite (i.e.  $\xi_0^+ = \xi_0^- = 0.5$ ) and the loading and response curves are outlined in the figures below.

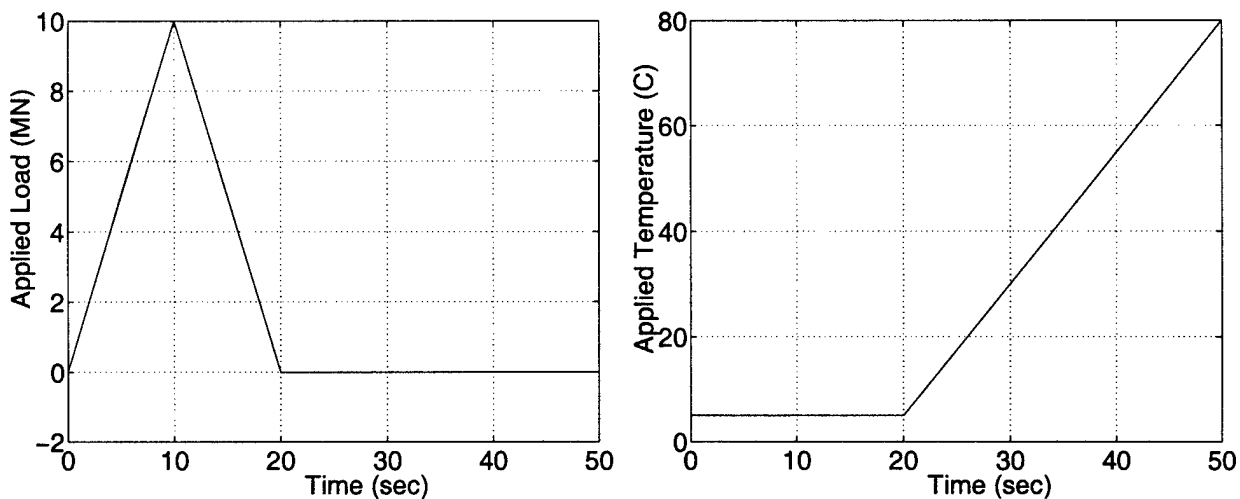


Figure 4.28: Loading and response curves for an NiTi beam under a under cyclic loading.

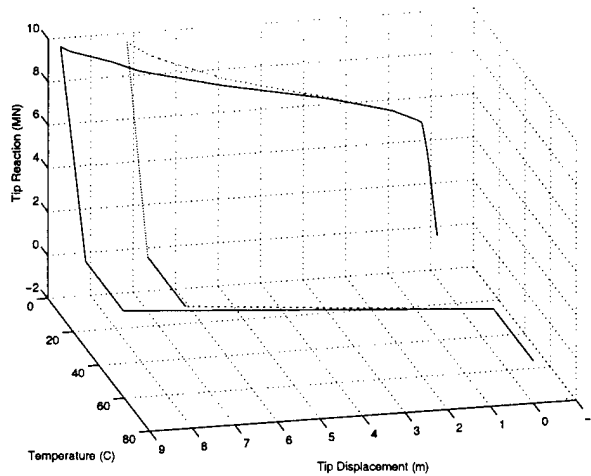


Figure 4.29: Thermo-mechanical response curves for an NiTi beam under a under cyclic loading.

From Figures 4.28 and 4.29 we can conclude that:

1. The algorithm accurately models the shape memory effect by determining the onset and completion of various phase transformations for each quadrature point.
2. Upon heating the bar we see that the residual deformation goes to zero as experimental observation shows.

**Remark 4.5.**

The simulations were also performed using various quadrature orders and total number of layers. Quadrature rules greater than 3 resulted in unconverged states during the heating cycle, specifically during the production of austenite. Initial findings indicate that since the resultant force on the cross-section is zero multiple stress distribution are admissible, thereby making state determination indeterminate. Current work in underway to determine alternative schemes for the determination of the state which maximizes the dissipative energy.

### 4.3.9 Summary of Numerical Simulations

We have considered several simulations encompassing isothermal load histories to demonstrate the features of the model for NiTi, in the setting of a linear and non-linear two dimensional beam. Several noteworthy characteristics are:

1. The algorithm accurately activates the correct evolution equation for the corresponding state on the phase diagram.
2. The algorithm accurately models both the pseudoelastic and shape memory effect.
3. The algorithm accurately determines the onset and completion of the various phase transformations.
4. Since the beam has multiple quadrature through the depth it provides a rigorous examination of the algorithm, due to the possibility of complex stress states.

## 4.4 Summary

In the previous sections we have consider the formulation of a thermomechanical constitutive model for shape memory alloys and its implementation into a multi-dimensional truss-bar and two-dimensional beam element. The simulations presented in this work provide a valuable tool for the analysis and design of shape memory devices. Some of the key features emanating from this work are outlined below:

1. The development of a new constitutive model which accounts for both compressive and tensile states of stress and the associated variant productions is presented.
2. We introduce a new algorithm for the determination of the state which accounts for nested elastic and inelastic regimes based upon the use of modified trial state variables.
3. The ability of the model to replicate the quantitative behavior for the shape memory and pseudoelastic effect is presented for both truss and beam elements for linear and finite kinematics.
4. The algorithm developed for state determination accurately computes onset, evolution and completion of the various transformations which may occur.

# Bibliography

- [1] ABEYARATNE, R. & KNOWLES, J.K. [1993], "A continuum model of a thermoelastic solid capable of undergoing phase transitions", *J. Mech. Phy. Solids*, **41**: 541-571.
- [2] ABEYARATNE, R., KIM, S-J. & KNOWLES, J.K. [1994], "Continuum Modeling of Shape-Memory Alloys", *ASME International Congress and Exposition*, Chicago, ASME, Proceedings of the Symposium on Phase Transformations and Shape Memory Alloys, AMD-Vol 189, L.C. Brinson & B. Moran Eds. : 59-69.
- [3] ACHENBACH, M. & MULLER, I. [1985], "Simulation of Material Behavior of Alloys with Shape Memory", *Arch. Mech.*, **35** : 537-585.
- [4] ACHENBACH, M. [1989], "A Model for an Alloy with Shape Memory", *Int. J. Plast.*, **5**: 371-395.
- [5] ACHENBACH, M., ATANACKOVIC, T. & MULLER, I. [1986], "A Model for Memory Alloys in Plane Strain", *Int. J. of Solids & Struct.*, **22(2)** : 171-193.
- [6] AURICCHIO, F. [1995], "Shape Memory Alloys: applications, micromechanics, macromodeling and numerical simulations", Ph.D. dissertation, University of California at Berkeley, Department of Civil Engineering.
- [7] BALL, J.M. & JAMES, R.D., [1992], "Proposed Experimental Tests of a Theory of Fine Microstructure and the 2-well Problem", *Philosophical Transactions of the Royal Society of London Series A-Physical Sciences and Engineering*, **338 (1650)**: 389-450.
- [8] BOYD, J.G. & LAGOUDAS, D.C. [1996A], "A Thermodynamic Constitutive Model for the Shape Memory Materials. Part I. The Monolithic Shape Memory Alloy", *Int. J. Plast.*, **12** 805-842.

- [9] BOYD, J.G. & LAGOUDAS, D.C. [1996B], "A Thermodynamic Constitutive Model for the Shape Memory Materials. Part II. The SMA Composite Material", *Int. J. Plast.*, **12** 843-873.
- [10] BRINSON, L.C. [1993], "One Dimensional Constitutive Behavior of Shape Memory Alloys: Thermomechanical Derivation with Non-Constant Material Functions", *J. Intell. Matl. Syst. & Struct.*, **4**: 229-242.
- [11] BRINSON, L.C. & LAMMERING, R. [1993], "Finite Element Analysis of the Behavior of Shape Memory Alloys and their Applications", *Int. J. Solids & Struct.*, **30(23)**: 3261-3280.
- [12] BUEHLER, W.J., GILFRICH, J.V. & WILEY, R.C. [1963], "A Thermomechanical Description of Materials with Internal variables in the Process of Phase Transformations", *J. Appl. Phys.*, **34**: 1475.
- [13] CHANG, L.C. & READ, T.A. [1951], "A Thermomechanical Description of Materials with Internal Variables in the Process of Phase Transformations", *Trans. AIME*, **191**: 47.
- [14] DUERIG, T.W., MELTON, K.N., STOCKEL, D. & WAYMAN, C.M. [1990], *Engineering Aspects of Shape Memory Alloys*, Butterworth-Heinemann, Boston.
- [15] FALK, F. [1980], "Model Free Energy, Mechanics, and Thermodynamics of Shape Memory Alloys", *Acta Metall.*, **28**: 1773-1780.
- [16] FERNALD, R., FRITZ, D., SIEVERT, C. & STICE, J. [1994], "NiTi: The Material of Choice for High Performance Guidewires", *Proceedings of the First International Conference on Shape Memory and Superelastic Technology*, Asilomar, California, 341-345.
- [17] FISHER, F.D., BERVEILLER, M., TANAKA, K. & OBERAIGNER, E.R. [1994], "Continuum Mechanical Aspects of Phase Transformations in Solids", *Arch. Appl. Mech.*, **65**: 54-85.
- [18] FUNAKUBO, H., [1984] *Shape Memory Alloys*, Translated by: J.B. Kennedy, Gordon and Breach Science Publishers.
- [19] GERE, J.M. & TIMOSHENKO, S.P. [1984], "Mechanics of Materials", 2nd ed., Brooks/Cole Eng. Div., Monterey, Ca.
- [20] GOVINDJEE, S. & KASPER, E.P. [1998], "A Shape Memory Model for Uranium-Niobium Accounting for Plasticity", *J. Intell. Mat. Sys. Struct.* (in press).
- [21] GURTIN, M.E. [1981], *An Introduction to Continuum Mechanics*, Academic Press.

- [22] HUGHES [1987], *The Finite Element Method*, Prentice-Hall, Englewood Cliff, N.J.
- [23] IVSHIN, Y. & PENCE, T.J. [1994A], "A Constitutive Model for Hysteretic Phase Transformation Behavior", *Int. J. Eng. Sci.*, **32**: 681-704.
- [24] IVSHIN, Y. & PENCE, T.J. [1994B], "A Thermomechanical Model for a One Variant Shape Memory Material", *J. Intell. Matl. Syst. & Struct.*, **5**: 455-473.
- [25] KAFKA, V. [1994A], "Shape Memory: A New Concept of Explanation and Mathematical Modeling. Part I: Micromechanical Explanation of the Causality in the SM Processes", *J. Intell. Matl. Syst. & Struct.*, **5**: 809-814.
- [26] KAFKA, V. [1994B], "Shape Memory: A New Concept of Explanation and Mathematical Modeling. Part II: Mathematical Modeling of the SM Effect and of Pseudoelasticity", *J. Intell. Matl. Syst. & Struct.*, **5**: 815-824.
- [27] KIM, S-J. & ABEYARATNE, R. [1995], "On the Effect of the Heat Generated During a Stress Induced Thermoelastic Phase Transformation", *Continuum Mechanics & Thermodynamics*, **7**: 311-332.
- [28] LIANG, C. & ROGERS, C.A. [1990], "One-Dimensional Thermomechanical Constitutive Relations for Shape Memory Materials", *J. Intell. Matl. Syst. & Struct.*, **1**: 207-234.
- [29] MANACH, P.Y., FAVIER, D. & RIO, G. [1996], "Finite Element Simulations of Internal Stresses Generated During the Ferroelastic Deformation of NiTi Bodies", *J. Physique III*, International Conference on Martensitic Transformation, ICOMAT 95 Part II, Vol **6**, Colloque C1: 235.
- [30] MULLER, I. & XU, H. [1991], "On the pseudo-elastic hysteresis", *Acta Metall.*, **39**: 263-271.
- [31] MULLER, I. & WILMANSKI, K. [1981], "Memory Alloys, Phenomenology and Ersatz Model", in Brulin, O., Hsieh, R.K.T. (eds.), *Continuum Models of Discrete Systems*, **4**, North Holland Pub. Co.
- [32] OZAKI, Y., VIOLARIS, A.G. & SERUYS, P.W. [1996], "New Stent Technologies", *Progress in Cardiovascular Diseases*, **XXXIX (2)**: 129-140.
- [33] PATOOR, E., EBERHARDT, A & BERVEILLER, M. [1996], "Micromechanical Modeling of Superelasticity in Shape Memory Alloys", *J. Physique III*, International Conference on Martensitic Transformation, ICOMAT 95 Part II, Vol **6**, Colloque C1:277.

- [34] SIMO, J.C., HJELMSTAD, K.D. & TAYLOR, R.L. [1984], "Numerical Formulations of Elasto-Viscoplastic Response of Beams Accounting for the Effect of Shear", *Computer Methods in Applied Mechanics and Engineering*, **42**: 301-330.
- [35] SACK, R.L. [1989], "Matrix Structural Analysis", PWS-KENT Pub. Co., Boston
- [36] SIGWART, U. [1997], "Ten Years of Stenting: What Next?", *Journal of Interventional Cardiology*, **10 (3)**: 195-205.
- [37] SUN, Q.P. & HWANG, K.C. [1993A], "Micromechanics Modeling for the Constitutive Behavior of Polycrystalline Shape Memory Alloys - I. Derivation of General Relations", *J. Mech. Phys. Solids*, **41**: 1.
- [38] SUN, Q.P. & HWANG, K.C. [1993B], "Micromechanics Modeling for the Constitutive Behavior of Polycrystalline Shape Memory Alloys - II. Study of the Individual Phenomena", *J. Mech. Phys. Solids*, **41**: 19.
- [39] TANAKA, K. & IWASAKI, R [1985], "A Phenomenological Theory of Transformation Superplasticity", *Ing. Arch.* , **51** : 287-299.
- [40] TANAKA, K. [1986], "A Thermomechanical Sketch of Shape Memory Effect: One Dimensional Tensile Behavior", *Res. Mech.*, **18**: 251-263.
- [41] TRUESDELL, C. & NOLL, W. [1992], *The Non-linear Field Theories of Mechanics*, 2nd Edition, Springer Verlag.
- [42] WAYMAN, C.M. [1980], "Some Applications of Shape Memory Alloys" *Journal of Metals*, June : 129-137.
- [43] WU, K., YANG, F., PU, Z. & SHI, J. [1996], "The Effect of Strain Rate on Detwinning and Superelastic Behavior of NiTi Shape Memory Alloys", *J. Intell. Matl. Syst. & Struct.*, **7**: 138-144.
- [44] ZIENKIEWICZ, O.C. & TAYLOR, R.L. [1989], "The Finite Element Method, Vol 1.", 4th ed., McGraw-Hill, London.

## Part III

# A Nonlinear Composite Shell Theory

# 1. GEOMETRICALLY NONLINEAR APPROACHES

## FOR FINITE ELEMENT ANALYSIS

### 1.1 Introduction

A general purpose finite element code having powerful and reliable geometric and material nonlinear capabilities is an essential tool for today's structural engineer. In this work we have endeavored to extend a multi-layered shear deformable composite shell theory, initially designed for linear analysis only, to the nonlinear regime. In the first phase of the enhancement for nonlinear analysis, a geometrically nonlinear capability for large displacements and rotations but small strains has been implemented.

A comprehensive literature review was conducted on geometrically nonlinear finite element approaches and nonlinear solution techniques developed in the last two decades. As discussed in the following sections, the element co-rotational procedure was selected along with a nonlinear solution technique for handling the geometric nonlinearity. This co-rotational procedure is ideally suited to extending an existing linear finite element code to perform geometrically nonlinear analysis. The theoretical issues related to the implementation of the co-rotational procedure are discussed and the close relationship between the updated Lagrangian formulation and the co-rotational procedure is revealed. All the approximations made in the co-rotational procedure as well as the restrictions and limitations caused by them are also identified.

### 1.2 Background on Total and Updated Lagrangian Formulation

In the past two decades, significant advancements have been made in the development of efficient and convenient finite element theories for large deflection and inelastic response of complex structures. Several formulation strategies and procedures are available for accommodating large rotation capabilities. The advances made have been prompted by an improved understanding of the physical principles involved and the continuing advances in computer

technology.

When large displacements, large rotations and even finite strain nonlinear constitutive relations are involved in problems, an incremental solution technique is generally required and either a total Lagrangian or an Eulerian coordinate system is employed to establish the finite element equilibrium equations. The former coordinate system results in equilibrium equations in terms of the initial undeformed configuration whereas the latter coordinate system results in equilibrium equation with respect to the final deformed configuration. However, because the final deformed configuration is determined as a part of the solution, an Eulerian formulation reduces to an updated Lagrangian formulation, where the equilibrium state obtained for the previous load increment (or iteration) is employed as the reference configuration for the current load increment (or iteration).

### 1.3 Basic Philosophy of the Co-rotational Procedure

Unfortunately, neither the total nor the updated Lagrangian formulation can be simply incorporated into existing linear finite element codes. It is well known in continuum mechanics that the motion of a continuous medium can always be decomposed into a rigid body motion followed by a pure deformation. If the finite element is small enough to provide a valid approximation of the continuous body, then the motion of each individual finite element can be similarly decomposed. In particular, the motion of a flexible shell or beam finite element can be conceived as a finite rigid body motion followed by relatively small pure deformation. *The latter is not involved with geometrical nonlinearities and the former is not involved in the constitutive equations* for the element. If the rigid body motion part is eliminated from the total displacements, the deformational part of the motion is always a small quantity relative to the local element axes. Since the strain is small, the deformational displacement derivatives with respect to the local element coordinates (convected coordinates) must be in the same order of magnitude as the strains. As a result, the second order terms in the Green-Lagrange

strain formulation can be dropped [3] and the linear finite element theory can be adopted for geometrically nonlinear analysis.

Based on this concept, Belytschko and Hsieh [4] developed a co-rotational procedure for nonlinear transient analysis and Wempner [5] proposed a finite rotation and small strain finite element theory for flexible shell elements in static analysis. In [4], each element is associated with a local convected coordinate system which is assumed to rotate relative to the fixed global coordinate system by the rigid body rotation of that element. With this convected coordinate system, the total displacements and rotations were easily decomposed and the geometrical nonlinearities caused by large rotations were treated entirely by transformations between the global and the convected coordinates.

Since the co-rotational procedure reported in [4,5], many elements based on this procedure have been developed for geometrically nonlinear analysis. Harrigmoen and Bergan [6] successfully applied the co-rotational procedure to linear flat triangular and rectangular shell elements for large rotation analysis. In their study, the local convected coordinate system was naturally defined by using the direction cosines of the mid-surface normal and one edge of the element. Excellent results for several typical problems involving large rotations and buckling and/or bifurcation points were obtained.

#### **1.4 Solution Techniques for Nonlinear Finite Element Equations**

The nonlinear finite element equations of motion are normally expressed as a set of nonlinear algebraic equations containing nodal displacements and external load vectors. Among them, each algebraic equation states the equilibrium condition of an individual degree-of-freedom in the finite element model. For the case of *proportional loading*, the external load vector can always be expressed as the product of an arbitrarily defined reference external load vector and a scalar called the load parameter. Actually the load-displacement curves are determined by these  $N$  nonlinear algebraic equations about  $(N + 1)$  unknowns where  $N$

is the total degrees-of-freedom of the finite element model.

The finite element equations can be solved in various ways, for instance, by the **pure incremental method** (without equilibrium iteration), the **iterative method based on the secant stiffness relations** or the **combined incremental-iterative method** based on the *Newton-Raphson* scheme. The finite element stability analysis is characterized by a singular or ill-conditioned tangent stiffness matrix at or in the vicinity of the critical load point. In the full Newton-Raphson method where the stiffness matrix is modified at the end of each iteration, it is quite possible that the critical point may be hit exactly and as a result the iterative procedure break down. However, the modified Newton-Raphson method is better at avoiding the critical point and is therefore highly recommended in buckling analysis [13]. According to several researchers [12–15], and our experiences, the exact singularity in tangent stiffness matrix is extremely unlikely to be encountered in practical computation if the modified Newton-Raphson method is employed. Therefore we employ the Modified Newton Raphson Method together with the line-search technique to solve the resulting nonlinear system of equations.

## 2. ELEMENT COROTATIONAL FORMULATION FOR GEOMETRICALLY NONLINEAR ANALYSIS OF MULTILAYERED SHELLS

In this section the theoretical formulation of the element co-rotational procedure for geometrically nonlinear analysis is presented. Following a brief introduction identifying the main attributes of the total and updated Lagrangian formulations, the co-rotational procedure is derived from the updated Lagrangian method consistently by making a series of approximations based on the assumption of small strain. The sources of possible numerical errors and restrictions on the co-rotational procedure resulting from the approximations in its derivation are also discussed.

To present the nonlinear finite element theory, we consider the motion of a general body in a stationary Cartesian coordinate system. It is assumed that the general body can experience large displacements and rotations, large strains, and a nonlinear constitutive response. In static analysis, the time variable is employed just for convenience in describing the loading process. It is obvious that the objective of nonlinear analysis is to evaluate the equilibrium positions of the complete body at a series of discrete time points  $0, \Delta t, 2\Delta t, 3\Delta t, \dots$ , where the time increment  $\Delta t$  corresponds to the load increment. In an incremental solution procedure, assuming that the solutions for the static and kinematic variables for all the time points from 0 to  $t$  have been obtained, we have to develop a solution strategy to solve for the next required equilibrium position corresponding to time  $t + \Delta t$ .

In the Lagrangian incremental analysis approach, we can express the equilibrium of the body at time  $t + \Delta t$  using the principle of virtual work. Using tensor notation, this principle requires that

$$\int_{\Omega_t} \boldsymbol{\sigma}_{n+1} \delta \boldsymbol{\varepsilon}_{n+1} d\Omega = \mathbf{f}_{n+1}^{\text{ext}} \quad (1)$$

where  $\boldsymbol{\sigma}_{n+1}$  is the Cauchy stress tensor,  $\boldsymbol{\varepsilon}_{n+1}$  is the infinitesimal strain tensor, and the  $\delta$

represents variation. Both  $\sigma_{n+1}$  and  $\varepsilon_{n+1}$  are referred to the configuration at time  $t + \Delta t$ . The external virtual work,  $f_{n+1}^{ext}$  can be expressed as

$$f_{n+1}^{ext} = \int_{\Omega_t} f_{n+1}^b \delta u d\Omega + \int_{\Gamma_t} f_{n+1}^s \delta u d\Gamma \quad (2)$$

where  $f_{n+1}^b$  and  $f_{n+1}^s$  indicate the externally applied body and surface force vectors, respectively, and  $\delta u$  is the virtual displacement vector.  $\Omega_t$  and  $\Gamma_t$  denote the volume and surface corresponding to the equilibrium configuration at time  $t + \Delta t$ .

It should be noted that the principle of virtual work presented in equation (1) is established in the unknown equilibrium configuration at time  $t + \Delta t$ . This is a fundamental difference compared with linear analysis in which it is assumed that the displacements are infinitesimally small so that the configuration of the body does not change. To overcome this difficulty, either the total Lagrangian or the updated Lagrangian formulation is usually employed.

*Remark:* In the following we will follow the notation from Marsden and Hughes [1983].

## 2.1 Total Lagrangian Formulation

In the total Lagrangian formulation, the principle of virtual work (1) is established with respect to the initial undeformed configuration at time 0.

$$\int_{\Omega_o} S_{n+1} \delta E_{n+1} d\Omega_o = F_{n+1}^{ext} \quad (3)$$

where  $E_{n+1}$  is the Green-Lagrange strain tensor given by

$$E_{n+1} = \frac{1}{2}(U_{I,J} + U_{J,I} + U_{K,I} U_{K,J})_{n+1} \quad (4)$$

In (4), the displacement gradients  $U_{I,J}$  with respect to the initial undeformed configuration at time 0 are defined as

$$U_{I,J} = \frac{\partial U_I}{\partial X_J} \quad (5)$$

where  $U$  indicates the total displacements referred to the initial configuration and  $X$  represents the coordinates in the initial configuration.  $S_{n+1}$  denotes the second Piola-Kirchhoff

stress tensor which is related to the Cauchy stress tensor by a stress transformation as follows:

$$\mathbf{S}_{n+1} = J \mathbf{F}_{n+1}^{-1} \boldsymbol{\sigma}_{n+1} \mathbf{F}_{n+1}^{-T} \quad (6)$$

where  $J$  is the Jacobian of transformation and  $\mathbf{F}^{-1}$  is the inverse of the deformation gradient matrix, namely,

$$F_{iI} = \frac{\partial x_i}{\partial X_I} \quad ; \quad F_{iI}^{-1} = \frac{\partial X_I}{\partial x_i} \quad (7)$$

Because the second Piola-Kirchhoff stress tensor and the Green-Lagrange strain tensor are energetically conjugate, they can be used as a pair in the principle of virtual work.

*Remark:* It should be noted that the Cauchy stress tensor, which corresponds to the internal force per unit area in the final deformed configuration, represents the true stress state in the deformed body. However, the second Piola-Kirchhoff stress tensor, which is interpreted as internal force per unit area in the initial configuration, does not represent the true stress state in the structure and cannot be used directly in engineering design.

Defining the displacement increments within the load step from  $t$  to  $t + \Delta t$  as follows:

$$\Delta \mathbf{U} = \mathbf{U}_{n+1} - \mathbf{U}_n \quad (8)$$

We can divide the Green-Lagrange strain increment  $\Delta \mathbf{E} = \mathbf{E}_{n+1} - \mathbf{E}_n$  into linear and non-linear parts as

$$\Delta \mathbf{E} = \mathbf{E}^l + \mathbf{E}^{nl} \quad (9)$$

where

$$E_{IJ}^l = \frac{1}{2}(U_{I,J} + U_{J,I} + (U_{K,I})_n U_{K,J} + U_{K,I} (U_{K,J})_n) \quad (10)$$

and

$$E_{IJ}^{nl} = \frac{1}{2} U_{K,I} U_{K,J} \quad (11)$$

*Remark:* The initial displacement terms  $(U_{K,I})_n$  and  $(U_{K,J})_n$  introduce the initial displacement effect in the elastic stiffness matrix and the internal force vector.

The second Piola-Kirchhoff stress tensor in equation (3) can be expressed as the summation of the stress components at time  $t$  and a small increment as

$$\mathbf{S}_{n+1} = \mathbf{S}_n + \Delta \mathbf{S} \quad (12)$$

Substituting (9) and (12) the principle of virtual work (3), denoting  $\delta \mathbf{E}_{n+1} = \delta \Delta \mathbf{E}$  and neglecting the quadratic terms, we obtain the linearized equations of motion in incremental form

$$\int_{\Omega_o} \mathbf{E}^l : \mathbf{C} : \delta \mathbf{E}^l d\Omega + \int_{\Omega_o} \mathbf{S}_n \delta \mathbf{E}^{nl} d\Omega = \mathbf{F}_{n+1}^{\text{ext}} - \int_{\Omega_o} \mathbf{S}_n \delta \mathbf{E}^l d\Omega \quad (13)$$

where the constitutive tensor  $\mathbf{C}$  is used to relate the incremental second Piola-Kirchhoff stress to the linear part of the incremental Green-Lagrange strain in the first term on the left hand side in (13) as

$$\Delta \mathbf{S} = \mathbf{C} : \mathbf{E}^l \quad (14)$$

*Remark:* It should be pointed out that because constitutive equation (14) is given in incremental form, it can be understood as a linearization of any general nonlinear constitutive relation.

The linearized principle of virtual work presented in (13) can be employed to calculate an increment in the displacements for prescribed external load at  $t + \Delta t$ , which is then used to evaluate the approximation to the total displacements, strains and stresses corresponding to the time  $t + \Delta t$ . The displacement approximations corresponding to  $t + \Delta t$  are simply obtained by adding the calculated displacement increments to the displacements at time  $t$ . The strain and stress approximations are then evaluated from the displacements using the kinematic relation and the constitutive relation.

After obtaining the approximate displacements, strains and stresses, we check the difference between external virtual work and the internal virtual work evaluated from the obtained approximate static and kinematic variables at time  $t + \Delta t$ . Denoting the approximate values with a superscript  $(i)$  in anticipation that an iteration will, in general, be necessary, the

residual due to linearization (13) is

$$Residual = \mathbf{R}_{n+1}^{(i)} = \mathbf{F}_{n+1}^{ext} - \int_{\Omega_o} \mathbf{S}_{n+1}^{(i)} \delta \mathbf{E}_{n+1}^{l(i)} d\Omega \quad (15)$$

*Remark:* It is important to note that the right hand side of (15) is equivalent of the right hand side of (13). However, in (15) the current value of stress and strain variables are employed. The above considerations show that the right hand side terms in (13) and (15) are the “out-of-balance virtual work”.

In order to reduce the out-of-balance virtual work to within a certain convergence measure, iterations are normally required. Denoting the iteration number by superscript ( $i$ ), we have, for  $i = 1, 2, 3, \dots$

$$\int_{\Omega_o} \mathbf{E}_{n+1}^{l(i+1)} : \mathbf{C} : \delta \mathbf{E}_{n+1}^l d\Omega + \int_{\Omega_o} \mathbf{S}_{n+1} \delta \mathbf{E}_{n+1}^{nl(i+1)} d\Omega = \mathbf{F}_{n+1}^{ext} - \int_{\Omega_o} \mathbf{S}_{n+1}^{(i)} \delta \mathbf{E}_{n+1}^{l(i)} d\Omega \quad (16)$$

During the iterations the displacements are updated as follows

$$\mathbf{U}_{n+1}^{(i+1)} = \mathbf{U}_{n+1}^{(i)} + \Delta \mathbf{U}_{n+1}^{(i+1)} \quad (17)$$

where  $\Delta \mathbf{U}_{n+1}^{i+1}$  in (17) indicates the displacement increment obtained from iteration  $i$  to  $i + 1$ . The initial displacement in any typical step is the last converged displacement in the previous step and is given by

$$\mathbf{U}_{n+1}^{(o)} = \mathbf{U}_n \quad (18)$$

## 2.2 Updated Lagrangian Formulation

The updated Lagrangian formulation also can be derived from the principle of virtual work given in equations (1) and (2). However, in contrast to the total Lagrangian formulation, the updated Lagrangian method involves the principle of virtual work being established for the equilibrium configuration at the previous load increment at time  $t$ .

$$\int_{\Omega_t} \frac{1}{J} \boldsymbol{\tau}_{n+1} \delta \boldsymbol{\varepsilon}_{n+1} d\Omega = \mathbf{r}_{n+1} \quad (19)$$

where  $\tau_{n+1}$  and  $\varepsilon_{n+1}$  denote the second Piola-Kirchhoff stress tensor and the Green-Lagrange strain tensor measured in the updated configuration at time  $t$ , respectively. The equilibrium configuration at time  $t$  is then called the reference configuration for current load step. The updated Lagrangian formulation can therefore be visualized as a piecewise total Lagrangian formulation.

In the updated Lagrangian formulation, an incremental displacement is defined with respect to the configuration at time  $t$ . The stress components can therefore be expressed as the sum of stress components at time  $t$  and a small increment in the same way as in (12). The strain components are similarly decomposed into their linear and nonlinear parts,

$$\varepsilon_{n+1} = e_{n+1} + \eta_{n+1} \quad (20)$$

where the linear part is defined as

$$e_{n+1} = \frac{1}{2}(u_{i,j} + u_{j,i})_{n+1}$$

and the non-linear part is defined as

$$\eta_{n+1} = \frac{1}{2}(u_{k,i} u_{k,j})_{n+1}$$

*Remark:* It is important to note that the initial displacement effect disappears in the updated Lagrangian formulation. Actually, it has been taken into account implicitly through the continuous updating of the reference configuration.

Substituting the updated stresses and strains in (19), and introducing the linearized incremental constitutive relation

$$\sigma = \frac{1}{J} \tau = c : e \quad (21)$$

and neglecting the quadratic terms, we obtain the linearized equation of motion

$$\int_{\Omega_t} e : c : \delta e d\Omega + \int_{\Omega_t} \sigma \cdot \delta \eta d\Omega = f^{\text{ext}} - \int_{\Omega_t} \sigma \delta e d\Omega \quad (22)$$

Defining the out-of-balance virtual work as

$$Residual = \mathbf{r}^{(i)} = \mathbf{f}_{n+1}^{ext} - \int_{\Omega_t} \boldsymbol{\sigma}_{n+1}^{(i)} \delta \mathbf{e}_{n+1}^{(i)} d\Omega \quad (23)$$

We establish the Newton-Raphson iteration procedure for updated Lagrangian formulation as follows,

$$\int_{\Omega_t} \mathbf{e}_{n+1}^{(i+1)} : \mathbf{c} : \delta \mathbf{e}_{n+1} d\Omega + \int_{\Omega_t} \boldsymbol{\sigma}_{n+1} \delta \boldsymbol{\eta}_{n+1}^{(i+1)} d\Omega = \mathbf{f}_{n+1}^{ext} - \int_{\Omega_t} \boldsymbol{\sigma}_{n+1}^{(i)} \delta \mathbf{e}_{n+1}^{(i)} d\Omega \quad (24)$$

After each iteration, displacements are accumulated in the same way as in the total Lagrangian formulation (7) and the incremental second Piola-Kirchhoff stress and Green-Lagrangian strain tensors are evaluated which are then pushed forward to the current configuration. In order to evaluate the out-of-balance virtual work in (24), a transformation has to be performed to obtain the current Cauchy stress tensor as follows,

$$\boldsymbol{\sigma}_{n+1} = \frac{1}{J_{n+1}} \boldsymbol{\tau}_{n+1} = \frac{1}{J_n} \boldsymbol{\tau}_n + \frac{1}{J_{n+1}} (\mathbf{F}_{n+1} \Delta \mathbf{S}_{n+1} \mathbf{F}_{n+1}^T) \quad (25)$$

The variation of strain tensor  $\delta \mathbf{e}_{n+1}^{(i)}$  are now evaluated with respect to the latest configuration as

$$\delta \mathbf{e}_{n+1}^{(i)} = \delta \frac{1}{2} (\nabla \mathbf{u}^{(i)} + \nabla \mathbf{u}^{(i)T}) \quad (26)$$

and furthermore, the integration of the right hand side of (24) is carried out over the latest configuration  $\Omega_{n+1}^{(i)}$  as well.

Substituting now the element geometry and displacement interpolations into equations (16) and (24) as we would do in linear analysis, we obtain the incremental-iterative procedures for general finite element nonlinear analysis. For total Lagrangian formulation, we have

$$(\mathbf{K}_n^l + \mathbf{K}_n^{nl}) \Delta \mathbf{U}^{(i+1)} = \mathbf{F}_{n+1}^{ext} - \mathbf{F}_{n+1}^{int(i)} \quad (27)$$

and for updated formulation, we have,

$$(\mathbf{k}_n^l + \mathbf{k}_n^{nl}) \Delta \mathbf{u}^{(i+1)} = \mathbf{f}_{n+1}^{ext} - \mathbf{f}_{n+1}^{int(i)} \quad (28)$$

In both (27) and (28), the iteration matrices called the tangent stiffness matrices are on the left-hand side and include the elastic stiffness matrix and geometric stiffness matrix. The right hand side vectors are out-of-balance force vectors which represent the difference between the externally applied load vector and the internal force vector associated with the stresses in the structure.

*Remark:* It can be shown that the tangent stiffness matrices and out-of-balance force vectors evaluated in equations (27) and (28) are identical. (See Bathe [1994]).

To appreciate the difficulties of implementing the Lagrangian formulations into an existing standard linear finite element code, it is helpful to compare (27) and (28) with standard finite element equations for linear analysis, say

$$\mathbf{K}d = \mathbf{F}$$

It is readily recognized that in the Total Lagrangian formulation, although all the spatial derivatives and integrations are with respect to the initial undeformed configuration and the geometric stiffness matrix has the same form as that in linear buckling analysis, we still have three major difficulties:

- (1) Because of the initial displacement effect, the formulation of the elastic stiffness matrix  $\mathbf{K}_n^l$  becomes much more complicated than that in the linear analysis.
- (2) The addition of the quadratic displacement derivative terms in the expression of the Green-Lagrange strain tensor to the linear strain-displacement relation may require significant changes in organization of the linear finite element code.
- (3) The evaluation of internal force vectors is computationally complicated and involves considerable coding efforts.

In the updated Lagrangian formulation, because the continuous updating of the reference configuration eliminates the initial displacement effect, both the *elastic stiffness* matrix,  $\mathbf{k}_n^l$

and the *geometric stiffness* matrix  $k_n^{nl}$  have the same form as that in linear analysis. Furthermore, the formulation of internal force vector is somewhat simplified as well. However, we still have a number of difficulties as enumerated below:

- (1) We have to deal with quadratic terms in the Green-Lagrange strain tensor.
- (2) We need to carry out a complicated transformation to establish the current Cauchy stress tensor.
- (3) We need to calculate the new spatial derivatives with respect to the latest obtained configurations at the end of each iteration.

If we want to solve more general nonlinear problems, such as those involving large strains or nonlinear materials, the exact Lagrangian approaches must be employed to generate reliable finite element solutions. Fortunately, in the case of small strains, a series of approximations can still be made to degenerate the updated Lagrangian formulation to element co-rotational procedure, as explained below.

### 2.3 Element Corotational Procedure

The total and updated Lagrangian formulations discussed in previous section are so general that they are able to handle any kinds of nonlinearity, i.e., large displacements, large rotations, finite strains as well as various forms of nonlinear constitutive relations. However in the case of small strains, a series of approximations can be made to significantly simplify the Lagrangian formulations.

Theoretically, an arbitrary motion of a general continuous medium can always be decomposed into a rigid body motion followed by a pure relative deformation. In finite element analysis, this decomposition can be accomplished by defining a local convected coordinate system for each element which translates and rotates with the element, but not deform with the element. If the finite element is sufficiently small, the pure deformation part of displacement obtained by subtracting the rigid-body motion components from the total displacement

is normally small. Consequently, the linear theory can be applied. This is the key idea of the "Co-rotational Procedure".

In the following, we endeavour to show the close relationship between co-rotational procedure and updated Lagrangian formulation. From this relationship we establish some simple but mathematically consistent procedures for updating element stresses and calculating internal force vector.

Because of the small strain assumption, the pure deformation part of the displacements is always a small quantity as compared to the element dimensions in the local convected coordinate system. Consequently, it is reasonable for us to make the following two approximations:

- 1) The changes in element shapes are small in each individual local increment; and
- 2) The displacement derivatives of the pure deformation part of the displacements with respect to the current configuration measured in the local convected coordinate system are of the same order as the small strains. Furthermore, the quadratic terms in the Green-Lagrange strain components are neglected.

The second approximation was first introduced by Belytschko and Hsieh [4]. From the above two approximations, it follows that the linear theory can be employed in the element local convected coordinate system to provide geometrically nonlinear solutions to large displacements, large rotation, but small strain problems.

*Remark:* Although all the motions of a continuous body can be theoretically decomposed into rigid-body and pure deformation components, in practical computations, the numerical performance of the co-rotational procedure greatly depends upon the method of construction of the local convected coordinate system. The more completely the rigid body motion is isolated from the total displacement field, the more accurate the finite element solution provided by the co-rotational procedure is.

In order to present the corotational procedure, we refer the three sets of coordinate sys-

tems. They are:

- (i) The Global Coordinate System which is the Cartesian coordinate system fixed in space.
- (ii) The Local Convected Coordinate System,  $\mathbf{I} = [i_1, i_2, i_3]$  which is associated with each element and undergoes rigid body rotations and translations with the element, and
- (iii) The Surface Coordinate System,  $\mathbf{V}_i$ , which is the nodal triad associated with node  $i$  in a structural element. During the equilibrium iteration,  $\mathbf{V}_i$  experiences both the rigid body rotations and pure deformation. Obviously  $\mathbf{V}_i$  can be measured in either global or local convected coordinate system, as

$$\mathbf{V}_i = [v_{i,1}, v_{i,2}, v_{i,3}] = \mathbf{I} = [\tilde{v}_{i,1}, \tilde{v}_{i,2}, \tilde{v}_{i,3}]$$

where  $i$  denotes the node number and tilde indicates quantities measured in the local convected coordinate systems.

In order for the linear finite element theory to generate sufficiently accurate results for nonlinear problems, the deformation part of the displacements must be kept as small as possible during the solution process. As a result, it is appropriate to update the reference configuration after the equilibrium state has been reached for each load increment. In this way, the displacement we are dealing with will be just the displacement increment in the current load step defined in equation (17). Because this concept is identical to that employed in the updated Lagrangian formulation, equation (28) will be an appropriate starting point for our derivation of the co-rotational procedure.

It has been pointed out in the previous section that in updated Lagrangian formulation, if the modified Newton-Raphson iterative method is adopted, the elastic and geometric stiffness matrices have the same form as in linear analysis. (See Bathe [1994]). The main difficulty arises in the calculation of the internal force vector. The internal force vector in (28) can be expressed, for an individual element, as:

$$\mathbf{f}_{n+1}^{\text{int}(i)} = \int_{\Omega_{n+1}^{(i)}} \mathbf{B}^{(i)T} \boldsymbol{\sigma}_{n+1}^{(i)} d\Omega \quad (29)$$

where  $\mathbf{B}^{(i)T}$  has the same form as in ordinary linear finite element analysis, but contains the spatial derivatives with respect to the latest configuration obtained, i.e.,  $\Omega_{n+1}^{(i)}$ , which is not necessarily in equilibrium state.  $\boldsymbol{\sigma}_{n+1}^{(i)}$  is the Cauchy stress tensor and is also measured in the latest configuration. To obtain exact Cauchy stress tensor, we have to first calculate the incremental Green-Lagrange strain from which the incremental second Piola-Kirchhoff stress tensor can be obtained, and secondly, perform the complex stress transformation as described in proceeding section. All variables in (29) are with respect to the global coordinate system.

To apply the corotational procedure, it is convenient to transform equation (29) into local convected coordinate system, as

$$\tilde{\mathbf{f}}_{n+1}^{\text{int}(i)} = \int_{\tilde{\Omega}_{n+1}^{(i)}} \tilde{\mathbf{B}}^{(i)T} \tilde{\boldsymbol{\sigma}}_{n+1}^{(i)} d\tilde{\Omega} \quad (30)$$

where the tilde indicates quantities measured in the local convected coordinate system.  $\tilde{\mathbf{B}}^{(i)}$  represents the strain-displacement matrix in the local convected coordinate system in configuration  $\tilde{\Omega}_{n+1}^{(i)}$ .

The Cauchy stress tensor in the latest obtained configuration can be calculated through the stress transformation in local convected coordinate system as follows

$$J \tilde{\boldsymbol{\sigma}} = \tilde{\boldsymbol{\tau}} = \tilde{\mathbf{F}} \tilde{\mathbf{S}} \tilde{\mathbf{F}}^T \quad (31)$$

$$\Rightarrow \tilde{\boldsymbol{\sigma}} = \frac{1}{J} \tilde{\mathbf{F}} \tilde{\mathbf{S}} \tilde{\mathbf{F}}^T \quad (32)$$

Consequently, stress update in the current configuration can be expressed as

$$\tilde{\boldsymbol{\sigma}}_{n+1} = \tilde{\boldsymbol{\sigma}}_n + \frac{1}{J} \tilde{\mathbf{F}} \Delta \tilde{\mathbf{S}} \tilde{\mathbf{F}}^T \quad (33)$$

Based on the first assumption where the changes on element shapes are assumed to be negligible, the deformation gradient matrix in local convected coordinate system must be

close to an identity matrix and the change in mass density is also negligible, we have  $\rho_o = \rho_t$  for  $J = 1$  and the deformation gradient

$$\tilde{\mathbf{F}}_{iI} = \frac{\partial \tilde{x}_i}{\partial \tilde{X}_I} = \begin{cases} 1 & i = I \\ 0 & i \neq I \end{cases} \quad (34)$$

Substituting (34) into (33), we get further approximation

$$\begin{aligned} \tilde{\boldsymbol{\sigma}}_{n+1} &= \tilde{\boldsymbol{\sigma}}_n + \Delta \tilde{\mathbf{S}} \\ &= \tilde{\boldsymbol{\sigma}}_n + \tilde{\mathbf{C}} : \Delta \tilde{\mathbf{E}}^l \end{aligned} \quad (35)$$

where because of the small strain assumption in the co-rotational framework, we drop the nonlinear term in the Green Lagrange strain tensor and are left with the linear strain tensor.

Consequently,

$$\begin{aligned} \tilde{\boldsymbol{\sigma}}_{n+1}^{(i+1)} &= \tilde{\boldsymbol{\sigma}}_n^{(i)} + \tilde{\mathbf{C}} : \Delta \tilde{\mathbf{E}}^{l(i)} \\ &= \tilde{\boldsymbol{\sigma}}_n^{(i)} + \tilde{\mathbf{C}} : \frac{1}{2} (\nabla \tilde{\mathbf{u}} + \nabla \tilde{\mathbf{u}}^T)_{n+1}^{(i)} \\ &= \tilde{\boldsymbol{\sigma}}_n^{(i)} + \tilde{\mathbf{C}} : \tilde{\mathbf{B}}_{n+1}^{(i)} \tilde{\mathbf{d}}_{n+1}^{(i)} \\ &= \tilde{\boldsymbol{\sigma}}_n^{(i)} + \tilde{\mathbf{C}} : \tilde{\mathbf{B}}_{n+1}^{(i)} \mathbf{I}^T \mathbf{d}_{n+1}^{(i)} \end{aligned} \quad (36)$$

where we have used the transformation relation between the nodal degrees of freedom in the global and the local convected coordinate systems. Once the internal force vector is obtained in local convected coordinate system, a simple coordinate transformation can be performed to obtain the internal force vector in global coordinate system as:

$$\mathbf{f}_{n+1}^{\text{int}(i)} = \mathbf{I}^T \tilde{\mathbf{f}}_{n+1}^{\text{int}(i)} \quad (37)$$

where the transformation matrix is obtained as

$$\phi(\mathbf{I}) = \begin{bmatrix} l_1^2 & m_1^2 & n_1^2 & l_1 m_1 & m_1 n_1 & n_1 l_1 \\ l_2^2 & m_2^2 & n_2^2 & l_2 m_2 & m_2 n_2 & n_2 l_2 \\ l_3^2 & m_3^2 & n_3^2 & l_3 m_3 & m_3 n_3 & n_3 l_3 \\ 2l_1 l_2 & 2m_1 m_2 & 2n_1 n_2 & l_1 m_2 + l_2 m_1 & m_1 n_2 + m_2 n_1 & n_1 l_2 + n_2 l_1 \\ 2l_2 l_3 & 2m_2 m_3 & 2n_2 n_3 & l_2 m_3 + l_3 m_2 & m_2 n_3 + m_3 n_2 & n_2 l_3 + n_3 l_2 \\ 2l_3 l_1 & 2m_3 m_1 & 2n_3 n_1 & l_3 m_1 + l_1 m_3 & m_3 n_1 + m_1 n_3 & n_3 l_1 + n_1 l_3 \end{bmatrix} \quad (38)$$

and

$$\begin{aligned}l_1 &= \cos(\mathbf{i}, \mathbf{e}_1) & m_1 &= \cos(\mathbf{j}, \mathbf{e}_1) & n_1 &= \cos(\mathbf{k}, \mathbf{e}_1) \\l_2 &= \cos(\mathbf{i}, \mathbf{e}_2) & m_2 &= \cos(\mathbf{j}, \mathbf{e}_2) & n_2 &= \cos(\mathbf{k}, \mathbf{e}_2) \\l_3 &= \cos(\mathbf{i}, \mathbf{e}_3) & m_3 &= \cos(\mathbf{j}, \mathbf{e}_3) & n_3 &= \cos(\mathbf{k}, \mathbf{e}_3)\end{aligned}$$

The relation between the Cauchy stress tensor in the global and the local convected coordinate system is expressed through the standard transformation matrix as

$$\tilde{\boldsymbol{\sigma}}_{n+1}^{(i)} = \boldsymbol{\phi}^T(\mathbf{E}) \boldsymbol{\sigma}_{n+1}^{(i)} \quad (39)$$

*Remark:* The above treatment to the geometric nonlinearities is element-independent and applicable to all finite elements. However, the definition of the local convected coordinate system is still element-dependent and special care has to be exercised to obtain a better numerical performance. Another element-dependent step is the modification of nodal triads after each iteration. The formulations must be consistent with the kinematic relations employed in the element.

### 3. STABILIZATION TECHNIQUES FOR UNDERINTEGRATED

#### NONLINEAR SHELL ELEMENTS

##### 3.1 Introduction

In large-scale finite element analyses, a significant number of elements and large computer memory are required to obtain the detailed information for engineering design or process control. When these analyses are explicit, computational costs are mostly determined by the efficiency of the elements, especially for non-linear problems. In the past, full quadrature and selective reduced integration, were extensively used in the finite element analyses. Full quadrature ensures the stability and convergence of solutions. However, it is very expensive owing to the requirement of many computational operations for evaluating the element stiffness matrices and the internal force vectors and it also lead to volumetric locking and transverse shear locking in thin structure bending and incompressible problems. A remedy for this is to use the selective reduced integration in which the full quadrature and reduced quadrature are applied to different terms to form the element stiffness matrix as proposed by Malkus and Hughes [14] and Nagtegaal *et al.* [15], among others. However, it is as costly as full quadrature.

Perhaps, the most efficient elements are the one-point-quadrature elements with hourglass control developed by Flanagan and Belytschko [16], Belytschko [17] and Belytschko *et al.* [18]. The mesh instability associated with the underintegrated elements is controlled by adding a stabilization to the one-point-quadrature element. The stabilization terms are developed to ensure the consistency of the finite element equations and its magnitude is controlled by a user input stabilization parameter. Liu and Belytschko [19] also developed a one-point-quadrature element for heat conduction problems. In this work, the stabilization parameter is determined by solving an eigenvalue problem. In Belytschko *et al.* [20] the Hu-Washizu variational principle is used to examine the magnitude of the stabilization parameters. More recently, an assumed strain stabilization of the four-node quadrilateral element and the eight-

node hexahedral element with one-point quadrature, where the stabilization parameters are not required, was proposed by Belytschko and Bindeman [20,21].

An alternative approach for hourglass control is proposed by Liu *et al.* [22] in which the resulting stabilization matrix requires no stabilization parameter. It is shown that the stabilization vector  $\gamma$  can be obtained simply by taking the partial derivatives of the generalized strain vector with respect to the natural coordinates. The strain vector is therefore approximated by the combination of a constant part and other parts involving strain derivatives. However, shear-related locking phenomena are not taken into consideration and no three dimensional result is reported in their study. Belytschko [18] established an hourglass control procedure by expanding the stress in a Taylor series about the element center. It is found that the hourglass control is suppressed by the retention of the first and second derivatives terms in the expansion. The detailed derivation of element matrices and numerical examples are, however, only for two dimensional problems.

In this work a three-dimensional underintegrated element based on the procedures similar to that proposed by Liu *et al.* [22] are developed. Emphasis is placed on avoiding of locking and the removal of spurious singular modes. This element is applicable to plate and shell bending problems, and more importantly it is suitable for extension to elasto-plasticity. Section 3.2 presents the synopsis of the underintegrated four-node quadrilateral elements with hourglass control as developed by Belytschko *et al.*. The three-dimensional element suitable to bulk deformation and plate/shell structural analyses is developed in Section 3.3.

### 3.2 Four-node quadrilateral element

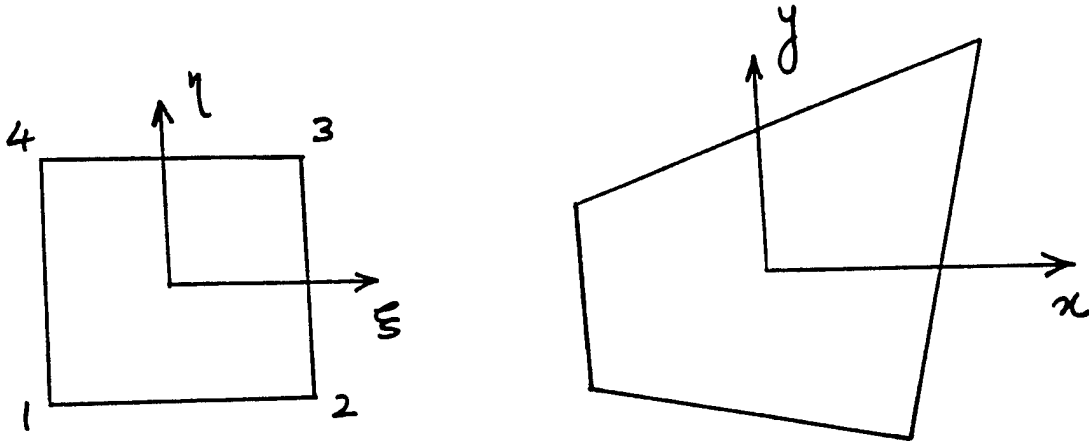


Fig. 1. Physical and reference configurations.

Let us consider a four-node quadrilateral element as shown in Figure 1. The configuration of the element is a bi-unit square in the natural coordinate system  $(\xi, \eta)$ . The spatial coordinates  $x$  and the velocity component  $v$  in the element are approximated by linear combinations of nodal values and the element shape functions.

The gradient submatrix is given by

$$B_a = \begin{bmatrix} N_{a,x} \\ N_{a,y} \end{bmatrix} \quad (40)$$

which can be evaluated at the element center as

$$B_a(0) = \begin{bmatrix} N_{a,x}(0) \\ N_{a,y}(0) \end{bmatrix} = \begin{bmatrix} b_{1a} \\ b_{2a} \end{bmatrix} \quad (41)$$

where

$$b_1 = \{b_{1a}\} = \frac{1}{2A} [y_{24}, y_{31}, y_{42}, y_{13}]^T \quad (42)$$

$$b_2 = \{b_{2a}\} = \frac{1}{2A} [x_{42}, x_{13}, x_{24}, x_{31}]^T \quad (43)$$

$$x_{IJ} = x_I - x_J \quad (44)$$

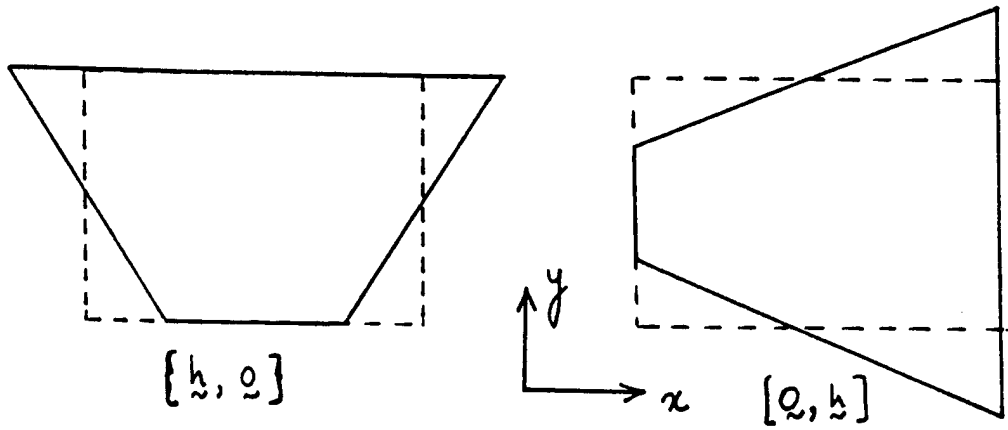


Fig. 2. Bending Modes.

$$y_{IJ} = y_I - y_J \quad (45)$$

$$A = \frac{1}{2}(x_{31} y_{42} + x_{24} y_{31}) \quad (46)$$

and  $I$  and  $J$  designate the node numbers.

For the purpose of identifying the deformation modes of element, let us define column vectors

$$\mathbf{s} = [1, 1, 1, 1]^T \quad (47)$$

$$\mathbf{x} = \mathbf{x}_1 = [x_1, x_2, x_3, x_4]^T \quad (48)$$

$$\mathbf{y} = \mathbf{x}_2 = [y_1, y_2, y_3, y_4]^T \quad (49)$$

$$\mathbf{h} = [1, -1, 1, -1]^T \quad (50)$$

$$\boldsymbol{\xi} = [-1, 1, 1, -1]^T \quad (51)$$

$$\boldsymbol{\eta} = [-1, -1, 1, 1]^T \quad (52)$$

where  $\mathbf{x}$  and  $\mathbf{y}$  are the element nodal coordinates of the physical space;  $\boldsymbol{\xi}$  and  $\boldsymbol{\eta}$  are element nodal coordinates of the biunit square; and  $\mathbf{h}$  is the hourglass vector. In Figure 2, we show two bending modes:  $\{\mathbf{h}, \mathbf{0}\}$  and  $\{\mathbf{0}, \mathbf{h}\}$  which are the deformation mode associated with no energy in the one-point quadrature element but resulting in a non-constant strain in the element.

The strain rate  $\dot{\epsilon}$  is approximated by expanding it in a Taylor series about the element center up to linear terms:

$$\dot{\epsilon}(\xi, \eta) = \dot{\epsilon}(\mathbf{0}) + \dot{\epsilon}_{,\xi}(\mathbf{0})\xi + \dot{\epsilon}_{,\eta}(\mathbf{0})\eta \quad (53)$$

or

$$\dot{\epsilon} = \sum_{a=1}^{n_{en}} \bar{\mathbf{B}}_a(\xi, \eta) \mathbf{v}_a \quad (54)$$

where

$$\bar{\mathbf{B}}_a(\xi, \eta) = \mathbf{B}_a(\mathbf{0}) + \mathbf{B}_{a,\xi}(\mathbf{0})\xi + \mathbf{B}_{a,\eta}(\mathbf{0})\eta \quad (55)$$

The first term on the right hand side of equation (53) is the constant strain rate evaluated at the quadrature point,  $\mathbf{0}$ , and the other terms are linear strain rate terms.

After some algebra, the explicit expressions of the first derivatives of  $\mathbf{B}_a(\mathbf{0})$  with respect to natural coordinates,  $\mathbf{B}_{a,\xi}(\mathbf{0})$  and  $\mathbf{B}_{a,\eta}(\mathbf{0})$ , can be shown to be

$$\mathbf{B}_{a,\xi}(\mathbf{0}) = \begin{bmatrix} b_{1,\xi a} \\ b_{2,\xi a} \end{bmatrix} \quad (56)$$

$$\mathbf{B}_{a,\eta}(\mathbf{0}) = \begin{bmatrix} b_{1,\eta a} \\ b_{2,\eta a} \end{bmatrix} \quad (57)$$

where

$$\mathbf{b}_{1,\xi} = \{b_{1,\xi a}\} = a_{12}\boldsymbol{\gamma} \quad (58)$$

$$\mathbf{b}_{2,\xi} = \{b_{2,\xi a}\} = a_{11}\boldsymbol{\gamma} \quad (59)$$

$$\mathbf{b}_{1,\eta} = \{b_{1,\eta a}\} = a_{22}\boldsymbol{\gamma} \quad (60)$$

$$\mathbf{b}_{2,\eta} = \{b_{2,\eta a}\} = a_{21}\boldsymbol{\gamma} \quad (61)$$

where

$$a_{11} = \frac{\boldsymbol{\xi}^T \mathbf{x}}{4A} \quad (62)$$

$$a_{12} = \frac{-\boldsymbol{\xi}^T \mathbf{y}}{4A} \quad (63)$$

$$a_{21} = \frac{-\boldsymbol{\eta}^T \mathbf{x}}{4A} \quad (64)$$

$$a_{22} = \frac{\boldsymbol{\eta}^T \mathbf{y}}{4A} \quad (65)$$

The  $\boldsymbol{\gamma}$  in equations (58)–(65) is the stabilization vector which spans the improper null-space of  $\mathbf{B}(\mathbf{0})$ . It is given by

$$\boldsymbol{\gamma} = \mathbf{h} - (\mathbf{h}^T \mathbf{x}_i) \mathbf{b}_i \quad (66)$$

where  $i$  is the summation index from 1 to 2.  $\boldsymbol{\gamma}$  is orthogonal to the linear velocity field and provides the proper stabilization for the element. Belytschko and co-workers [17,20] derived these vectors from the requirements of consistency of the finite element equations in the sense that the gradients of the linear fields were evaluated correctly.

To alleviate volumetric locking, we employ the ideas underlying selective/reduced integration.  $\bar{\mathbf{B}}_a(\xi, \eta)$  is decomposed into two parts as

$$\bar{\mathbf{B}}_a(\xi, \eta) = \bar{\mathbf{B}}_a^{\text{dil}}(\mathbf{0}) + \bar{\mathbf{B}}_a^{\text{dev}}(\xi, \eta) \quad (67)$$

where  $\bar{\mathbf{B}}_a^{\text{dil}}$  are the gradient submatrices due to the dilatational part of  $\bar{\mathbf{B}}_a$ ; and  $\bar{\mathbf{B}}_a^{\text{dev}}$  are the gradient submatrices due to the deviatoric part of  $\bar{\mathbf{B}}_a$ . Here, the dilatational part of the gradient matrix has been underintegrated and evaluated only at one quadrature point,  $\mathbf{0}$ , to alleviate the volumetric locking. Expanding  $\bar{\mathbf{B}}_a^{\text{dev}}$  about the element center via equation (55), equation (67) can be written as

$$\bar{\mathbf{B}}_a(\xi, \eta) = \mathbf{B}_a(\mathbf{0}) + \mathbf{B}_{a,\xi}^{\text{dev}}(\mathbf{0})\xi + \mathbf{B}_{a,\eta}^{\text{dev}}(\mathbf{0})\eta \quad (68)$$

where  $\mathbf{B}_a(\mathbf{0})$  are the one-point-quadrature gradient submatrices contributed from both the dilatational and deviatoric parts. The other terms on the right-hand side of above equation are the gradient submatrices corresponding to non-constant deviatoric strain rates. It is noted that the resulting element using the gradient matrices as in equation (67) or (68) exhibits no hourglass mode if the element internal virtual work is evaluated by using a multiple-quadrature-point integration.

The element developed so far is not suitable for the thin beam or plate analysis owing to the so called shear locking for the bending modes. It is well known that the reduced integration on shear strain rates in the global coordinate system is not physically correct when the referential coordinate system is not aligned with the global one. Hence, a co-rotational coordinate system which rotates with the element is used for the derivation that follows. To alleviate the shear locking, the gradient submatrices for the general 2-D element are interpolated in the following form:

$$\bar{\mathbf{B}}_{xx}(\xi, \eta) = \mathbf{B}_{xx}(\mathbf{0}) + \mathbf{B}_{xx,\xi}^{\text{dev}}(\mathbf{0})\xi + \mathbf{B}_{xx,\eta}^{\text{dev}}(\mathbf{0})\eta \quad (69)$$

$$\bar{\mathbf{B}}_{yy}(\xi, \eta) = \mathbf{B}_{yy}(\mathbf{0}) + \mathbf{B}_{yy,\xi}^{\text{dev}}(\mathbf{0})\xi + \mathbf{B}_{yy,\eta}^{\text{dev}}(\mathbf{0})\eta \quad (70)$$

$$\bar{\mathbf{B}}_{xy}(\xi, \eta) = \mathbf{B}_{xy}(\mathbf{0}) \quad (71)$$

$$\bar{\mathbf{B}}_{zz}(\xi, \eta) = \mathbf{B}_{zz,\xi}^{\text{dev}}(\mathbf{0})\xi + \mathbf{B}_{zz,\eta}^{\text{dev}}(\mathbf{0})\eta \quad (72)$$

where

$$\begin{bmatrix} \mathbf{B}_{xx}(\mathbf{0}) \\ \mathbf{B}_{yy}(\mathbf{0}) \\ \mathbf{B}_{xy}(\mathbf{0}) \\ \mathbf{B}_{zz}(\mathbf{0}) \end{bmatrix} = \begin{bmatrix} \mathbf{b}_1^T & \mathbf{0} \\ \mathbf{0} & \mathbf{b}_2^T \\ \mathbf{b}_2^T & \mathbf{b}_1^T \\ \mathbf{0} & \mathbf{0} \end{bmatrix} \quad (73)$$

$$\begin{bmatrix} \mathbf{B}_{xx,\xi}^{\text{dev}}(\mathbf{0}) \\ \mathbf{B}_{yy,\xi}^{\text{dev}}(\mathbf{0}) \\ \mathbf{B}_{zz,\xi}^{\text{dev}}(\mathbf{0}) \end{bmatrix} = \begin{bmatrix} \frac{2}{3} a_{12} \gamma^T & -\frac{1}{3} a_{11} \gamma^T \\ -\frac{1}{3} a_{12} \gamma^T & \frac{2}{3} a_{11} \gamma^T \\ -\frac{1}{3} a_{12} \gamma^T & -\frac{1}{3} a_{11} \gamma^T \end{bmatrix} \quad (74)$$

$$\begin{bmatrix} \mathbf{B}_{xx,\eta}^{\text{dev}}(\mathbf{0}) \\ \mathbf{B}_{yy,\eta}^{\text{dev}}(\mathbf{0}) \\ \mathbf{B}_{zz,\eta}^{\text{dev}}(\mathbf{0}) \end{bmatrix} = \begin{bmatrix} \frac{2}{3} a_{22} \gamma^T & -\frac{1}{3} a_{21} \gamma^T \\ -\frac{1}{3} a_{22} \gamma^T & \frac{2}{3} a_{21} \gamma^T \\ -\frac{1}{3} a_{22} \gamma^T & -\frac{1}{3} a_{21} \gamma^T \end{bmatrix} \quad (75)$$

$\bar{\mathbf{B}}_{xx}$ ,  $\bar{\mathbf{B}}_{yy}$ ,  $\bar{\mathbf{B}}_{xy}$  and  $\bar{\mathbf{B}}_{zz}$  are the gradient submatrices corresponding to the shear strain rates  $\dot{\epsilon}_{xx}$ ,  $\dot{\epsilon}_{yy}$ ,  $\dot{\epsilon}_{xy}$  and  $\dot{\epsilon}_{zz}$ , respectively. Here, only the constant term is used for the shear strain

rate component such that the mode causing locking is removed. The normal strain rates keep all non-constant terms given in equation (68).

Although one-point quadrature with hourglass control can be applied to the element developed herein, it might be not accurate enough for more advanced nonlinear constitutive models. Hence we follow Liu *et al.* [22] to use two-point quadrature where the element internal force vector is evaluated at the two integration points located as follows:

$$\text{Point 1 : } \left( +\frac{1}{\sqrt{3}}, +\frac{1}{\sqrt{3}} \right)$$

$$\text{Point 2 : } \left( -\frac{1}{\sqrt{3}}, -\frac{1}{\sqrt{3}} \right)$$

This two-point quadrature element exhibits no hourglass mode and is rank sufficient. By assuming that the Jacobian is a constant, one half of the area, the element internal force vector can be integrated as follows:

$$\mathbf{f}^{int} = \sum_{i=1}^2 \frac{A}{2} \bar{\mathbf{B}}^T(\xi_i) \boldsymbol{\tau}(\xi_i) \quad (76)$$

where  $\xi_i$  denotes the natural coordinates of the integration point  $i$  and  $A$  is the element area.

The element internal force vector can be further rearranged as

$$\mathbf{f}^{int} = \mathbf{f}_2^{int} + \mathbf{f}_{stab}^{int} \quad (77)$$

where  $\mathbf{f}_2^{int}$  and  $\mathbf{f}_{stab}^{int}$  are the internal force vector resulting from one-point quadrature and stabilization, respectively. They are given by

$$\mathbf{f}_2^{int} = \frac{A}{2} \begin{bmatrix} \tilde{\tau}_{11} \mathbf{b}_1 + \tilde{\tau}_{12} \mathbf{b}_2 \\ \tilde{\tau}_{12} \mathbf{b}_1 + \tilde{\tau}_{22} \mathbf{b}_2 \end{bmatrix} \quad (78)$$

and

$$\mathbf{f}_{stab}^{int} = \frac{\sqrt{3}A}{18} \begin{bmatrix} (a_{12} + a_{22}) \times (2\hat{\tau}_{11} - \hat{\tau}_{22} - \hat{\tau}_{33}) \boldsymbol{\gamma} \\ (a_{11} + a_{21}) \times (-\hat{\tau}_{11} + 2\hat{\tau}_{22} - \hat{\tau}_{33}) \boldsymbol{\gamma} \end{bmatrix} \quad (79)$$

where  $a_{ij}$  are given in equations (62)–(65) and

$$\tilde{\tau}_{ij} = \tau_{ij}(\xi_1) + \tau_{ij}(\xi_2) \quad (80)$$

$$\hat{\tau}_{ij} = \tau_{ij}(\xi_1) - \tau_{ij}(\xi_2) \quad (81)$$

### 3.3 Eight-node Hexahedral element

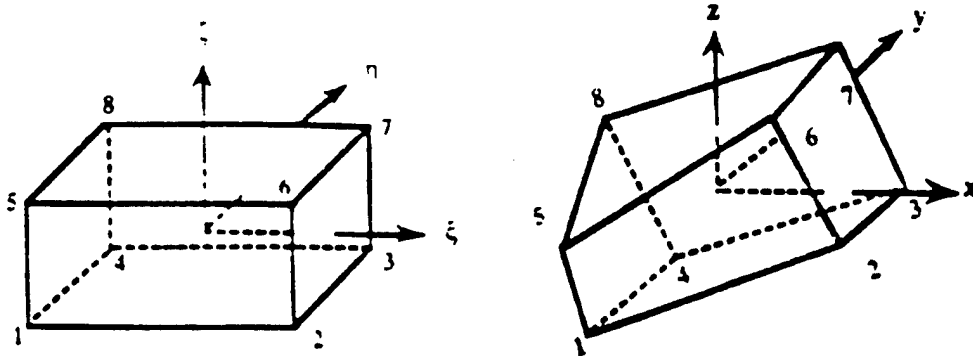


Fig. 3. Physical and reference configurations for 8-node element.

Let us consider an eight-node hexahedral element as shown in Figure 3. The spatial coordinates and velocity in the element are approximated by linear combination of nodal values and shape functions as follows:

$$x_i = \sum_{a=1}^{n_{en}} N_a(\xi, \eta, \zeta) x_{ia} \quad (n_{en} = 8) \quad (82)$$

$$v_i = \sum_{a=1}^{n_{en}} N_a(\xi, \eta, \zeta) v_{ia} \quad (83)$$

$$N_a(\xi, \eta, \zeta) = \frac{1}{8} (1 + \xi_a \xi) (1 + \eta_a \eta) (1 + \zeta_a \zeta) \quad (84)$$

where the subscripts  $i$  and  $a$  denote coordinate component ranging from one to three and the element node number, ranging from one to eight, respectively.

For the purpose of identifying the deformation modes of the element, let us define the gradient submatrices  $B_a(\mathbf{0})$  and other column vectors as

$$B_a(\mathbf{0}) = \begin{bmatrix} N_{a,x}(\mathbf{0}) \\ N_{a,y}(\mathbf{0}) \\ N_{a,z}(\mathbf{0}) \end{bmatrix} = \begin{bmatrix} b_{1a} \\ b_{2a} \\ b_{3a} \end{bmatrix} \quad (85)$$

$$\mathbf{s}^T = [1, 1, 1, 1, 1, 1, 1, 1] \quad (86)$$

$$\mathbf{x}^T = [x_1, x_2, x_3, x_4, x_5, x_6, x_7, x_8] \quad (87)$$

$$\mathbf{y}^T = [y_1, y_2, y_3, y_4, y_5, y_6, y_7, y_8] \quad (88)$$

$$\mathbf{z}^T = [z_1, z_2, z_3, z_4, z_5, z_6, z_7, z_8] \quad (89)$$

$$\mathbf{h}_1^T = [1, -1, 1, -1, 1, -1, 1, -1] \quad (90)$$

$$\mathbf{h}_2^T = [1, -1, -1, 1, -1, 1, 1, -1] \quad (91)$$

$$\mathbf{h}_3^T = [1, 1, -1, -1, -1, -1, 1, 1] \quad (92)$$

$$\mathbf{h}_4^T = [-1, 1, -1, 1, 1, -1, 1, -1] \quad (93)$$

$$\boldsymbol{\xi}^T = [-1, 1, 1, -1, -1, 1, 1, -1] \quad (94)$$

$$\boldsymbol{\eta}^T = [-1, -1, 1, 1, -1, -1, 1, 1] \quad (95)$$

$$\boldsymbol{\zeta}^T = [-1, -1, -1, -1, 1, 1, 1, 1] \quad (96)$$

where  $\mathbf{x}$ ,  $\mathbf{y}$  and  $\mathbf{z}$  are the nodal coordinates and  $\mathbf{h}_1$  is the  $\xi\eta$ -hourglass vector,  $\mathbf{h}_2$  the  $\xi\zeta$ -hourglass vector,  $\mathbf{h}_3$  the  $\eta\zeta$ -hourglass vector and  $\mathbf{h}_4$  the  $\xi\eta\zeta$ -hourglass vector.

The Jacobian matrix evaluated in the center of an element can be shown to be

$$\mathbf{J}(\mathbf{0}) = [J_{ij}] = \frac{1}{8} \begin{bmatrix} \boldsymbol{\xi}^T \mathbf{x} & \boldsymbol{\xi}^T \mathbf{y} & \boldsymbol{\xi}^T \mathbf{z} \\ \boldsymbol{\eta}^T \mathbf{x} & \boldsymbol{\eta}^T \mathbf{y} & \boldsymbol{\eta}^T \mathbf{z} \\ \boldsymbol{\zeta}^T \mathbf{x} & \boldsymbol{\zeta}^T \mathbf{y} & \boldsymbol{\zeta}^T \mathbf{z} \end{bmatrix} \quad i, j = 1, 2, 3 \quad (97)$$

The determinant of the Jacobian matrix is denoted by  $J_0$  and the inverse of  $J(\mathbf{0})$  is given by  $D$ :

$$D = [D_{ij}] = J^{-1}(\mathbf{0}) \quad (98)$$

The gradient vectors  $\mathbf{b}_1, \mathbf{b}_2$  and  $\mathbf{b}_3$  (which are evaluated at  $\mathbf{0}$ ) in equation (85), can be shown to be

$$\mathbf{b}_1 = \{b_{1a}\} = \frac{1}{8} [D_{11}\xi + D_{12}\eta + D_{13}\zeta] \quad (99)$$

$$\mathbf{b}_2 = \{b_{2a}\} = \frac{1}{8} [D_{21}\xi + D_{22}\eta + D_{23}\zeta] \quad (100)$$

$$\mathbf{b}_3 = \{b_{3a}\} = \frac{1}{8} [D_{31}\xi + D_{32}\eta + D_{33}\zeta] \quad (101)$$

Expanding strain rate  $\dot{\epsilon}$  in Taylor series about the element center

$$\begin{aligned} \dot{\epsilon}(\xi, \eta, \zeta) = & \dot{\epsilon}(\mathbf{0}) + \dot{\epsilon}_{,\xi}(\mathbf{0})\xi + \dot{\epsilon}_{,\eta}(\mathbf{0})\eta + \dot{\epsilon}_{,\zeta}(\mathbf{0})\zeta \\ & + \dot{\epsilon}_{,\xi\eta}(\mathbf{0})\xi\eta + \dot{\epsilon}_{,\eta\zeta}(\mathbf{0})\eta\zeta + \dot{\epsilon}_{,\zeta\xi}(\mathbf{0})\zeta\xi \end{aligned} \quad (102)$$

or

$$\dot{\epsilon} = \sum_{a=1}^{n_{en}} \bar{B}_a(\xi, \eta, \zeta) \mathbf{v}_a \quad (103)$$

where

$$\begin{aligned} \bar{B}_a(\xi, \eta, \zeta) = & B_a(\mathbf{0}) + B_{a,\xi}(\mathbf{0})\xi + B_{a,\eta}(\mathbf{0})\eta + B_{a,\zeta}(\mathbf{0})\zeta \\ & + B_{a,\xi\eta}(\mathbf{0})\xi\eta + B_{a,\eta\zeta}(\mathbf{0})\eta\zeta + B_{a,\zeta\xi}(\mathbf{0})\zeta\xi \end{aligned} \quad (104)$$

The first term on the right hand side of the equation (102) or (104) is the constant strain rates evaluated at the quadrature point,  $\mathbf{0}$ , and the remaining terms are the linear and bilinear strain rate terms. After some tedious algebra, it can be shown that the first and second derivatives of  $B_a(\mathbf{0})$  with respect to natural coordinates are given by

$$\mathbf{b}_{1,\xi} = \{N_{a,x\xi}\} = \frac{1}{8} [D_{12}\gamma_1 + D_{13}\gamma_2] \quad (105)$$

$$\mathbf{b}_{2,\xi} = \{N_{a,y\xi}\} = \frac{1}{8} [D_{22}\gamma_1 + D_{23}\gamma_2] \quad (106)$$

$$\mathbf{b}_{3,\xi} = \{N_{a,z\xi}\} = \frac{1}{8} [D_{32}\gamma_1 + D_{33}\gamma_2] \quad (107)$$

$$\mathbf{b}_{1,\eta} = \{N_{a,x\eta}\} = \frac{1}{8} [D_{11}\gamma_1 + D_{13}\gamma_3] \quad (108)$$

$$\mathbf{b}_{2,\eta} = \{N_{a,y\eta}\} = \frac{1}{8} [D_{21}\gamma_1 + D_{23}\gamma_3] \quad (109)$$

$$\mathbf{b}_{3,\eta} = \{N_{a,z\eta}\} = \frac{1}{8} [D_{31}\gamma_1 + D_{33}\gamma_3] \quad (110)$$

$$\mathbf{b}_{1,\zeta} = \{N_{a,x\zeta}\} = \frac{1}{8} [D_{11}\gamma_2 + D_{12}\gamma_3] \quad (111)$$

$$\mathbf{b}_{2,\zeta} = \{N_{a,y\zeta}\} = \frac{1}{8} [D_{21}\gamma_2 + D_{22}\gamma_3] \quad (112)$$

$$\mathbf{b}_{3,\zeta} = \{N_{a,z\zeta}\} = \frac{1}{8} [D_{31}\gamma_2 + D_{32}\gamma_3] \quad (113)$$

$$\mathbf{b}_{1,\xi\eta} = \{N_{a,x\xi\eta}\} = \frac{1}{8} [D_{13}\gamma_4 - (\mathbf{p}_1^T \mathbf{x}_i) \mathbf{b}_{i,\xi} - (\mathbf{r}_1^T \mathbf{x}_i) \mathbf{b}_{i,\eta}] \quad (114)$$

$$\mathbf{b}_{2,\xi\eta} = \{N_{a,y\xi\eta}\} = \frac{1}{8} [D_{23}\gamma_4 - (\mathbf{p}_2^T \mathbf{x}_i) \mathbf{b}_{i,\xi} - (\mathbf{r}_2^T \mathbf{x}_i) \mathbf{b}_{i,\eta}] \quad (115)$$

$$\mathbf{b}_{3,\xi\eta} = \{N_{a,z\xi\eta}\} = \frac{1}{8} [D_{33}\gamma_4 - (\mathbf{p}_3^T \mathbf{x}_i) \mathbf{b}_{i,\xi} - (\mathbf{r}_3^T \mathbf{x}_i) \mathbf{b}_{i,\eta}] \quad (116)$$

$$\mathbf{b}_{1,\eta\zeta} = \{N_{a,x\eta\zeta}\} = \frac{1}{8} [D_{11}\gamma_4 - (\mathbf{q}_1^T \mathbf{x}_i) \mathbf{b}_{i,\eta} - (\mathbf{p}_1^T \mathbf{x}_i) \mathbf{b}_{i,\zeta}] \quad (117)$$

$$\mathbf{b}_{2,\eta\zeta} = \{N_{a,y\eta\zeta}\} = \frac{1}{8} [D_{21}\gamma_4 - (\mathbf{q}_2^T \mathbf{x}_i) \mathbf{b}_{i,\eta} - (\mathbf{p}_2^T \mathbf{x}_i) \mathbf{b}_{i,\zeta}] \quad (118)$$

$$\mathbf{b}_{3,\eta\zeta} = \{N_{a,z\eta\zeta}\} = \frac{1}{8} [D_{31}\gamma_4 - (\mathbf{q}_3^T \mathbf{x}_i) \mathbf{b}_{i,\eta} - (\mathbf{p}_3^T \mathbf{x}_i) \mathbf{b}_{i,\zeta}] \quad (119)$$

$$\mathbf{b}_{1,\xi\zeta} = \{N_{a,x\xi\zeta}\} = \frac{1}{8} [D_{12}\gamma_4 - (\mathbf{q}_1^T \mathbf{x}_i) \mathbf{b}_{i,\xi} - (\mathbf{r}_1^T \mathbf{x}_i) \mathbf{b}_{i,\zeta}] \quad (120)$$

$$\mathbf{b}_{2,\xi\zeta} = \{N_{a,y\xi\zeta}\} = \frac{1}{8} [D_{22}\gamma_4 - (\mathbf{q}_2^T \mathbf{x}_i) \mathbf{b}_{i,\xi} - (\mathbf{r}_2^T \mathbf{x}_i) \mathbf{b}_{i,\zeta}] \quad (121)$$

$$\mathbf{b}_{3,\xi\zeta} = \{N_{a,z\xi\zeta}\} = \frac{1}{8} [D_{32}\gamma_4 - (\mathbf{q}_3^T \mathbf{x}_i) \mathbf{b}_{i,\xi} - (\mathbf{r}_3^T \mathbf{x}_i) \mathbf{b}_{i,\zeta}] \quad (122)$$

where

$$\mathbf{p}_i = D_{i1}\mathbf{h}_1 + D_{i3}\mathbf{h}_3 \quad (123)$$

$$\mathbf{q}_i = D_{i1}\mathbf{h}_2 + D_{i2}\mathbf{h}_3 \quad (124)$$

$$\mathbf{r}_i = D_{i2}\mathbf{h}_1 + D_{i3}\mathbf{h}_2 \quad (125)$$

The  $\gamma_\alpha$  in equations (105)–(122) are the stabilization vectors which span the improper null-space of  $B(\mathbf{0})$ . They are given by

$$\gamma_\alpha = \mathbf{h}_\alpha - (\mathbf{h}_\alpha^T \mathbf{x}_i) \mathbf{b}_i \quad (126)$$

where  $i$  is the summation index from 1 to 3.  $\gamma_\alpha$  is orthogonal to the linear displacement field and provide the proper stabilization for the element.

Similar to the four-node quadrilateral element,  $\bar{B}_a(\xi, \eta, \zeta)$  is decomposed into two parts, dilatational part and the deviatoric part. The dilatational part of gradient matrices are underintegrated and evaluated at only one quadrature point,  $\mathbf{0}$ , to avoid volumetric locking:

$$\bar{B}_a(\xi, \eta, \zeta) = \bar{B}_a^{\text{dil}}(\mathbf{0}) + \bar{B}_a^{\text{dev}}(\xi, \eta, \zeta) \quad (127)$$

Expanding  $\bar{B}_a^{\text{dev}}$  about the element center, equation (126) can be written as

$$\begin{aligned} \bar{B}_a(\xi, \eta, \zeta) = & B_a(\mathbf{0}) + B_{a,\xi}^{\text{dev}}(\mathbf{0})\xi + B_{a,\eta}^{\text{dev}}(\mathbf{0})\eta + B_{a,\zeta}^{\text{dev}}(\mathbf{0})\zeta \\ & + B_{a,\xi\eta}^{\text{dev}}(\mathbf{0})\xi\eta + B_{a,\eta\zeta}^{\text{dev}}(\mathbf{0})\eta\zeta + B_{a,\zeta\xi}^{\text{dev}}(\mathbf{0})\zeta\xi \end{aligned} \quad (128)$$

where  $B_a(\mathbf{0})$  are the one-point-quadrature gradient submatrices contributed from both the dilatational and deviatoric parts. The remaining terms on the right-hand-side of the above equation are the gradient submatrices corresponding to non-constant deviatoric strain rates. It is noted that the element using the gradient matrices as in equation (127) or (128) is properly underintegrated and exhibits no hourglass mode if the element internal energy is evaluated by using the multiple-point quadrature.

The element developed so far is not suitable to plate /shell analysis owing to the shear and membrane locking in thin structures. To remove shear locking, the gradient submatrices, corresponding to the assumed shear strain rates is written in an orthogonal co-rotational coordinate system rotating with the element as

$$\begin{aligned} \bar{B}_{xx}(\xi, \eta, \zeta) = & B_{xx}(\mathbf{0}) + B_{xx,\xi}^{\text{dev}}(\mathbf{0})\xi + B_{xx,\eta}^{\text{dev}}(\mathbf{0})\eta + B_{xx,\zeta}^{\text{dev}}(\mathbf{0})\zeta \\ & + B_{xx,\xi\eta}^{\text{dev}}(\mathbf{0})\xi\eta + B_{xx,\eta\zeta}^{\text{dev}}(\mathbf{0})\eta\zeta + B_{xx,\zeta\xi}^{\text{dev}}(\mathbf{0})\zeta\xi \end{aligned} \quad (129)$$

$$\begin{aligned}\bar{B}_{yy}(\xi, \eta, \zeta) &= B_{yy}(0) + B_{yy,\xi}^{\text{dev}}(0)\xi + B_{yy,\eta}^{\text{dev}}(0)\eta + B_{yy,\zeta}^{\text{dev}}(0)\zeta \\ &\quad + B_{yy,\xi\eta}^{\text{dev}}(0)\xi\eta + B_{yy,\eta\zeta}^{\text{dev}}(0)\eta\zeta + B_{yy,\zeta\xi}^{\text{dev}}(0)\zeta\xi\end{aligned}\quad (130)$$

$$\begin{aligned}\bar{B}_{zz}(\xi, \eta, \zeta) &= B_{zz}(0) + B_{zz,\xi}^{\text{dev}}(0)\xi + B_{zz,\eta}^{\text{dev}}(0)\eta + B_{zz,\zeta}^{\text{dev}}(0)\zeta \\ &\quad + B_{zz,\xi\eta}^{\text{dev}}(0)\xi\eta + B_{zz,\eta\zeta}^{\text{dev}}(0)\eta\zeta + B_{zz,\zeta\xi}^{\text{dev}}(0)\zeta\xi\end{aligned}\quad (131)$$

$$\bar{B}_{xy}(\xi, \eta, \zeta) = B_{xy}(0) + B_{xy,\zeta}^{\text{dev}}(0)\zeta \quad (132)$$

$$\bar{B}_{yz}(\xi, \eta, \zeta) = B_{yz}(0) + B_{yz,\xi}^{\text{dev}}(0)\xi \quad (133)$$

$$\bar{B}_{zx}(\xi, \eta, \zeta) = B_{zx}(0) + B_{zx,\eta}^{\text{dev}}(0)\eta \quad (134)$$

where

$$\begin{bmatrix} B_{xx}(0) \\ B_{yy}(0) \\ B_{zz}(0) \\ B_{xy}(0) \\ B_{yz}(0) \\ B_{zx}(0) \end{bmatrix} = \begin{bmatrix} b_1^T & 0 & 0 \\ 0 & b_2^T & 0 \\ 0 & 0 & b_3^T \\ b_2^T & b_1^T & 0 \\ 0 & b_3^T & b_2^T \\ b_3^T & 0 & b_1^T \end{bmatrix} \quad (135)$$

$$\begin{bmatrix} B_{xx,\xi}^{\text{dev}}(0) \\ B_{yy,\xi}^{\text{dev}}(0) \\ B_{zz,\xi}^{\text{dev}}(0) \\ B_{xy,\xi}^{\text{dev}}(0) \\ B_{yz,\xi}^{\text{dev}}(0) \\ B_{zx,\xi}^{\text{dev}}(0) \end{bmatrix} = \frac{1}{8} \begin{bmatrix} 0 & -\frac{1}{3}D_{22}\gamma_1^T & -\frac{1}{3}D_{33}\gamma_2^T \\ 0 & \frac{2}{3}D_{22}\gamma_1^T & -\frac{1}{3}D_{33}\gamma_2^T \\ 0 & -\frac{1}{3}D_{22}\gamma_1^T & \frac{2}{3}D_{33}\gamma_2^T \\ D_{22}\gamma_1^T & 0 & 0 \\ 0 & D_{33}\gamma_2^T & D_{22}\gamma_1^T \\ D_{33}\gamma_2^T & 0 & 0 \end{bmatrix} \quad (136)$$

$$\begin{bmatrix} B_{xx,\eta}^{\text{dev}}(0) \\ B_{yy,\eta}^{\text{dev}}(0) \\ B_{zz,\eta}^{\text{dev}}(0) \\ B_{xy,\eta}^{\text{dev}}(0) \\ B_{yz,\eta}^{\text{dev}}(0) \\ B_{zx,\eta}^{\text{dev}}(0) \end{bmatrix} = \frac{1}{8} \begin{bmatrix} \frac{2}{3}D_{11}\gamma_1^T & 0 & -\frac{1}{3}D_{33}\gamma_3^T \\ -\frac{1}{3}D_{11}\gamma_1^T & 0 & -\frac{1}{3}D_{33}\gamma_3^T \\ -\frac{1}{3}D_{11}\gamma_1^T & 0 & \frac{2}{3}D_{33}\gamma_3^T \\ 0 & D_{11}\gamma_1^T & 0 \\ 0 & D_{33}\gamma_3^T & 0 \\ D_{33}\gamma_3^T & 0 & D_{11}\gamma_1^T \end{bmatrix} \quad (137)$$

$$\begin{bmatrix} B_{xx,\zeta}^{\text{dev}}(0) \\ B_{yy,\zeta}^{\text{dev}}(0) \\ B_{zz,\zeta}^{\text{dev}}(0) \\ B_{xy,\zeta}^{\text{dev}}(0) \\ B_{yz,\zeta}^{\text{dev}}(0) \\ B_{zx,\zeta}^{\text{dev}}(0) \end{bmatrix} = \frac{1}{8} \begin{bmatrix} \frac{2}{3}D_{11}\gamma_2^T & -\frac{1}{3}D_{22}\gamma_3^T & 0 \\ -\frac{1}{3}D_{11}\gamma_2^T & \frac{2}{3}D_{22}\gamma_3^T & 0 \\ -\frac{1}{3}D_{11}\gamma_2^T & -\frac{1}{3}D_{22}\gamma_3^T & 0 \\ D_{22}\gamma_3^T & D_{11}\gamma_2^T & 0 \\ 0 & 0 & D_{22}\gamma_3^T \\ 0 & 0 & D_{11}\gamma_2^T \end{bmatrix} \quad (138)$$

$$\begin{bmatrix} B_{xx,\xi\eta}^{\text{dev}}(0) \\ B_{yy,\xi\eta}^{\text{dev}}(0) \\ B_{zz,\xi\eta}^{\text{dev}}(0) \\ B_{xy,\xi\eta}^{\text{dev}}(0) \\ B_{yz,\xi\eta}^{\text{dev}}(0) \\ B_{zx,\xi\eta}^{\text{dev}}(0) \end{bmatrix} = \frac{1}{8} \begin{bmatrix} 0 & 0 & -\frac{1}{3}D_{33}\gamma_4^T \\ 0 & 0 & -\frac{1}{3}D_{33}\gamma_4^T \\ 0 & 0 & \frac{2}{3}D_{33}\gamma_4^T \\ 0 & D_{33}\gamma_4^T & 0 \\ 0 & 0 & 0 \\ D_{33}\gamma_4^T & 0 & 0 \end{bmatrix} \quad (139)$$

$$\begin{bmatrix} B_{xx,\eta\zeta}^{\text{dev}}(0) \\ B_{yy,\eta\zeta}^{\text{dev}}(0) \\ B_{zz,\eta\zeta}^{\text{dev}}(0) \\ B_{xy,\eta\zeta}^{\text{dev}}(0) \\ B_{yz,\eta\zeta}^{\text{dev}}(0) \\ B_{zx,\eta\zeta}^{\text{dev}}(0) \end{bmatrix} = \frac{1}{8} \begin{bmatrix} \frac{2}{3}D_{11}\gamma_4^T & 0 & 0 \\ -\frac{1}{3}D_{11}\gamma_4^T & 0 & 0 \\ -\frac{1}{3}D_{11}\gamma_4^T & 0 & 0 \\ 0 & D_{11}\gamma_4^T & 0 \\ 0 & 0 & 0 \\ 0 & 0 & D_{11}\gamma_4^T \end{bmatrix} \quad (140)$$

$$\begin{bmatrix} \mathbf{B}_{xx,\zeta\xi}^{\text{dev}}(\mathbf{0}) \\ \mathbf{B}_{yy,\zeta\xi}^{\text{dev}}(\mathbf{0}) \\ \mathbf{B}_{zz,\zeta\xi}^{\text{dev}}(\mathbf{0}) \\ \mathbf{B}_{xy,\zeta\xi}^{\text{dev}}(\mathbf{0}) \\ \mathbf{B}_{yz,\zeta\xi}^{\text{dev}}(\mathbf{0}) \\ \mathbf{B}_{zx,\zeta\xi}^{\text{dev}}(\mathbf{0}) \end{bmatrix} = \frac{1}{8} \begin{bmatrix} \mathbf{0} & -\frac{1}{3}D_{22}\gamma_4^T & \mathbf{0} \\ \mathbf{0} & \frac{2}{3}D_{22}\gamma_4^T & \mathbf{0} \\ \mathbf{0} & -\frac{1}{3}D_{22}\gamma_4^T & \mathbf{0} \\ D_{22}\gamma_4^T & \mathbf{0} & \mathbf{0} \\ \mathbf{0} & \mathbf{0} & D_{22}\gamma_4^T \\ \mathbf{0} & \mathbf{0} & \mathbf{0} \end{bmatrix} \quad (141)$$

In above equations,  $\bar{\mathbf{B}}_{xx}$ ,  $\bar{\mathbf{B}}_{yy}$ ,  $\bar{\mathbf{B}}_{zz}$ ,  $\bar{\mathbf{B}}_{xy}$ ,  $\bar{\mathbf{B}}_{yz}$  and  $\bar{\mathbf{B}}_{zx}$  are the gradient submatrices corresponding to strain rates  $\dot{\epsilon}_{xx}$ ,  $\dot{\epsilon}_{yy}$ ,  $\dot{\epsilon}_{zz}$ ,  $\dot{\epsilon}_{xy}$ ,  $\dot{\epsilon}_{yz}$  and  $\dot{\epsilon}_{zx}$  respectively. Here, only one non-constant term is used for each shear strain rate component such that the modes causing shear locking are removed. The normal strain rates keep all non-constant terms given in equation (127). In  $\mathbf{B}^{\text{dev}}(\mathbf{0})$ , only those terms corresponding to a parallelepiped element are used for stabilization.

For advanced nonlinear constitutive models in 3-D calculations of large deformation problems, we propose to use a four-point- quadrature scheme instead of one-point quadrature. Following Belytschko *et. al.* [20] the element internal force vector is evaluated at the four integration points located as follows:

$$\text{Point 1 : } \left( +\frac{1}{\sqrt{3}}, +\frac{1}{\sqrt{3}}, +\frac{1}{\sqrt{3}} \right) \quad (142)$$

$$\text{Point 2 : } \left( -\frac{1}{\sqrt{3}}, -\frac{1}{\sqrt{3}}, +\frac{1}{\sqrt{3}} \right) \quad (143)$$

$$\text{Point 3 : } \left( -\frac{1}{\sqrt{3}}, +\frac{1}{\sqrt{3}}, -\frac{1}{\sqrt{3}} \right) \quad (144)$$

$$\text{Point 4 : } \left( +\frac{1}{\sqrt{3}}, -\frac{1}{\sqrt{3}}, -\frac{1}{\sqrt{3}} \right) \quad (145)$$

By assuming that the Jacobian is a constant, one-quarter of the element volume, the element internal force vector can be integrated as follows:

$$\mathbf{f}^{\text{int}} = \sum_{i=1}^4 \frac{V}{4} \bar{\mathbf{B}}^T(\xi_i) \boldsymbol{\tau}(\xi_i) \quad (146)$$

where  $\xi_i$  denotes the natural coordinates of the integration point  $i$  and  $V$  is the element volume.

The element internal force vector can be rearranged in the form

$$\mathbf{f}^{\text{int}} = \mathbf{f}_4^{\text{int}} + \mathbf{f}_{\text{stab}}^{\text{int}} \quad (147)$$

where  $\mathbf{f}_4^{\text{int}}$  and  $\mathbf{f}_{\text{stab}}^{\text{int}}$  are the internal force vectors resulting from a four-point quadrature and the stabilization procedure, respectively. They are given by

$$\mathbf{f}_4^{\text{int}} = \sum_{i=1}^4 \frac{V}{4} \begin{bmatrix} \tau_{11}(\xi_i) \mathbf{b}_1 + \tau_{12}(\xi_i) \mathbf{b}_2 + \tau_{13}(\xi_i) \mathbf{b}_3 \\ \tau_{21}(\xi_i) \mathbf{b}_1 + \tau_{22}(\xi_i) \mathbf{b}_2 + \tau_{23}(\xi_i) \mathbf{b}_3 \\ \tau_{31}(\xi_i) \mathbf{b}_1 + \tau_{32}(\xi_i) \mathbf{b}_2 + \tau_{33}(\xi_i) \mathbf{b}_3 \end{bmatrix} \quad (148)$$

and

$$\mathbf{f}_{\text{stab}}^{\text{int}} = \sum_{i=1}^4 \frac{V}{32} \begin{bmatrix} \mathbf{g}_1(\xi_i) \tau_{11}^{\text{dev}}(\xi_i) + \mathbf{g}_4(\xi_i) \tau_{12}(\xi_i) + \mathbf{g}_5(\xi_i) \tau_{31}(\xi_i) \\ \mathbf{g}_2(\xi_i) \tau_{22}^{\text{dev}}(\xi_i) + \mathbf{g}_6(\xi_i) \tau_{12}(\xi_i) + \mathbf{g}_7(\xi_i) \tau_{23}(\xi_i) \\ \mathbf{g}_3(\xi_i) \tau_{33}^{\text{dev}}(\xi_i) + \mathbf{g}_8(\xi_i) \tau_{23}(\xi_i) + \mathbf{g}_9(\xi_i) \tau_{31}(\xi_i) \end{bmatrix} \quad (149)$$

where the superscript, dev, denotes the deviatoric part of the stress, and the other quantities are given by

$$\mathbf{g}_1(\boldsymbol{\xi}) = D_{11}(\eta\gamma_1 + \xi\gamma_2 + 2\eta\zeta\gamma_4) \quad (150)$$

$$\mathbf{g}_2(\boldsymbol{\xi}) = D_{22}(\xi\gamma_1 + \zeta\gamma_3 + 2\xi\zeta\gamma_4) \quad (151)$$

$$\mathbf{g}_3(\boldsymbol{\xi}) = D_{33}(\xi\gamma_2 + \eta\gamma_3 + 2\xi\eta\gamma_4) \quad (152)$$

$$\mathbf{g}_4(\boldsymbol{\xi}) = D_{22}\zeta\gamma_3 \quad (153)$$

$$\mathbf{g}_5(\boldsymbol{\xi}) = D_{33}\eta\gamma_3 \quad (154)$$

$$\mathbf{g}_6(\boldsymbol{\xi}) = D_{11} \zeta \gamma_2 \quad (155)$$

$$\mathbf{g}_7(\boldsymbol{\xi}) = D_{33} \xi \gamma_2 \quad (156)$$

$$\mathbf{g}_8(\boldsymbol{\xi}) = D_{22} \xi \gamma_1 \quad (157)$$

$$\mathbf{g}_9(\boldsymbol{\xi}) = D_{11} \eta \gamma_1 \quad (158)$$

It is noted that the element developed above cannot pass the patch test because with the one-point quadrature the element internal forces are not properly evaluated if the element is skewed. To remedy this drawback,  $\mathbf{B}_a(\mathbf{0})$  are replaced by the uniform matrices,  $\tilde{\mathbf{B}}_a$ , defined by Belytschko *et al.* [18,19].

$$\tilde{\mathbf{B}}_a = \frac{1}{V_e} \int_{\Omega^e} \mathbf{B}_a(\xi, \eta, \zeta) dV \quad (159)$$

where  $V_e$  is the element volume. Similarly, equation (85) is modified as

$$\tilde{\mathbf{B}}_a(\mathbf{0}) = \begin{bmatrix} \tilde{\mathbf{b}}_{1a} \\ \tilde{\mathbf{b}}_{2a} \\ \tilde{\mathbf{b}}_{3a} \end{bmatrix} \quad (160)$$

and the stabilization vectors are redefined as

$$\tilde{\gamma}_\alpha = \mathbf{h}_\alpha - (\mathbf{h}_\alpha^T \mathbf{x}_i) \tilde{\mathbf{b}}_i \quad (161)$$

which span the proper null-space. Since, the element internal force vector can be evaluated exactly when the element is subjected to a constant strain rate field, the use of the uniform gradient matrices  $\tilde{\mathbf{B}}_a$  leads to a new four-quadrature-point-element which passes the patch test.

## 4. NUMERICAL EXAMPLES

We now present geometrically non-linear analysis of flat and curved composite laminates and compare the results with the published data by various investigators. This task is performed to verify and validate the proposed model with the established benchmark problems. The main feature of the proposed formulation is that it can easily model the layered material with orthotropic material properties. Comparison is made with some of the celebrated shell models in the literature.

### 4.1 Geometrically nonlinear bending of a narrow cantilever plate under point load

The first simulation is that of a narrow cantilever isotropic plate subjected to a concentrated load, and comparison is done with the shell element *SHEBA* by Argyris *et al.* [26]. The concentrated load is applied in equal intervals at the middle of the right boundary (see Fig. 4). The values of Young's modulus  $E = 2.1 \times 10^{10} \text{ kg/cm}^2$  and Poisson ratio  $\nu = 0.3$  are used in this analysis. The value of applied load,  $P$  is  $4 \times 10^3 \text{ kg}$ . The applied load versus the displacement path (Fig. 5) of the load point in our simulation shows a close agreement with that given by Argyris *et al.* [26]. The superposed initial and final meshes are shown in Fig. 6 and surface stresses  $\sigma_{xx}$  are shown in Fig. 7.

## Nonlinear bending of thin cantilever isotropic plate

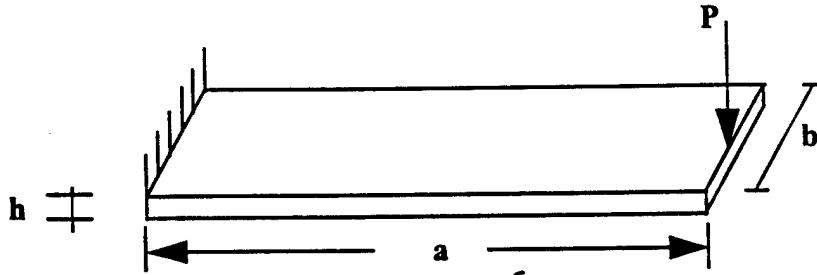


Fig. 4. Schematic diagram of the problem.

## Nonlinear bending of a thin cantilever isotropic plate

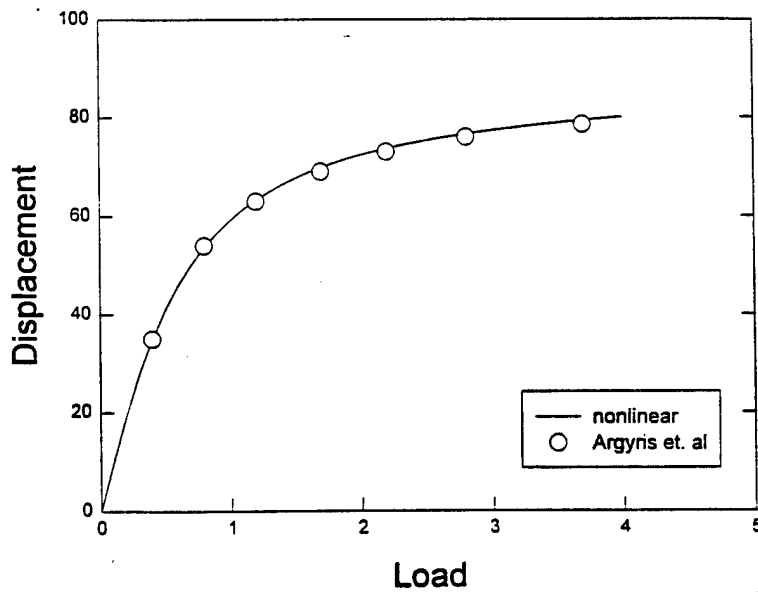


Fig. 5. Load-deflection diagram at point under the load.

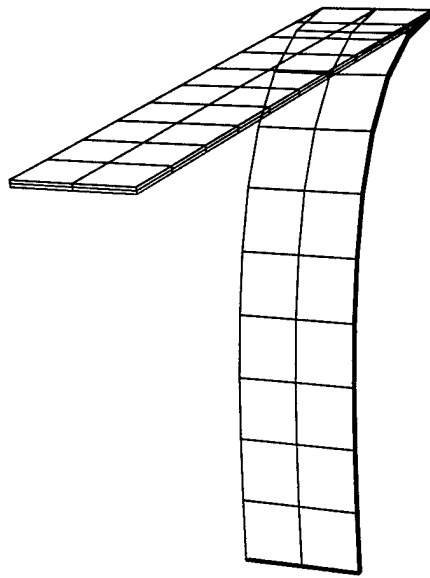


Fig. 6. Initial and final deformed geometry.

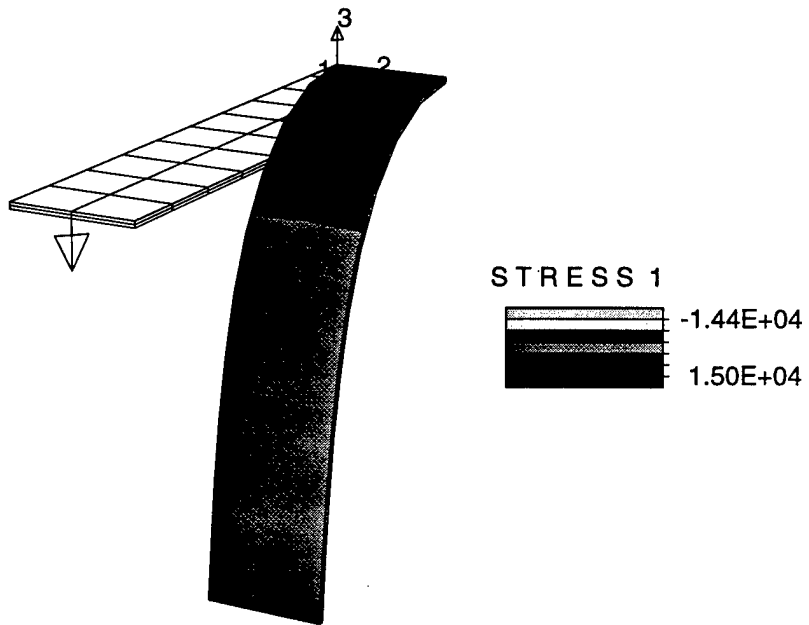
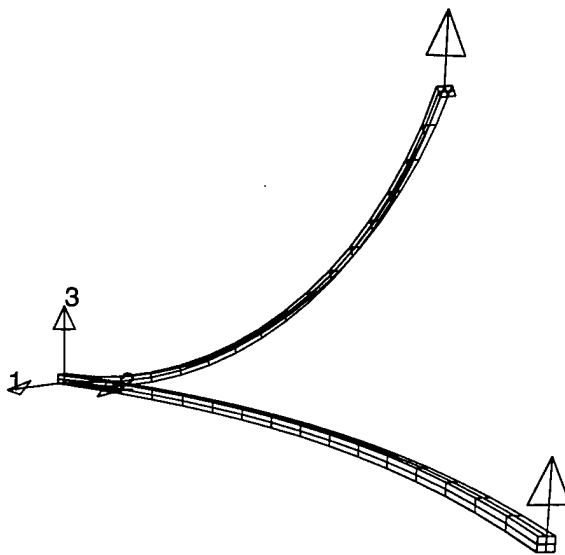


Fig. 7. Surface stress distribution for  $\sigma_{xx}$  on the final deformed geometry.

## 4.2 Large deformation analysis of three-dimensional curvilinear beam

This example presents large displacement response of a three-dimensional curvilinear cantilever beam. The beam has a cross-sectional area of  $1 \text{ in}^2$  and lies in the  $X - Y$  plane. In the undeformed configuration the cantilever bend has a radius of 100 inch and an angle of  $45^\circ$ . A concentrated load is applied at one of the ends of the beam in the  $Z$  direction while the opposite end is kept fixed. Because of its curved geometry and the eccentricity of the applied load, the beam undergoes bending as well as twisting deformations. The finite element mesh is composed of  $16 \times 2 \times 1$  elements. Material properties used are: Young's modulus  $E = 10^7 \text{ psi}$  and Poisson's ratios  $\nu = 0$ .

Figure 8 shows the initial and the final deflected shapes of the cantilever. The graph for tip deflection plotted against the load parameter can be seen in Figure 9. Results are compared with the beam element of Bathe and Bolourchi and 3D co-rotational element of Moita and Crisfield. Computed results show a very good correlation with the published results.



*Fig. 8.* Initial and final deformed geometry.  
Three Dimensional Curvilinear Beam

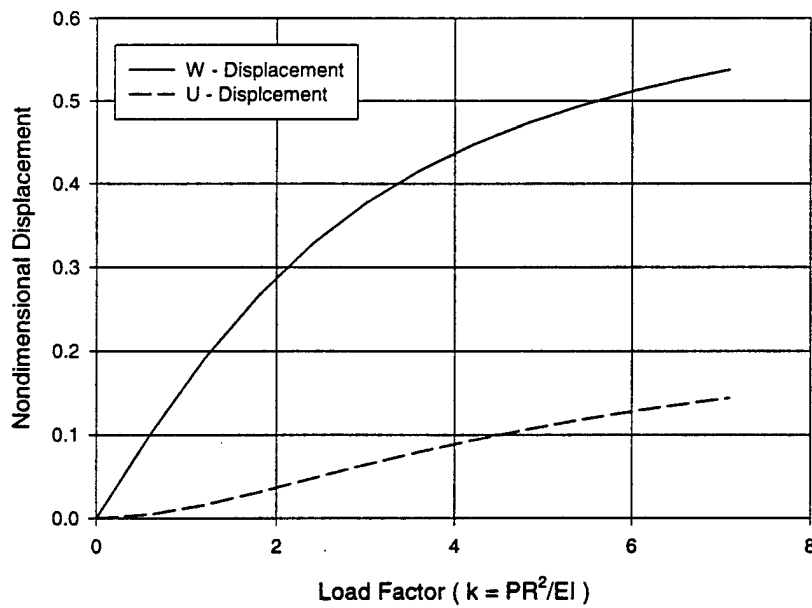


*Fig. 9.* Load-deflection diagram.

### 4.3 Geometrically nonlinear analysis of a clamped isotropic plate under uniform pressure load

The next numerical simulation is a large deformation analysis of a fully clamped isotropic plate. Again we have selected this isotropic problem to benchmark our element for geometrically nonlinear analysis. Material properties are, Youngs Modulus  $E = 2 \times 10^4 kg/mm^2$  and Poisson ratio  $\nu = 0.3$ . The plate is loaded by applying a uniform pressure of intensity  $q = 0.8 \times 10^{-4} kg/mm^2$  (see Fig. 10). To solve this problem we generated a mesh of  $8 \times 8 \times 2$  hybrid elements. The pseudo-time increment in the nonlinear solution strategy is  $\Delta t = 0.01$ . A total of 100 steps were required to apply the total load. Fig 11 presents the nonlinear load-deflection curve obtained at the point under the load which compares very well with the experiment load-deflection curve reported in Kawai *et al.* [24]. Figs. 12 and 13 present the top and bottom view of the surface stresses for the final step.

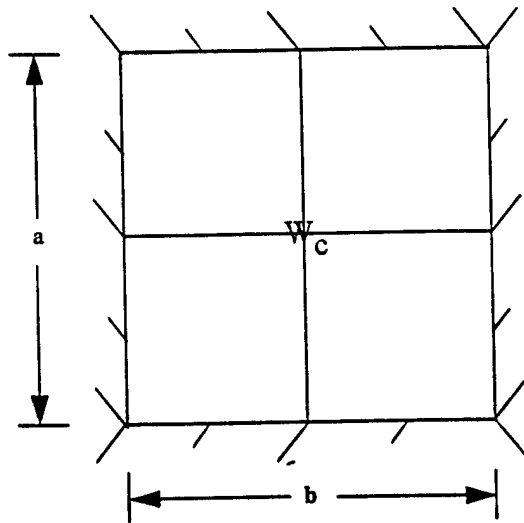


Fig. 10. Schematic diagram of the problem.

### Nonlinear bending of isotropic plate under uniform distributed load

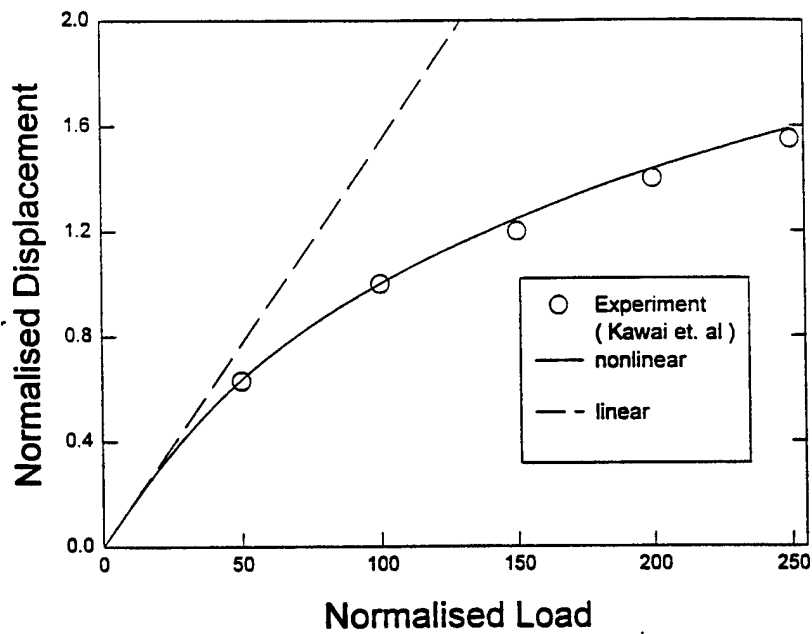


Fig. 11. Load-deflection diagram at the center of the plate.

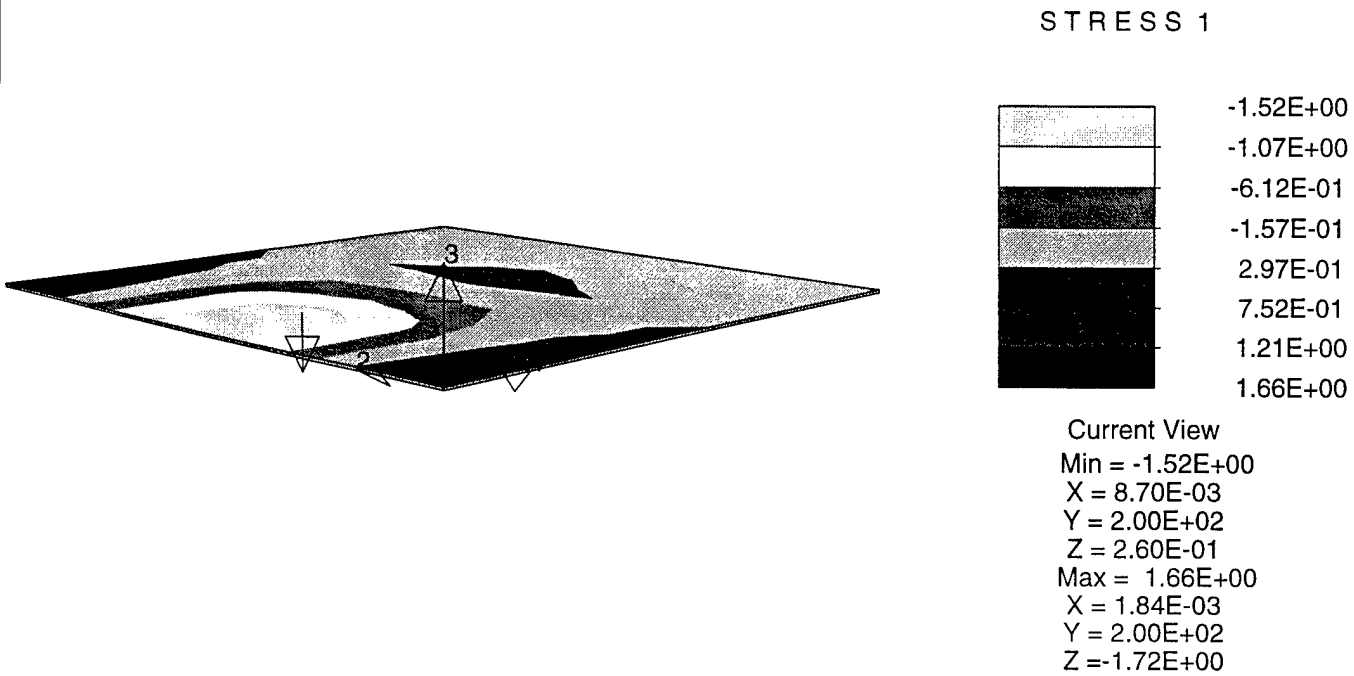


Fig. 12. Surface stress distribution for  $\sigma_{xx}$  on the top surface.

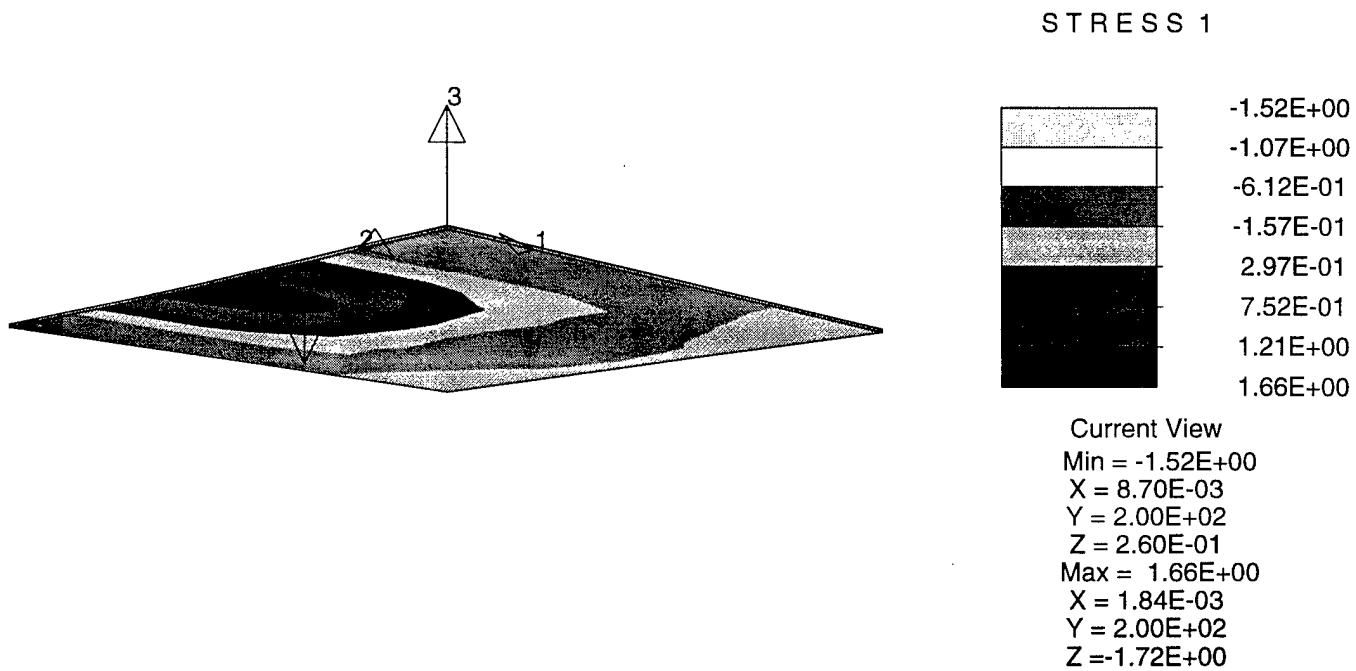


Fig. 13. Surface stress distribution for  $\sigma_{xx}$  on the bottom surface.

#### 4.4 Pinched cylindrical shell with free edges

The next simulation is that of a cylindrical shell with free edges (Fig. 14), subjected to two opposite point loads. In this test case the shell is able to undergo finite rotations and thus provides a severe test for the veracity of the underlying formulation. The overall response represents two distinct features; an initial portion that is dominated by bending and is characterized by large displacement, and a later portion that is dominated by membrane effects that are characterized by a very stiff response. Invoking the symmetry conditions, only one-eighth of the shell is modeled using  $16 \times 8 \times 2$  elements (16 along the periphery, 8 along the length and 2 through the thickness). The depicted curves show the displacement under the load, as well as the horizontal displacement at the side of the shell. The final deformed configuration of the shell is shown in Fig. 16.

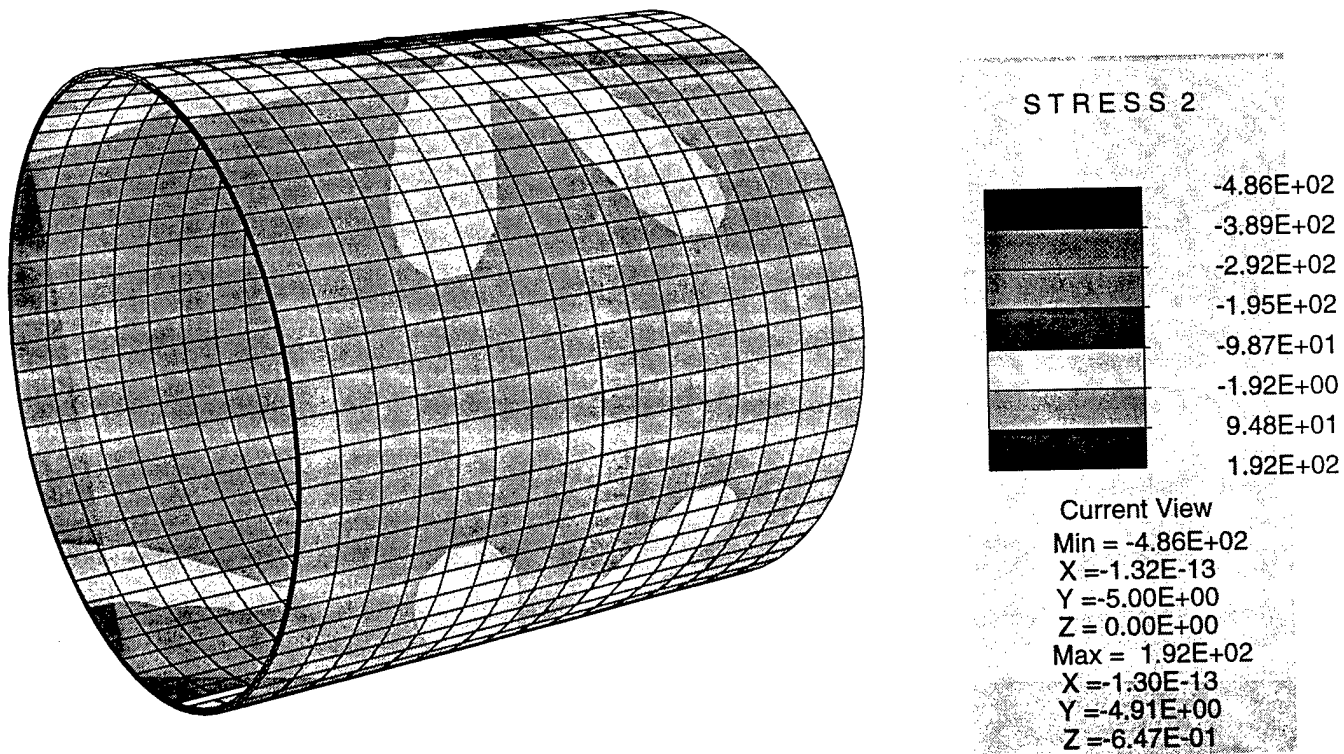


Fig. 14. Initial geometry and loads.

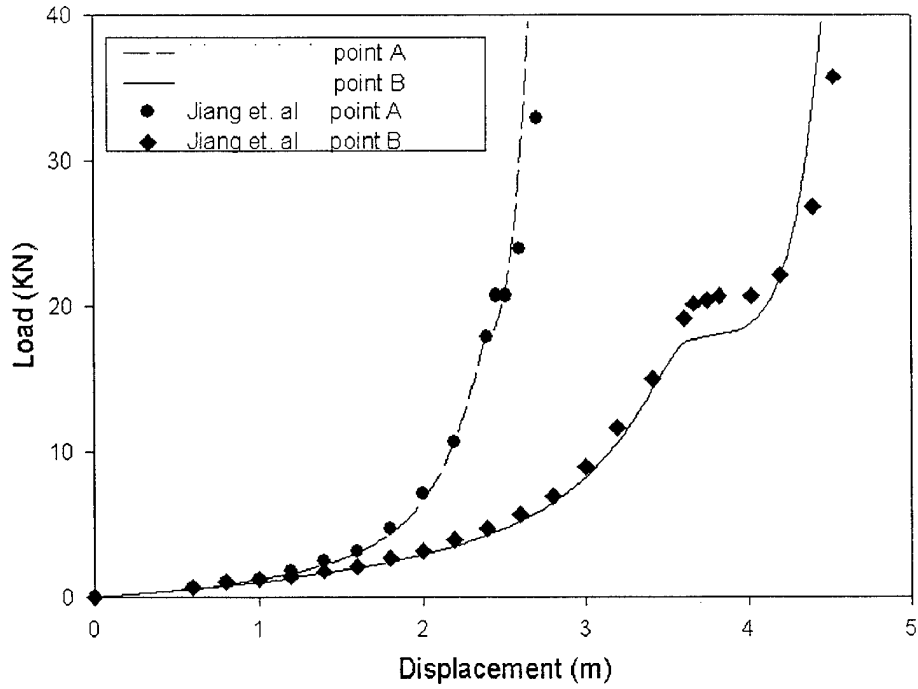


Fig. 15. Load-deflection diagram.

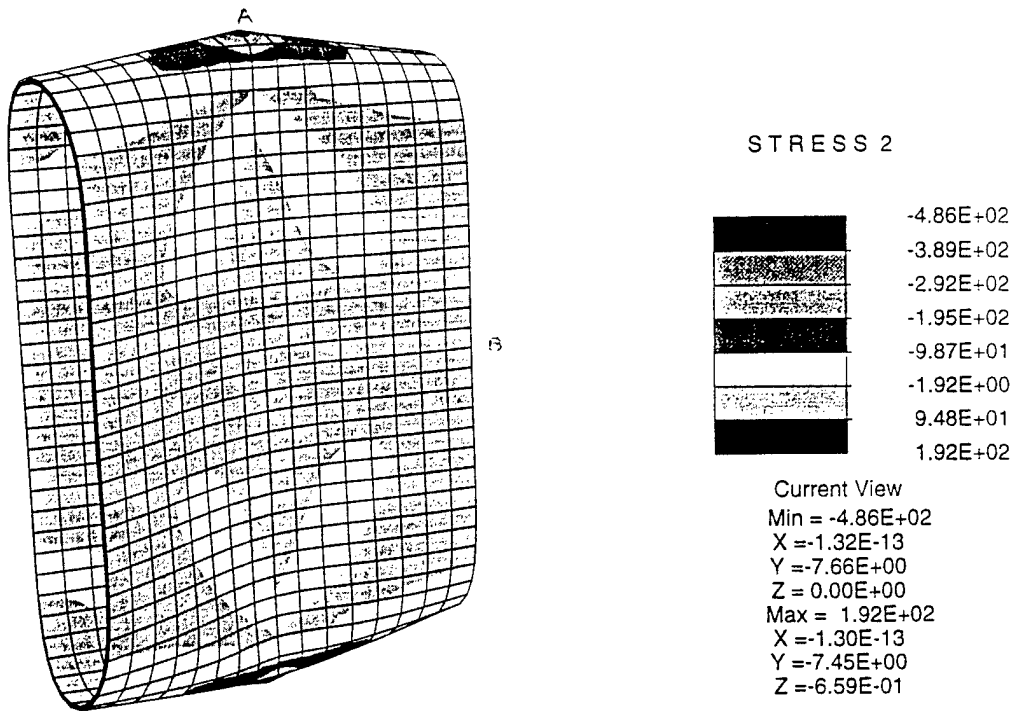


Fig. 16. Final deformed geometry.

## 4.5 Pinched hemispherical shell

The next problem is that of a pinched hemispherical shell which is a popular benchmark problem for linear as well as nonlinear shell analysis. The undeformed configuration of the shell has a  $18^\circ$  hole at the top and is subjected to two inward and two outward forces that are  $90^\circ$  apart. The material and geometric properties are:  $E = 6.825 \times 10^7$  psi,  $\nu = 0.3$ , radius  $R = 10$  inch and thickness  $t = 0.04$  inch. Because of the symmetry conditions that can be applied, only one quadrant needs to be modeled. A plot of the pinching load versus the deflection under the corresponding pinching load is shown in Fig. 18. Comparison is made with "stress resultant geometrically exact shell model of Simo *et al.* 25]. Figure 19 shows the final deformed mesh configuration without any magnification of the deformation.

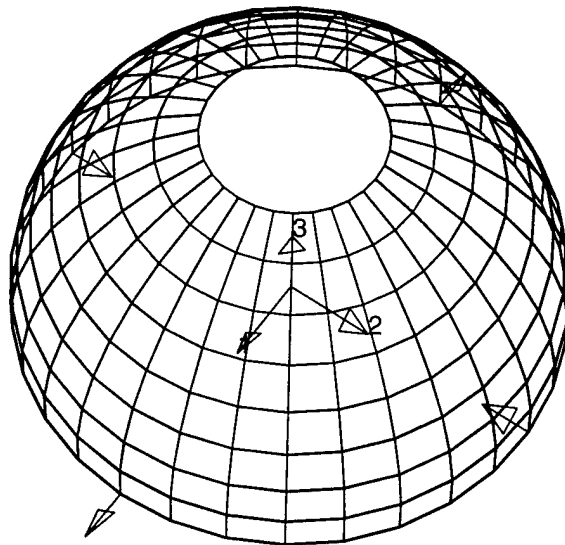


Fig. 17. Initial geometry and loads.

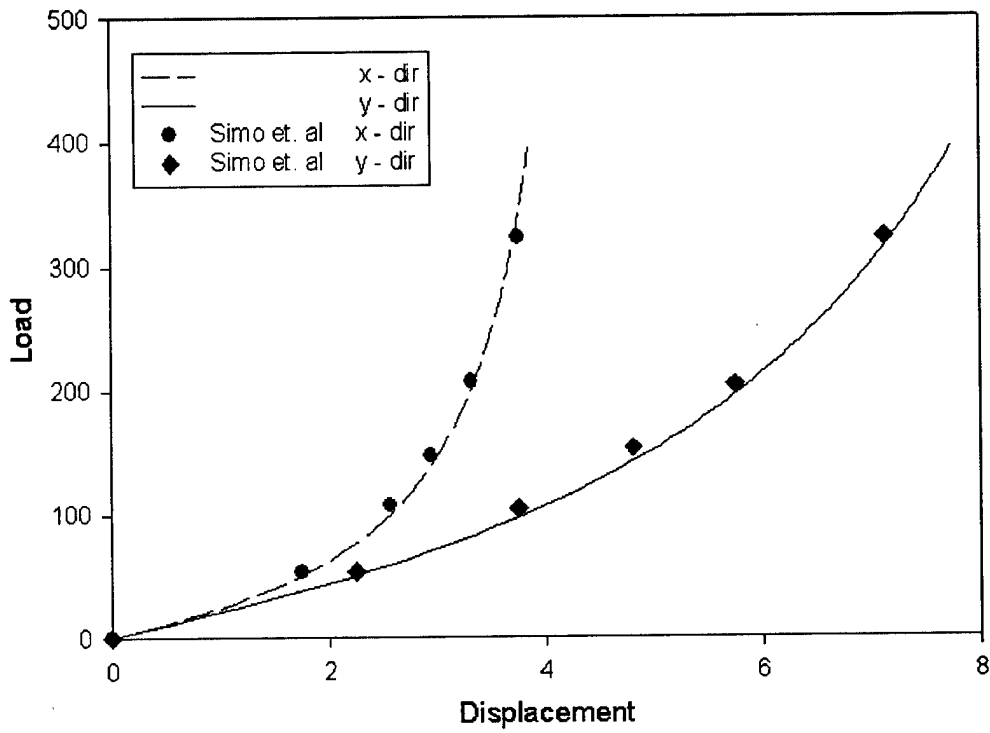
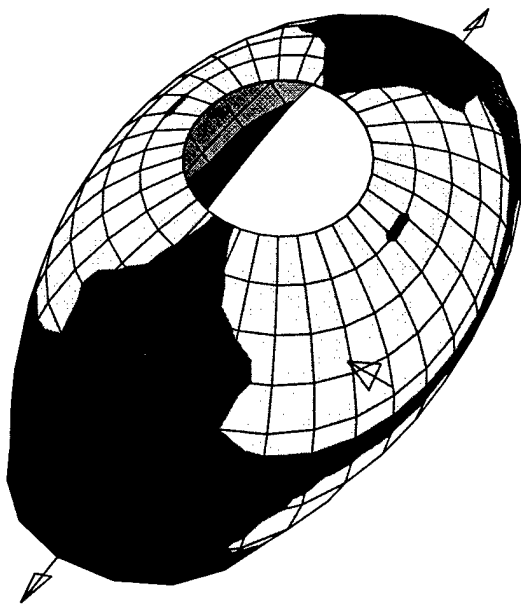
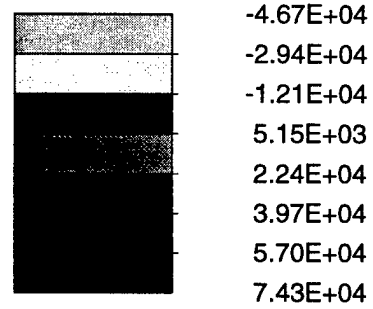


Fig. 18. Load-deflection diagram.



STRESS 1



Current View  
 Min = -3.36E+04  
 X = 2.52E-13  
 Y = 6.98E+00  
 Z = 1.50E+00  
 Max = 7.43E+04  
 X = -8.00E-13  
 Y = -4.96E+00  
 Z = -9.49E-01

Fig. 19. Final deformed geometry.

## References

- [1] Zienkiewicz, O.C., (1977), *The Finite Element Method* (3rd edition), McGraw-Hill.
- [2] Bathe, K.J., (1982), *Finite Element Procedures in Engineering Analysis*, Prentice-Hall, Inc. New Jersey.
- [3] Liao, C.L. and Reddy, J.N., (1990), "Analysis of anisotropic, stiffened composite laminates using a continuum-based shell element", *Comp. Struct.*, **34**, No. 6, 805-815.
- [4] Belytschko, T. and Hsieh, B.J., (1973), "Non-linear transient finite element analysis with convected coordinates", *Internat. J. Numer. Methods Engrg.*, **7**, 255-271.
- [5] Wempner, G., (1969), "Finite elements, finite rotations and small strains of flexible shells", *Internat. J. Solids Structures*, **5**, 117-153.
- [6] Harrigmoe, G. and Bergan, P.G., (1978), "Nonlinear analysis of free-form shells by flat finite elements", *Comput. Methods in Appl. Mech. Engrg.*, **16**, 11-35.
- [7] Clarke, M.J. and Hancock, G.J., (1990), "A study of incremental-iterative strategies for non-linear analysis", *Internat. J. Numer. Methods Engrg.*, **29**, 1365-1391.
- [8] Bergan, P.G., Harrigmoe, G., Krakeland, B. and Soreide, T.H., (1978), "Solution techniques for non-linear finite element problems", *Internat. J. Numer. Methods Engrg.*, **12**, 1677-1696.
- [9] Argyris, J., Balmer, H. and Doltsinis, I.S., (1987), "Implementation of a nonlinear capability on a linear software system", *Comput. Methods in Appl. Mech. Engrg.*, **65**, 267-291.
- [10] Riks, E., (December 1971), "The application of Newton's method to the problem of elastic stability", ASME, *J. of Appl. Mech.*, 1060-1065.

- [11] Riks, E., (1979), "An incremental approach to the solution of snapping and buckling problems", *Internat. J. Solids Structures*, **15**, 529-551.
- [12] Crisfield, M.A., (1981), "A fast incremental/iterative solution procedure that handles "snap-through"", *Comp. Struct.*, **13**, 55-62.
- [13] Bathe, K.J. and Dvorkin, E.N., (1983), "On the automatic solution of nonlinear finite element equations", *Comp. Struct.*, **17**, No. 5-6, 871-879.
- [14] Malkus, D.S. and Hughes, T.J.R., (1978), "Mixed finite element methods-reduced and selective integration techniques: a unification of concepts", *Comput. Methods in Appl. Mech. Engrg.*, **15**, 63-81.
- [15] Nagtegaal, J.C., Parks, D.M. and Rice, J.R., (1974), "On numerical accurate finite element solutions in the fully plastic range", *Comput. Methods in Appl. Mech. Engrg.*, **4**, 153-177.
- [16] Flanagan, D.P. and Belytschko, T., (1981), "A uniform strain hexahedron and quadrilateral with orthogaonal hourglass control", *Internat. J. Numer. Methods Engrg.*, **17**, 679-706.
- [17] Belytschko, T., (1983), "Correction of article by Flanagan, D.P. and Belytschko, T.", *Internat. J. Numer. Methods Engrg.*, **19**, 467-468.
- [18] Belytschko, T., Ong, J.S.-J., Liu, W.K. and Kennedy, J.M., (1984), "Hourglass control in linear and nonlinear problems", *Comput. Methods in Appl. Mech. Engrg.*, **43** , 251-276.
- [19] Liu, W.K. and Belytschko, T., (1984), "Efficient linear and nonlinear heat conduction with a quadrilateral element", *Internat. J. Numer. Methods Engrg.*, **20**, 931-948.
- [20] Belytschko, T. and Bindeman, L.P., (1991), "Assumed strain stabilization of the 4-node quadrilateral with 1-point quadrature for nonlinear problems", *Comput. Methods in Appl. Mech. Engrg.*, **88**, 311-340.

- [21] Belytshcko, T. and Bindeman, L.P., "Assumed strain stabilization of the eight node hexahedral element", to be published.
- [22] Liu, W.K., Ong, J.S.-J. and Uras, R.A., (1985), "Finite element stabilization matrixed - a unification approach", *Comput. Methods in Appl. Mech. Engrg.*, **53**, 13-46.
- [23] Liu, W.K., Chang, H., Chen, J.S. and Belytschko, T., (1988), "ALE Petrov-Galerkin finite elements for nonlinear continua", *Comput. Methods in Appl. Mech. Engrg.*, **68**, 259-310.
- [24] Kawai, T. and Yoshimura, N., (1969) "Analysis of large deflection of plates by the finite element method", *Int̄ernat. J. Numer. Methods Engrg.*, **1**, 123-133.
- [25] Simo, J.C., Fox, D.D and Rifai, M.S., (1990) "On a stress resultant geometrically exact shell model, Part III: Computational aspects of the nonlinear theory," *Comput. Methods in Appl. Mech. Engrg.*, **79**, 21-70.
- [26] Argyris, J. and Tenek, L., (1994) "An efficient and locking-free flat anisotropic plate and shell triangular element", *Comput. Methods in Appl. Mech. Engrg.*, **118**, 63-119.
- [27] Jiang, L., Chernuka, M.W., and Pegg, N.G. , (1994) " A co-rotational updated Lagrangian formulation for geometrically nonlinear finite element analysis of shell structures", *Finite Element in Analysis and design*, Vol. **18**, 129-140.

## Part IV

# Simulation of Coupled Systems

# Chapter 1

## Coupled Elastic/SMA Simulations

This section is dedicated to numerical simulations of coupled elastic-shape memory alloy composite systems. The simulations depict an initial configuration is given which is then transformed via a thermal variation to a final configuration. Several simulations are presented to shown the robustness of the shape memory alloy and its capacity to be embedded within an elastic medium to enable a global shape changes.

## 1.1 Two-Dimensional Cantilever Beam

The first simulation consists of a configuration with an initially curved two dimensional cantilever beam. The initial configuration of the beam is shown in Figure 1.1. The simulation is conducted with a total net reaction of the beam of zero and an initial thermal state of  $31\text{ }^{\circ}\text{C}$  which is then heated to  $54\text{ }^{\circ}\text{C}$ . The material under consideration is NiTi and its associated material parameters can be found in Table 1.1. The progression of the simulation is shown in Figures 1.2 and 1.3.

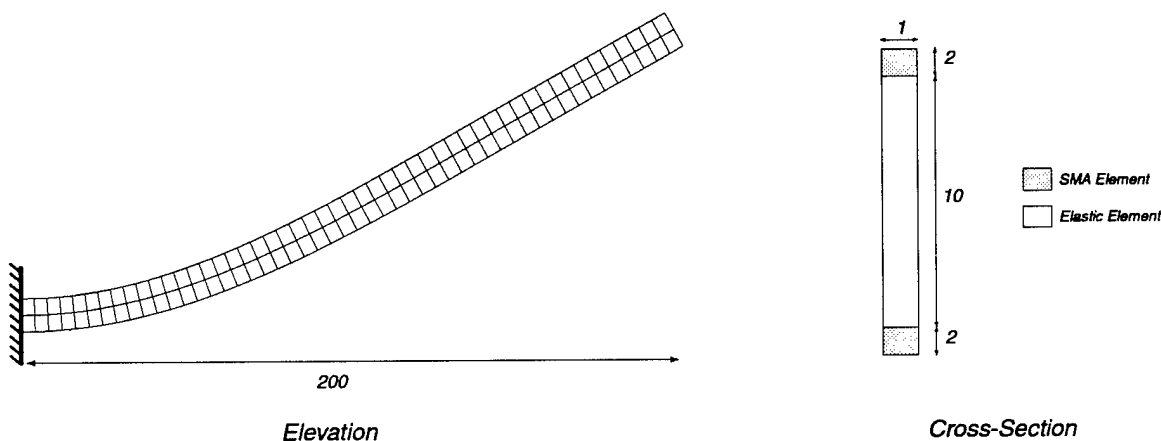


Figure 1.1: Initial Configuration of the Composite Elastic/SMA Beam.

Table 1.1: Material Properties for NiTi. (BRINSON & LAMMERING [1993])

---

Young's Moduli $E_m = E_a = 67\text{ GPa}$
Critical stresses for de-twinning $\sigma_{cr}^s = 100\text{ MPa}$ and $\sigma_{cr}^f = 170\text{ MPa}$
Martensite production temperatures $T_{ms} = 18.4\text{ C}$ and $T_{mf} = 9\text{ C}$
Austenite production temperatures $T_{as} = 34.5\text{ C}$ and $T_{af} = 49\text{ C}$
Austenite production slope $C_a = 13.8\text{ MPa/C}$
Martensite production slope $C_m = 8\text{ MPa/C}$
Maximum transformation strain $\epsilon_L = 0.067$
Thermal expansion coefficient $\alpha = 6.5\text{ }\mu\text{strain/C}$

---

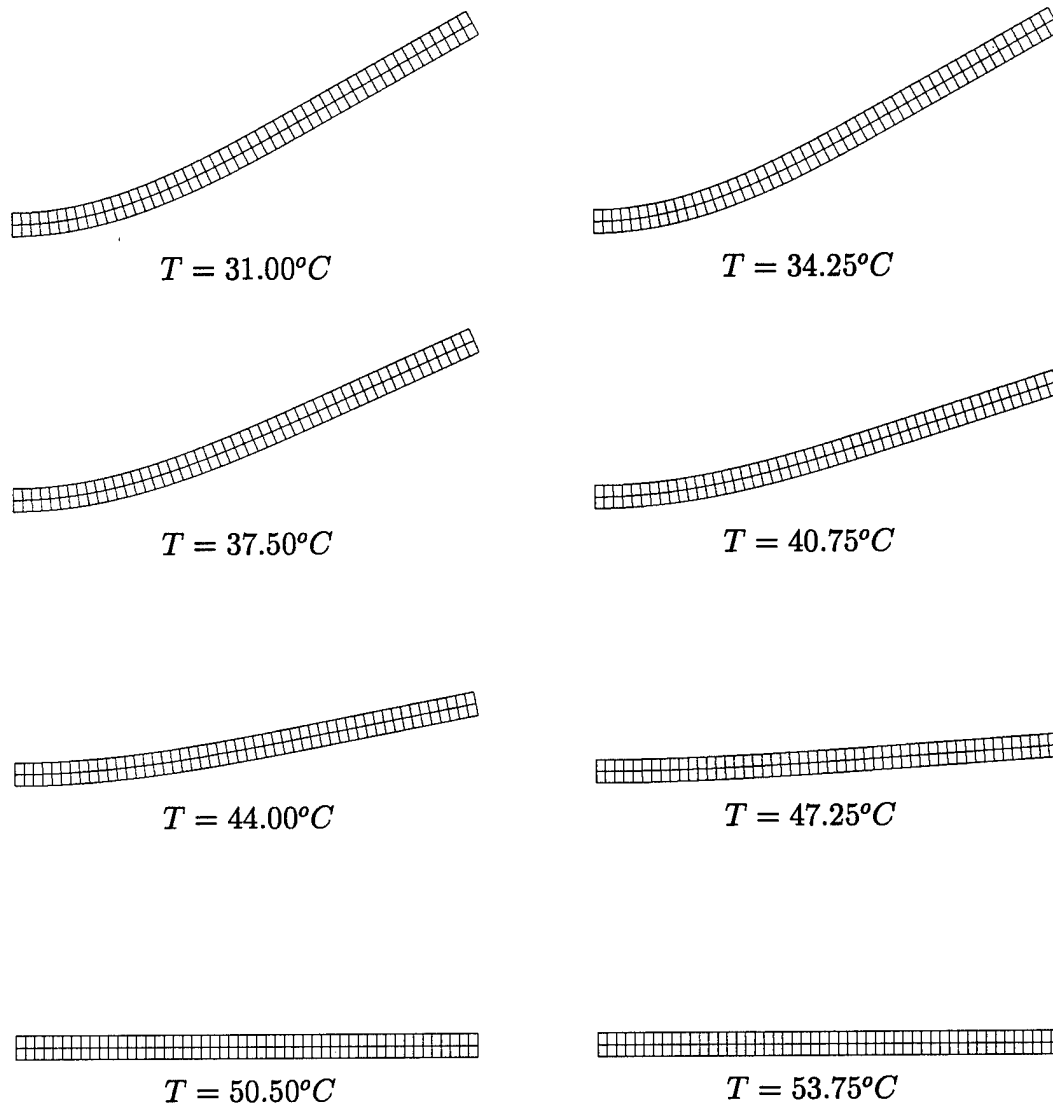


Figure 1.2: Simulation of an elastic/sma beam under a thermal cycle.

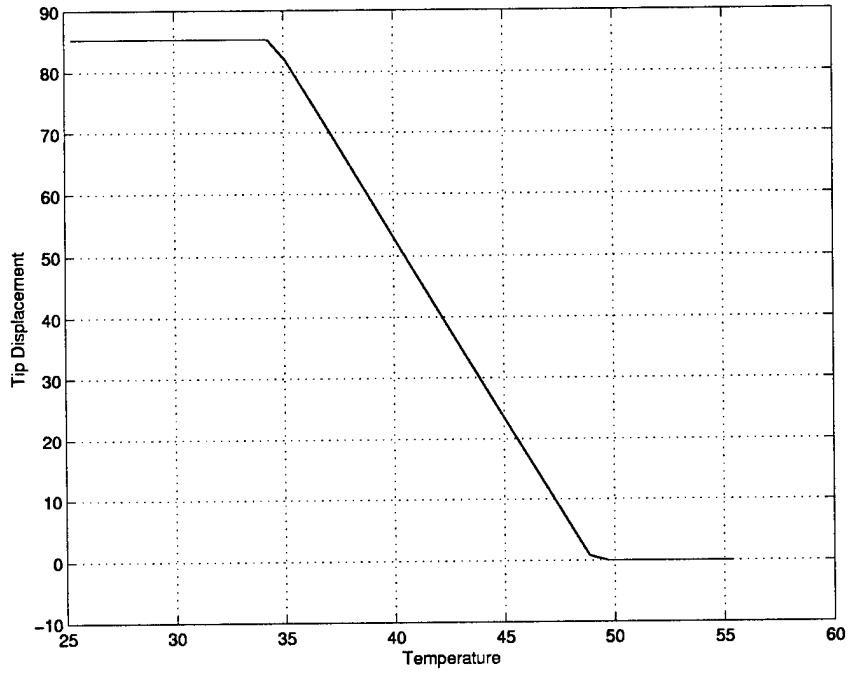


Figure 1.3: Trajectory of the displacement/temperature history.

## 1.2 Two-Dimensional Simply Supported Beam

The second simulation consists of a configuration with an initially curved two dimensional simply supported beam. The initial configuration of the beam is shown in Figure 1.4. The simulation is conducted with a total net reaction of the beam of zero and an initial thermal state of  $36.3\text{ }^{\circ}\text{C}$  which is then heated to  $50.3\text{ }^{\circ}\text{C}$ . The material under consideration is NiTi and its associated material parameters can be found in Table 1.2. The progression of the simulation is shown in Figures 1.5 and 1.6.

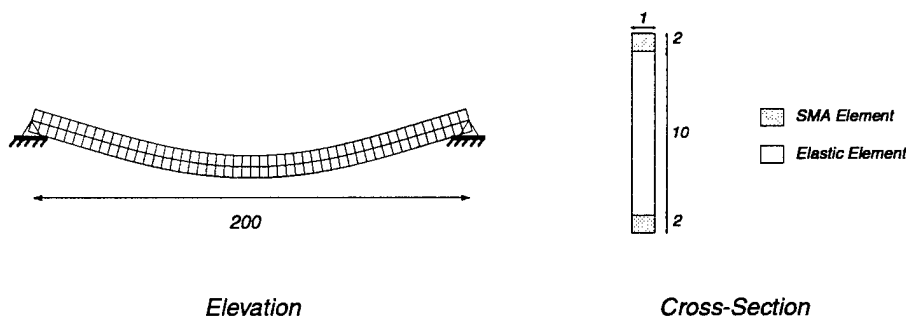


Figure 1.4: Initial Configuration of the Composite Elastic/SMA Beam.

Table 1.2: Material Properties for NiTi. (BRINSON & LAMMERING [1993])

Young's Moduli  $E_m = E_a = 67\text{ GPa}$

Critical stresses for de-twinning  $\sigma_{cr}^s = 100\text{ MPa}$  and  $\sigma_{cr}^f = 170\text{ MPa}$

Martensite production temperatures  $T_{ms} = 18.4\text{ C}$  and  $T_{mf} = 9\text{ C}$

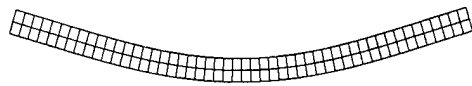
Austenite production temperatures  $T_{as} = 34.5\text{ C}$  and  $T_{af} = 49\text{ C}$

Austenite production slope  $C_a = 13.8\text{ MPa/C}$

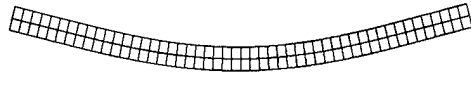
Martensite production slope  $C_m = 8\text{ MPa/C}$

Maximum transformation strain  $\varepsilon_L = 0.067$

Thermal expansion coefficient  $\alpha = 6.5\text{ }\mu\text{strain/C}$



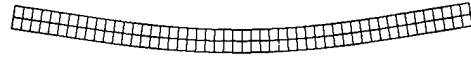
$T = 36.30^{\circ}C$



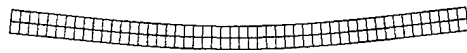
$T = 38.30^{\circ}C$



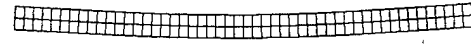
$T = 40.30^{\circ}C$



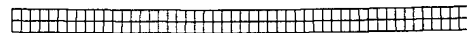
$T = 42.30^{\circ}C$



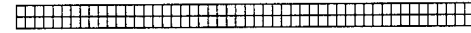
$T = 44.30^{\circ}C$



$T = 46.30^{\circ}C$



$T = 48.30^{\circ}C$



$T = 50.30^{\circ}C$

Figure 1.5: Simulation of an elastic/sma beam under a thermal cycle.

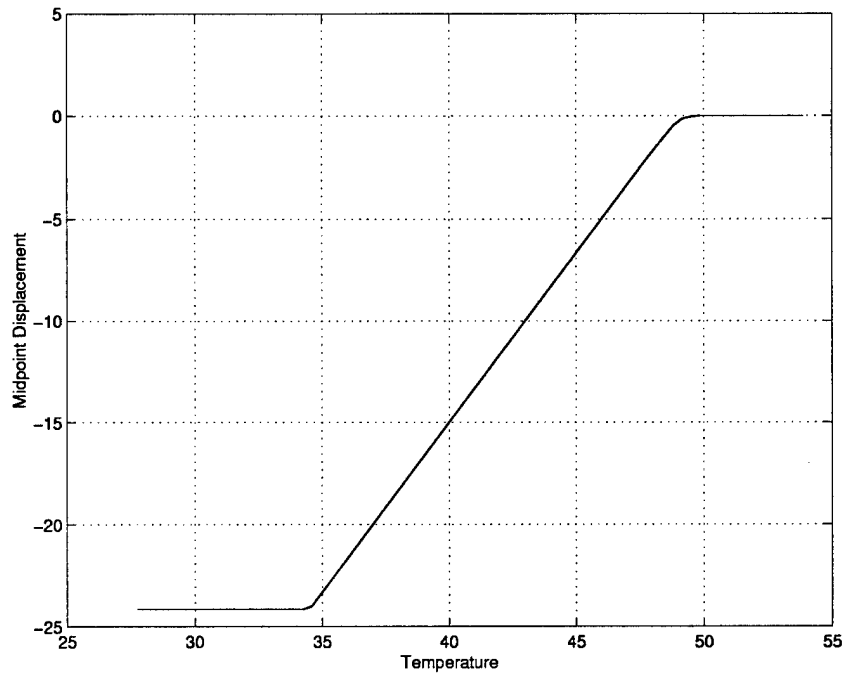


Figure 1.6: Trajectory of the displacement/temperature history.